

THE UNIVERSITY OF CHICAGO

CORRELATIONS AND SELF-ASSEMBLY IN IONIC AND NEMATIC LIQUIDS

A DISSERTATION SUBMITTED TO
THE FACULTY OF THE DIVISION OF THE PHYSICAL SCIENCES
IN CANDIDACY FOR THE DEGREE OF
DOCTOR OF PHILOSOPHY

DEPARTMENT OF CHEMISTRY

BY
NICHOLAS BENJAMIN LUDWIG

CHICAGO, ILLINOIS

DECEMBER 2019

Copyright © 2019 by Nicholas Benjamin Ludwig
All Rights Reserved

For my ancestors

“Entities should not be multiplied unnecessarily.”

– attributed to William of Ockham

TABLE OF CONTENTS

LIST OF FIGURES	viii
LIST OF TABLES	xvii
ACKNOWLEDGMENTS	xviii
ABSTRACT	xix
1 INTRODUCTION	1
2 IONIC FLUIDS: A BRIEF INTRODUCTION	5
2.1 The theory of Debye and Hückel	7
2.1.1 The Debye constant, or inverse screening length, κ_D	10
2.2 Linear response: the connection between liquid-liquid correlations and solute-liquid interactions	12
2.3 DLVO theory and Derjaguin approximation	19
2.3.1 The DLVO theory for flat plates	22
2.3.2 The Derjaguin approximation	25
2.4 Selected experiments beyond the Debye regime	27
2.4.1 Measurements of screening lengths	27
2.4.2 Unexpected stability of nanocrystals in molten salts and ionic liquids	30
2.5 Spatial correlation functions and the structure of liquids	31
2.6 Selected theory beyond Debye and Hückel	34
2.6.1 Accounting for the finite size of ions in a continuum theory for charged hard spheres	35
3 DESCRIBING SCREENING IN DENSE IONIC FLUIDS WITH A CHARGE-FRUSTRATED ISING MODEL	40
3.1 Introduction	41
3.2 Model	43
3.3 Simulation	49
3.4 Conclusions	55
3.5 Appendix: Simulation Methods	57
3.6 Appendix: Detailed Derivation of Mean Field Theory from a Lattice	58
3.6.1 Variational mean field theory for pairwise \pm spin model	59
3.6.2 Specializing to the Coulomb-frustrated Ising model	62
4 STABLE COLLOIDS IN MOLTEN INORGANIC SALTS	66
4.1 Experimental Summary	66
4.2 Summary of Simulation and Theory	67
4.3 Continuum theory for interacting surfaces in molten salts	70
4.3.1 Approximate continuum Hamiltonian for charge density ordering	72

4.3.2	Charge density order and free energy in two-surface geometry	74
4.4	Molecular dynamics (MD) simulations of NCs in molten KCl	80
4.4.1	Simulations of ion layering on a CdSe NC	80
4.4.2	Simulations of ion layering on a structureless (or chemically inert) wall	87
4.4.3	Details of molecular dynamics (MD) simulation	89
5	NANOCRYSTALS IN MOLTEN SALTS AND IONIC LIQUIDS: EXPERIMENTAL OBSERVATION OF IONIC CORRELATIONS EXTENDING BEYOND THE DEBYE LENGTH	91
5.1	Experimental Summary	93
5.1.1	Questions	96
5.2	Simulation on CdSe nanocrystal colloids in BMIM^+Cl^- solvent system	96
5.3	Conclusions	100
5.4	Methods	100
5.4.1	Molecular dynamics model	100
5.4.2	Molecular dynamics analysis	102
5.4.3	Estimating the interaction free energy between two small nanoparticles	103
6	EXTENDING THE CHARGE-FRUSTRATED ISING MODEL	104
6.1	Solutes	105
6.1.1	Charge density profiles	105
6.1.2	Potential of mean force between two solutes	108
6.2	Asymmetric Solvent and Defects	109
6.2.1	Asymmetric charge and spin	109
6.2.2	With defects	111
6.2.3	Asymmetric size	113
6.3	Future work	114
6.4	Appendix: Allowing solutes to translate and rotate	115
6.4.1	Increasing the probability of solute moves by relaxing local solvent .	115
7	SHAPE AND NUCLEATION DYNAMICS OF NEMATIC TACTOIDS IN CONTACT WITH WETTABLE COLLOIDS	120
7.1	Introduction	120
7.2	Colloid-tactoid interactions in a molecular dynamics model	122
7.2.1	Nematic tactoids associate with aster-like colloids	122
7.2.2	Strong interactions and slow dynamics can lead to transient nucleation of multiple tactoids on a single colloid	126
7.3	Tactoids and homeotropic colloids in a continuum phase field simulation . .	128
7.4	Discussion	132
7.5	Appendix	137
7.5.1	Gay-Berne parameterization and simulation protocol	137
7.5.2	Implementing a homeotropic colloid in molecular dynamics	138
7.5.3	Finding the near-optimal spacing of points on a sphere	140
7.5.4	Aspect ratio of GB tactoids	141

7.5.5	Extraction of director field	141
7.5.6	Measurement of surface tension	143
7.5.7	Large tactoids partially engulf aster-like colloids	143
7.5.8	Details of continuum simulations	146
7.5.9	Derivation of free energy of a thin splayed nematic layer on the surface of an adhesive colloid	146
8	CONCLUSIONS AND OUTLOOK	151
9	APPENDIX	155
9.1	The Euler–Lagrange equation	155
9.1.1	One-dimensional case	155
9.1.2	Three-dimensional case	156
9.2	Fourier transformation conventions	157
9.3	Inverse Fourier transformation of a k^4 order parameter correlation function .	158
9.3.1	Poles for k^4 order parameter correlation function	159
9.3.2	Computing the inverse Fourier transform contour integrals	162
	REFERENCES	165

LIST OF FIGURES

2.1	The van der Waals interaction energy of two spheres of radius R at a distance of closest approach D . The exact expression is shown in blue, while the short distance ($D \ll R$) limit is plotted in orange.	20
2.2	The van der Waals interaction energy of two spheres of radius R at a distance of closest approach D paired with a mock repulsive, exponential potential.	22
2.3	Schematic of the geometry used to derived the Derjaguin approximation. Two spheres of radius R have a distance of closest approach D , with $D \ll R$. The interaction between spheres is approximated as the integral of the interaction between plates a distance z apart over ring-like area sections of area $2\pi r dr$	26
2.4	Measurement from Lee et al. [1] surface force aparatus experiments showing the measured screening length, $\kappa_s \sigma$ as a function of the Debye constant, $\kappa_D \sigma$, both scaled by the estimated ion size σ . The measurement is for a variety of ionic fluids and shows that for small Debye constant, the Debye-Hückel theory makes accurate predictions of the screening length. However, increasing the Debye constant past the inverse ion size, $\kappa_D \sigma > 1$, leads to a break from the DH theory, and specifically, a scaling of $\kappa_s \sigma \sim (\kappa_D \sigma)^{-2}$. Data reproduced from Ref. [1] with permission.	29
2.5	Cartoons showing structuring in a simple liquid of hard spheres in two dimensions. (a) Cartoon of two-dimensional hard sphere fluid. Particles are arranged roughly in concentric shells. The concentric circles are meant as guides the eye to draw attention to the arrangement into concentric shells. (b) The radial distribution function, or RDF, $g(r)$, captures the correlations between particles at a distance r from a particle fixed at the origin. The normalization is such that a value of 1 corresponds to the ideal gas, or uncorrelated, case.	32
3.1	Mean field screening constant, $\kappa_s \sigma$, identified with the inverse decay length of charge correlations, displays non-monotonic trend as the Debye screening constant, $\kappa_D \sigma = \sqrt{4\pi\rho Q/T} \sigma$, (Eq. 3.5) is increased, plotted here for $\rho Q/J = 0.5/\sigma^2$. The solid black line shows the predicted screening constant, κ_s , in the two regimes. Note the inverse dependence of κ_s on T in the two regimes (see Eq. 3.8). Near, but slightly above the regime change, the screening constant from simulation shows an apparent scaling: $\kappa_s \sigma \sim (\kappa_D \sigma)^{-1}$. The dashed line shows the Debye constant $\kappa_D \sigma$, and the dotted line shows the temperature scaling of the inverse Ising correlation length $\sqrt{T/(\sigma^2 J)} \sim 1/l_c$. The dash-dotted line is a second inverse length scale which goes as $1/l_c$ for small $\kappa_D \sigma$; it merges with $\kappa_s \sigma$ at the regime change $\bar{\kappa}_D^* \sigma$, which also marks the peak in the screening constant, $\bar{\kappa}_s^* \sigma$. . .	47

3.2	Spatial correlations in FI model for various inverse Debye screening length, κ_D , for the parameter $\rho Q/J = 0.5/\sigma^2$. a , absolute values of charge-charge correlation functions, $r G_q(r) $, plotted on log-linear scale for various Debye constants. For $\kappa_D \ll \kappa_D^*$, the correlations decay purely exponentially as shown in the bottom two plots, while oscillations appear when $\kappa_D \gg \kappa_D^*$, see the top two plots. The solid black lines correspond to the envelope of these functions from which κ_s can be extracted. The dotted black line is the DH prediction for the decay of correlations. b , Fourier charge correlation functions scaled by temperature, $\tilde{G}_q(k)/T$, for various κ_D . j is an integer in $[0, L)$. For small k , the correlation functions scale as k^2 (solid black line). For $\kappa_D \ll \kappa_D^*$, $\tilde{G}_q(k)$ plateaus when k becomes large, but as κ_D increases, oscillations appear. The peak at $k \sim 1$ shifts towards larger k with increasing Debye constant. The largest k value peak corresponds to the lattice length σ .	48
3.3	Snapshots from simulation for different temperatures with $\rho Q/J = 0.5/\sigma^2$. Plus charges are brown, minus charges are blue. Simulations are visualized using Ovito [2]. a , T=3. b , T=5. c , T=20. d , T=100.	50
3.4	Screening constant, $\kappa_s\sigma$, for different extraction methods and oscillation frequency, all from simulation for $\rho Q/J = 0.5/\sigma^2$ and compared with theory. Solid and dashed black lines shows mean field theory prediction for screening length and oscillation frequency, respectively. Blue dots show screening constant extracted from envelope fits of charge-charge correlation functions (method shown in Fig. 3.2a). Red triangles show screening constant while green square show oscillation frequency extracted from small- k course of simulation $\tilde{G}_q(k)$ (see Simulation section). The length scales from $\tilde{G}_q(k)$ fits consistently overestimate length scale in small $\kappa_D\sigma$ regime, and underestimate it in the large $\kappa_D\sigma$ regime.	51
3.5	Screening constant, $\kappa_s\sigma$, displays non-monotonic trend as $\kappa_D\sigma$ is increased, shown here for $\rho Q/J = 1/\sigma^2$. Solid black line is continuum mean field theory prediction. Blue dots are screening constants extracted from the envelope of charge-charge correlation functions, $G_q(r)$, in simulations. The effect of the negative \bar{T}_c^{FI} is visible in the slight positive curvature of the mean field prediction when $\kappa_D\sigma > \bar{\kappa}_D^*\sigma$. Near, but slightly above the regime change, simulation $\kappa_s\sigma \sim (\kappa_D\sigma)^{-1}$.	52
3.6	The screening constant, $\kappa_s\sigma$, against $\kappa_D\sigma$ for different $\rho Q/J$ ratios. We extract $\kappa_s\sigma$ here using the small- k course of $\tilde{G}_q(k)$ discussed in the Simulation section. Increasing $\rho Q/J$ shifts $\kappa_D^*\sigma$ to the right, also increasing the maximum screening constant, $\kappa_s^*\sigma$. Near but slightly above the regime change, simulation $\kappa_s\sigma \sim (\kappa_D\sigma)^{-1}$ for each $\rho Q/J$ (the dotted lines show the scaling $\sqrt{T/J} \sim (\kappa_D\sigma)^{-1}$ for each parameter set).	54

4.4	An example of parallel CdSe nanocubes in molten KCl and the corresponding charge density profile. (Left) A snapshot of layering of ions between two [001] surfaces of CdSe nanocubes ($2.45 \times 1.85 \times 1.85 \text{ nm}^3$). (Right) Simulated charge density as a function of the distance between two surfaces; note the Cd-bound Cl^- peaks have been omitted from the charge density profile. Color code in the snapshot: Orange: Cd, yellow: Se, green: K^+ , and blue: Cl^- . Here, the density profiles templated by the nanocubes constructively interfere, and so this configuration is at a free energy trough. Note that the bound layer of Cl^- ions are not shown in the charge density profile.	83
4.5	Simulated free energies of layering (blue dots with error range) for two parallel (A) and tilted (B) nanocubes ($2.45 \times 1.85 \times 1.85 \text{ nm}^3$), and fit (solid lines) by the Landau-Ginzburg theory with Coulomb interactions (Eq. 4.18). (CF) Simulated charge densities between two parallel nanocubes located at troughs (C,D) and peaks (E,F) as marked in (A); the Cd-bound Cl^- peaks have been omitted from the charge density profiles. Note that constructively interfering charge density profiles are low energy configurations and destructively interfering ones are high energy configurations.	84
4.6	Simulated free energy of layering between two quasi-spherical CdSe NCs (10 nm in diameter) in molten KCl. The quasi-spheres are formed by one parallel facet and 4, 6, or 8 tilted facets. Inset shows an example of quasi-spherical particle. The highlighted facets have four and six adjacent tilted facets contributing to the repulsive force between NCs.	86
4.7	Temperature dependence of charge ordering induced by CdSe nanocubes ($2.45 \times 1.85 \times 1.85 \text{ nm}^3$) in molten KCl. Note the first Cd-bound Cl^- peak has been omitted from each charge density profile.	87
4.8	Structureless walls are purely attractive. (Left) Density profiles of K^+ (green) and Cl^- (blue) around a hard wall. (Right) Simulated free energy between two structureless walls in molten KCl and the fit by Landau-Ginzburg theory. Structureless walls do not induce charge oscillations. As a result, the free energy is as predicted by the Landau-Ginzburg theory for solutes which perturb a field in a symmetric manner.	89
5.1	(a) Experimental PDF of Pt NCs in the dry powder, d-PDF of Pt NCs capped with S^{2-} ligands in NaSCN/KSCN after the bulk liquid PDF subtraction, and dd-PDF after additional subtraction of the NC contribution. (b) dd-PDF of Pt NCs and NaSCN/KSCN melt curves fitted using exponentially damped sinusoidal functions (black curves). (c) Log plot of the curves from (b) showing the difference in the decay lengths between the restructured and bulk melts. (d) Comparison of the dd-PDFs corresponding to the restructured NaSCN/KSCN melt around ZrO_2 and InP NCs (black curves represent fits).	94

5.2	(a,b) Comparison of the dd-PDFs corresponding to the restructured BMIM^+Cl^- melt around Pt, CdSe, and InP NCs with PDF of bulk BMIM^+Cl^- (black curves represent the fits). (c) Comparison of the experimental PDFs with the simulated radial PDF of the bulk BMIM^+Cl^- IL, and contributions from the inter-ion structures of $\text{BMIM}^+\text{-}\text{Cl}^-$, $\text{BMIM}^+\text{-}\text{BMIM}^+$, and $\text{Cl}^-\text{-}\text{Cl}^-$. (d) MD snapshot (zoomed in view) of BMIM^+Cl^- in the vicinity of the cubic zinc blende InP NC (In atoms are blue circles; P atoms are red circles). (e) Comparison of the experimental PDFs with the simulated linear PDFs in the direction of the In-rich NC surface normal, and contributions from surface-ion correlations of In-BMIM^+ , In-Cl^-	97
5.3	Log plot comparing the decay of correlations in BMIM^+Cl^- bulk solvent and BMIM^+Cl^- with Pt NCs. As in the SCN^- salt system, the restructured decay length is larger than bulk, but the increase is smaller here, compare with Fig. 5.1c.	99
6.1	Snapshots from simulation for different temperatures with $\rho Q/J = 0.5/\sigma^2$. Plus charges are brown, minus charges are blue. Simulations are visualized using Ovito [2]. a , $T=3$. b , $T=5$. c , $T=20$. d , $T=100$	106
6.2	Charge density profiles for plate of size $20\sigma \times 20\sigma \times 4\sigma$ in simulation box of size $50\sigma \times 50\sigma \times 54\sigma$, linear scale. The value of $G_q(z)$ at 0 is the positive surface charge of the plate. The regime change can be seen qualitatively as the oscillations in $T = 3$ become less pronounced in $T = 5$ before disappearing entirely by $T = 20$, which exhibits pure exponential decay.	107
6.3	Charge density profiles for plate of size $20\sigma \times 20\sigma \times 4\sigma$ in simulation box of size $50\sigma \times 50\sigma \times 54\sigma$, log scale. The value of $G_q(z)$ at 0 is the positive surface charge of the plate. Here, the qualitative change in the behavior of the correlation length	107
6.4	Screening constant measured from the single-plate charge density profiles as a function of the Debye screening length.	108
6.5	Scaling of inverse screening length for different asymmetric charge systems. Each system has $\rho Q/J = 0.5/\sigma^2$. (a),(b) $\rho_0 = 1$, and the asymmetric plus charge has valence $q_+ = 2.2$ and $q_+ = 3$, respectively. (c),(d) $\rho_0 = 0.75$, and the asymmetric plus charge has valence $q_+ = 2.2$ and $q_+ = 3$, respectively. In all four cases, the simple modification to the mean field theory does a good job capturing the DH regime and gives a reasonable prediction of the regime change point, κ_D^* . For large $\kappa_D\sigma$, the scaling $\kappa_s \sim 1/l_c$ shown as the dotted line captures the scaling close to the regime change, but does poorly as κ_D continues to be increased. As discussed in Chapter 3, the critical temperature becomes unphysically negative when $\rho Q/J$ becomes too large, and that may explain the divergence between the theory predictions and simulation results in the large $\kappa_D\sigma$ regime.	110
6.6	Scaling of inverse screening length for $\rho Q/J = 0.5/\sigma^2$ and $\rho_0 = 0.75$. The simple modification to the mean field theory captures the DH regime and does a reasonable job predicting the regime change point, κ_D^* , but predicts larger length scale decay than observed in theory in the large $\kappa_D\sigma$ regime.	112

7.1 Tactoids form from GB rods in molecular dynamics simulations with $T = 0.55$, $N = 2000$, $L = 75\sigma_0$, and can interact favorably with colloids. **(a)** Schematic for the Gay-Berne model potential for our choices of parameters when rods are parallel. Rods interact based on their distance and orientation, and depend on two aspherical parameters: κ , the aspect ratio, here set to $\kappa = 3$, and κ' , the ratio of aspherical well depths (see Appendix 7.5.1 for more details). The attractive part of the potentials for two rods with the same orientation and $\kappa' = 1$ and $\kappa' = 0.5$ are plotted in the second and third portion of this subfigure. The end-end well depth is deeper by a factor of two for $\kappa' = 0.5$. Tactoids formed from rods with $\kappa' = 1$ are the subject of Section 7.2.1, while Section 7.2.2 studies $\kappa' = 0.5$. **(b)** A snapshot from a molecular dynamics trajectory of a tactoid with $\kappa' = 1$ from a simulation without a colloid. **(c)** The director field of the cross-section at the midplane of a tactoid extracted from a molecular dynamics trajectory of a tactoid with $\kappa' = 1$ from a simulation without a colloid. **(d)** A snapshot of the homeotropic colloid used in molecular dynamics simulation. This colloid is composed of 421 fixed rods with their centers placed on the surface of a sphere with radius $3.5\sigma_0$ and is the colloid we will use in the MD portion of this work. **(e)** A snapshot from molecular dynamics simulation of a Gay-Berne tactoid with $\kappa' = 1$ associated with a homeotropic colloid. In this snapshot, the immobilized colloid is colored yellow, the molecularly-thin splayed nematic layer adsorbed to the colloid is colored blue, and all other rods are colored red. **(f)** The director field extracted from a molecular dynamics trajectory of a tactoid with $\kappa' = 1$ associated with a homeotropic colloid. Same color scheme as (e). All MD snapshots are visualized using Ovito [2].

123

7.2 In MD, two tactoids may nucleate on the surface of a homeotropic colloid with appropriate choice of parameters, but they are an unstable configuration that gradually evolves into a more stable one.. Here, $N = 2000$, $L = 96\sigma_0$. **(a)** A snapshot from a molecular dynamics trajectory of two roughly equal-sized tactoids with $\kappa' = 0.5$ associated with a homeotropic colloid. In this snapshot, the immobilized colloid is colored yellow, the thin, splayed nematic monolayer adsorbed to the colloid is colored blue, and all other rods are colored red. **(b)** The director field of the cross-section at the midplane of two tactoids extracted from a molecular dynamics trajectory of two roughly equal-sized tactoids with $\kappa' = 0.5$ associated with a homeotropic colloid. Same color scheme as (a). **(c)** Time series data showing the difference in particle number between two tactoids for $\kappa' = 0.5$. This particular nucleation event resulted in two unequally-sized tactoids at around $t \sim 1000t_0$. The smaller tactoid slowly loses particles, which are incorporated into the larger tactoid, until it disappears, leaving only the larger tactoid. Snapshots are representative of the decay of smaller tactoid. Same color scheme as (a). **(d)** Time series data showing the difference in particle number between two tactoids, demonstrating the instability of two tactoids for $\kappa' = 1$. The configuration shown in (a) was used as the initial condition, and κ' was changed to 1 at $t = 0$. The tactoids equilibrate to their new interaction potential, and then begin to translate on the colloid surface, before combining after around $300t_0$. Snapshots show a selection of the configurations as the two tactoids combine. Note the rapid timescale relative to (c). Same color scheme as (a). All MD snapshots are visualized using Ovito [2].

125

7.3 Each image shows the nematic density field, \mathbf{Q} from continuum simulation for the same tactoid droplet, in contact with a colloid that imposes homeotropic (radial) anchoring, at different times during the relaxation of the droplet shape. The tactoid is initialized with the colloid at its center. Colors show the magnitude, S , and lines show the director, \mathbf{n} , of the nematic field. The scale bars in each case correspond to 10 grid points. The simulation box is 120×120 , only part of which is shown here. The top panel shows the situation for a smaller colloid (radius, $r_0 = 4$) which has weaker interactions with the nematic. Here, topological defects, seen as regions of depleted nematic order on either side of the colloid, are induced but the overall tactoid shape is undeformed. This resembles the well-known situation for colloids in bulk nematic. The bottom panel shows the situation for the larger colloid size (radius, $r_0 = 8$) with stronger interactions with the nematic. Here, the tactoid shape can be significantly deformed, resulting in an intermediate divided state. The two divided droplets ultimately coalesce forming a single tactoid with the colloid at its pole. The colloid is not shown directly but corresponds to the region of depleted nematic density at the center of the tactoid where the colloid displaces the fluid.

129

7.4	A schematic of a tactoid with size and shape parameters: the radius, R , and the tip angle α , as defined in Ref. [3]. This tactoid is associated at its pole with a colloid of radius a that imposes homeotropic (radial) alignment on the fluid it is in contact with. The colloid surface may be covered by a thin splayed nematic layer of thickness λ of the order of the rod length.	133
7.5	Set of phase diagrams for fixed $\lambda = 0.5a$ and total tactoid volume $V_t = 2 \times 4\pi a^3/3$ with increasing $A_v = 1.0, 1.3, 1.6$. The blue line in each plot divides the region where a molecularly-thin layer forms (above the blue line, where $F_l < 0$ or $w > \epsilon$) from the region where no molecularly-thin layer forms (below, where $F_l > 0$ or $w < \epsilon$). Above the blue line, the formation of the molecularly-thin layer replaces the wetting parameter, w , with a weaker “effective wetting” of ϵ , since, upon tactoid association, the area fraction covered by the tactoid, f_t is subtracted from the total area fraction, f_l of the molecularly-thin layer in the energy penalty term, ie. $f_l \rightarrow f_l - f_t$, see discussion in main text or Appendix Section 7.5.9. Thus, the possible existence of the thin nematic layer provides an upper bound on w . For a colloid to support (meta)stable divided tactoids, the nematic-vapor interfacial anchoring energy parameter, A_v , must be above a certain value. Here, multiple tactoids are a local free energy minimum between the orange and blue lines, for which there is no wetting layer, or above the blue line and to the left of the black line, for which multiple tactoids associate with the wetting layer. However, when A_v is small enough, there is no “divided” region, as seen in the phase diagram for $A_v = 1.0$	134
7.6	Energy time series for $\kappa' = 1$, $N = 2000$, $L = 75\sigma_0$ trajectories without (blue) and with (orange) a colloid demonstrate that equilibrium is reached within a reasonable simulation time. Initial condition is a simple cubic lattice of rods that is vaporized to a gas at $T = 2.55$. The temperature is then slowly quenched over time (over the first $1000t_0$) until reaching its final value of $T = 0.55$	139
7.7	Measured aspect ratio for tactoids formed from rods with $\kappa' = 1$ as a function of particle number. This trend of tactoids formed in the GB model, first reported by [4], is opposite of that predicted by theory and observed in experiment.	142
7.8	Surface tension measurement of $\kappa' = 1$ nematic-vapor slab at $T = 0.55$ via the pressure tensor. The surface tension is one half the value of the integral at the largest value of z , ie. $\gamma \sim 0.4\epsilon_0/\sigma_0^2$ (since there are two interfaces).	144

- 7.9 Large tactoids partially engulf small colloids because perturbations to the director field are costly and are minimized by expelling the colloid to the tactoid surface. Here, $T = 0.55$, $\kappa' = 0.5$, $N = 20200$, and $L = 200\sigma_0$. **(a)** A snapshot from simulation showing a large “tactoid” partially engulfing a homeotropic colloid. Partial wetting and dissociation of the tactoid end from the colloid is only observed when the resultant tactoid is much larger than the colloid. The “tactoid” has a distinct crescent shape. In this snapshot, the immobilized colloid is colored yellow, the thin, splayed nematic layer adsorbed to the colloid is colored blue, and all other rods are colored red. **(b)** The director field extracted from simulation showing partial colloid wetting. The director field is not apparently deflected beyond the wetting layer of the colloid. Same color scheme as (a). **(c)** Zoom-in near the colloid, showing the director field beyond the splayed nematic layer is only slightly perturbed. Same color scheme as (a). All MD snapshots are visualized using Ovito [2]. 145
- 7.10 When the thickness of the thin splayed nematic layer, λ is small relative to the radius of curvature of the associated tactoid, R , the curvature can be neglected and the intersection between the tactoid and the nematic layer can be treated as a portion of a cone. The requirement that the tactoid director lines be radial at the colloid surface, discussed in Ref. [5], then sets the “cone tactoid” radial at both colloid and splayed nematic layer surfaces and means that the tactoid covers an equal area fraction of both surfaces. 150

LIST OF TABLES

- 7.1 Parameters used in the continuum simulations. The first set of parameters are for generating tactoids. The second set of parameters represent the size of the colloid and the strength of the tactoid-colloid interactions for the two cases shown in Fig. 7.3. There, we show the evolution of tactoid nematic field for two different colloids: a small colloid with weak surface interaction (upper panel) to contrast with a large colloid with strong surface interaction (lower panel). All lengths are in units of grid size, whereas energy and timescales are in arbitrary units. . . . 147

ACKNOWLEDGMENTS

There are two reasons why I'm going to keep my acknowledgments to an absolute minimum. The philosophical reason is that there is no way I could possibly thank all the people I would need to in order to be remotely fair or just. The personal reason is that, in times long past, I gave a speech in which I thanked a number of friends and family by name but forgot one friend among many, and I do not want to repeat the same mistake. So for all those to whom I owe such a great debt for your help, love, and support through the work of the past half decade, thank you, and I hope you are not offended by my less-than-explicit acknowledgement.

Explicitly, I must thank my advisor, Suriyanarayanan Vaikuntanathan, for his patience, guidance, and wisdom, and the members of my thesis committee, Aaron Dinner and Dmitri Talapin, for their advice and valuable time. I also must thank the members of the Vaikuntanathan group for the solidarity and assistance that they provided over recent years, including, but certainly not limited to, editing the document which you now read.

ABSTRACT

One characterization of human scientific and industrial development is in terms of the increasing ability to control the physical world at smaller and smaller length scales. As control has increased, we have advanced from chemistry, to nuclear physics, to particle accelerators. But control over individual particles is different from control over many [6]. In this work, we study how particles of size between nanometers and micrometers, called colloids or solutes, interact within complicated solvent systems (or “soft matter” fluids). Our goal is to learn how to design colloids and fluids such that we can control their properties, such as the solubility of colloids within the fluid, or the shapes of fluid droplets that associate with the colloid. In particular, for a large part of this work, we are motivated by recent studies of colloids and surfaces within molten salts and ionic liquids that defy theoretical explanation to this day. To work towards an explanation, we search for the key elements that are required to reproduce the observed phenomena: the minimal model to describe experiment. In addition to simple theoretical models, we extend the applicability of our work through molecular and coarse-grained computer simulation.

In this work, we first introduce some foundational theories of fluids and ionic solutions that we will return to throughout this work. Motivated by recent unexplained experimental results on high ionic strength solutions, we apply some of these theoretical tools to a lattice model, the charge-frustrated Ising model, which we use to generalize past models of dilute ionic solutions to solvents with high ionic strength. This model helps us to frame the next two studies that we detail, which examine the unexpected experimental observation that nanocrystal colloids do not precipitate out of solution in molten salts and ionic liquids, ie. are “colloidally stable”. Though our mean field model and molecular dynamics simulations, are able to explain the majority of the experimental observations in these works, some questions still remain. Next, changing focus, we examine another colloid-soft matter system, in which a colloid is able to affect shape changes upon nematic liquid crystal droplets. We provide a

set of predictions about the requirements for a colloid and fluid to have such dramatic shape changes as the stable division of fluid droplets. The connecting thread between these works is our attention to the minimal features necessary to describe these complex fluids with long-range interactions. We are continually surprised at the effectiveness of these simple models at capturing complex physical phenomenology.

CHAPTER 1

INTRODUCTION

The work in this document is addressed to the question: how can we gain control over the physical world on nano- to micro-scopic length scales? Precise control and fundamental understanding allow for rational design, and design allows for the development of industries and the engineering of the fantastic devices we take for granted every day. Even before the methods of science, control on microscopic scales existed, having been discovered through trial and error. As one example, in metal smithing, the defects within the metal fundamentally determine the physical properties of that metal [7]. Much of a smith's job was to use macroscopic procedures (such as hitting a piece of hot steel repeatedly with a hammer) in order to affect microscopic changes (properly arranging the defects within the steel). This microscopic control over defects was incidental and “evolved” rather than “understood”, the result of specific formulas and rituals that were discovered through tinkering and passed down from master to apprentice. In contrast, the coupling of a microscopic theory with rational design allows for access to possibilities far beyond those discovered purely through serendipity, for example, the transistor or superconductors. The power of rational design can be seen in the development of nanoscience, which has its origin centuries ago when metal nanocrystals were used to color stained glass windows. It was not until the development of quantum mechanics that science could explain that the bright and durable colors in these materials were due to the nanoscale sizes of the metal nanoparticles, which affected how the particles interacted with light, here through “plasmon resonance” [8]. And even then, it took another few decades before the promise of further exploring such small length scales would be fully articulated [9]. More recently, nanoscience has truly begun to flourish, but none of this was possible until understanding of physical and chemical phenomenon was unlocked.

Here, we focus on the “mesoscopic” world – between molecular length scales and a few orders of magnitude larger – because these are the length scales over which nanocrystals

and slightly larger objects interact with each other. The systems under study are frequently categorized as “soft condensed matter”, or “soft matter” [10], and consist of many particles that interact strongly, yet in which thermal energy plays a large role, relegating quantum mechanics to the background. At these length scales, the number of component pieces to build any reasonably-sized structure is too large to control piece-by-piece. Rather than try to manually place each building block ourselves, we look for a way to engineer the building blocks so that they arrange themselves into the order we desire. We call this “self-assembly” [11]. An overarching goal in the field of self-assembly at mesoscopic length scales is to acquire such a detailed ability to control matter that we can engineer structures with a similar size and fidelity as cells do in nature.

Broadly, there are two main approaches to accomplish self-assembly at mesoscopic length scales. One is to engineer particle interactions so that they assemble into desired structures without any outside forces [12, 13, 14]. Another is concerned with how matter or energy input into a self-assembling system affects the structures that result [15, 16, 17]. In this work, we focus on the first approach, and specifically, how the interactions of particles of size between nanometers and micrometers – referred to as “solutes” or “colloids” – and the fluid they are immersed in lead to self-assembly of those colloids. A consistent theme throughout this work is the search for the minimal model that captures a set of phenomena.

This work will focus on two areas of interest in soft matter. *The first is the study of self-assembly of solutes within fluids with high ionic strength, such as molten salts and ionic liquids.* In addition to numerous industrial applications, these “ionic fluids” support a range of rich phenomena that can serve to increase scientific understanding of self-assembly on a general level. For example, the formalism introduced in Chapter 2 and used throughout later chapters also applies in a broad range of other soft matter systems, including block copolymers [18, 19] and lipid membranes [20]. Thus, a study of self-assembly in ionic fluids will enrich our understanding of self-assembly in soft matter in general. Further, the long-

range correlations that characterize ionic fluids with high ionic strength are challenging to treat, and indeed, are an area of open interest, as recent experimental reports of long-ranged correlations have defied theoretical explanation [21, 22, 23]. *The second area is concerned with how nematic liquid crystal droplets interact with, and are shaped by, colloids.* The ability of colloids to influence the shapes of fluid droplets is reminiscent of cellular processes that occur with incredible consistency and precision, such as cell division [5].

To be specific, we first provide an introduction, in Chapter 2, of some key concepts about ionic fluids to establish some of the background of the field. In this chapter we also introduce some of the formalism that we will use through much of this work. And to motivate the need for new physical models, we discuss a recent set of experiments by the Israelachvili, Perkin, and Ducker labs [21, 22, 23] which demonstrate unexplained physical phenomenon in high ionic strength solutions. Next, we detail a study of a lattice model, the frustrated Ising model, that we extended to study high ionic strength fluids in a coarse-grained manner [24] in Chapter 3. The frustrated Ising model is a minimal model that nonetheless captures key elements required for a framework to describe both low and high ionic strength fluids, and by virtue of its simplicity, the corresponding mean field theory serves as a useful framework that we return to throughout the rest of our work on ionic fluids. Our simulations of the lattice model, using a custom code which I have written in its entirety and which is available online, allow us to extend our results beyond mean field theory, and show under what conditions the mean field theory breaks down. In Chapter 4, we discuss a work examining the unexpected observation that nanocrystal colloids within molten inorganic salts do not precipitate out of solution [25]. We provide evidence that the stability of the colloids is a result of their strong interactions with the ionic fluids, and that linear response and a mean field theory can explain a surprising amount of the physics that leads to colloidal stability. A follow-up to that study is reported in Chapter 5, and includes an additional set of measurements by my experimentalist collaborators of the structuring of ionic liquids and molten salts due to

nanocrystal colloids [26], providing more evidence for the hypothesis we advance in Chapter 4. An important feature of this study is the clear demonstration of physics beyond the linear response regime that is still open to explanation. A currently unpublished continuation of the frustrated Ising work is the subject of Chapter 6, in which we generalize the frustrated Ising model and add solute- or colloid-like objects to bring the model more directly in line with the questions studied in the previous two works on colloids in ionic fluids. At this point, we change the focus from ionic fluids to another soft matter system in Chapter 7 and lay out a study of the interactions between elongated nematic liquid crystal droplets (called “tactoids”) and colloids. Finally, we sum up the themes of this work and discuss intriguing future directions in Chapter 8.

CHAPTER 2

IONIC FLUIDS: A BRIEF INTRODUCTION

One of the chief questions we will be addressing in the next few chapters is whether nanocrystal colloids will remain in solution or precipitate out of a molten salt or ionic liquid solvent. Setting aside numerous practical applications [27, 28], there are two main reasons this is an interesting question. First, because these colloids prove to remain in solution [25], despite the contrary predictions of traditional frameworks. Thus, there is some underexplored physics and chemistry to attend to. Second, because the measured decay length of forces between plate-like solutes within high ionic strength solutions was recently reported and has not yet been explained with theory or simulation [21, 22, 1, 23]. As we will see, these two aspects are related because the way that a surface of a colloid or plate interacts with a fluid is integrally tied to how multiple colloids or plates interact. To address the question of nanocrystal colloid solubility, we need to introduce a number of theoretical tools, some of which are surprisingly effective despite their simplicity.

Fundamentally, the question of whether colloids remain within solution is a matter of whether there is an interaction between colloids that is repulsive enough to resist the attractive van der Waals interactions between them – which leads to colloids remaining in solution – or not – which leads to aggregation and precipitation from solution [29]. A repulsive force can result from how a fluid responds to a colloid [30], and we will be detailing ways in which this can occur throughout the present chapter (in particular, see Section 2.3). Thus, in order to derive colloid-colloid interactions, we need to understand how the fluid will respond to a single colloid. Through linear response and the fluctuation-dissipation relation, which we introduce in Section 2.2, we can relate the fluid response to a colloid with the correlations within an unperturbed fluid. Then our method of study is to begin by examining the correlations within a fluid, next turn our attention to colloid-fluid correlations, and then finally, to our goal of fluid-mediated colloid-colloid interactions. In the studies that follow in

Chapters 3–6, we pair these simple tools with both molecular and coarse-grained simulation techniques in order to help bridge the gap between these minimal theoretical models and the real world to some extent.

The chapter is laid out as follows. In Section 2.1, we introduce the foundational work describing the correlations within ionic fluids, the Debye-Hückel (or DH) theory. The DH theory, though effective, is limited in its range of application to dilute ionic fluids, and much of this document is dedicated to pushing beyond this dilute regime. Next, we describe the linear response and fluctuation-dissipation relations in Section 2.2, which we will return to throughout this text. The linear response relation describes a first approximation of the response of a fluid to a perturbing potential, and as such, is strictly limited to weak perturbations. It is surprising how effective this approximation is in the context of strongly-interacting fluids, as we will see in Chapters 4 and 5. We detail the concept of colloidal stability in Section 2.3, before applying linear response concepts to find the correlations induced by colloids within a DH fluid. From these correlations, we can achieve our goal of computing the free energy of interaction between colloids. However, this result is limited to the dilute ion regime, and we are interested in pushing to higher ionic strengths; we will return to tools developed in this section once we have developed a theory of high ionic strength fluids in Chapters 3 and 4. In Section 2.4, we summarize some recent experimental results which provide a clear demonstration of the need to go beyond DH and DLVO to understand these high ionic strength fluids. An important feature missing from the DH framework is an accounting for the correlations between ions. To address this, we make a brief digression in Section 2.5 to outline some basic concepts about spatial correlations from the theory of liquids. Finally, in Section 2.6, we discuss some of the attempts to incorporate ion-ion correlations into theories of ionic fluids, which will serve as a basis for our understanding moving forward into the next chapter.

2.1 The theory of Debye and Hückel

The Debye-Hückel theory is derived using a number of assumptions and a key electrostatics equation: the Poisson equation, which describes the electrostatic potential due to a distribution of charge. Here, we are chiefly interested in the correlations between ions in a fluid, and the correlations induced by a solute within a solution of ions; hence we will be focusing exclusively on these aspects of the theory. The interested reader is referred to the literature for a more expansive review of the DH theory [31, 32, 33]. Proceeding, the Poisson equation is written

$$\nabla^2 V(r) = -4\pi\phi(r), \quad (2.1)$$

where the 4π factor occurs due to our choice to use Gaussian, rather than SI, units.¹ Here, $V(r)$ is the electrostatic potential and $\phi(r)$ is the charge density.² Importantly, we will consider the average configuration induced by a set of boundary conditions – which might represent a charged particle fixed at the origin, a charged plate, or some other simple geometry – within a fluid of charges which are dilute and modeled as a continuous field – in other words, the response due to a perturbation. There may be other, uncharged particles in the fluid (such as water molecules in an aqueous solution of ions), but their only effect is to add a uniform background contribution, which is accounted for by the dimensionless relative permittivity. For notational convenience, we incorporate the relative permittivity into the parameter Q , which describes the strength of the electrostatic interaction and has units of charge². Because of our simplistic treatment of any possible background uncharged molecules, the equations we derive will apply equally well to a dilute solution of ions in water

1. In Gaussian units the Coulomb interaction is $\sim 1/r$ in real space or $\sim 4\pi/k^2$ in Fourier space; further, there is no permittivity of free space, though the dimensionless relative permittivity may appear. Here, the relative permittivity is incorporated into a constant, Q , which describes the strength of the electrostatic interaction.

2. Throughout this work, the choice of units is as follows. The charge density $\phi(r)$ has units $1/\text{length}^d$, for d the dimension, and the electrostatic potential $V(r)$ has units of energy/charge² (which is equivalent to $1/\text{length}$ in Gaussian units). Further, charge valences q_j will be unitless, and frequently ± 1 , and a parameter Q with units charge² will be used.

as to a high temperature gas of ions, provided the assumptions we discuss below hold. For our purposes, we consider two different cases: the potential and charge distribution with respect to a point charge q fixed at the origin in a dilute fluid of point charges, and that of a charge, q , fixed at the origin with hard sphere radius σ in a dilute fluid of charges with hard sphere radius σ (in the limit that $\sigma \rightarrow 0$, these cases become identical).

Since the system of charges is at equilibrium, we use the Boltzmann distribution to write down the distribution of charges, $\phi(r)$, in the fluid due to the charge fixed at the origin, not yet specializing to a point charge or a charged hard sphere:

$$\begin{aligned}\phi(r) &= \sum_j q_j \rho_j \exp(-\beta w_j(r)) \\ &\approx \sum_j q_j \rho_j \exp(-\beta Q q_j V(r)),\end{aligned}\tag{2.2}$$

where q_j is the valence of charge j , ρ_j is the concentration of particles of the same type as particle j , $\beta = (k_B T)^{-1}$ is the inverse thermal energy, k_B is the Boltzmann constant, and in the second line we approximate the potential of mean force $w_j(r)$ with $Q q_j V(r)$, ie. the pair interaction energy. Replacing the potential of mean force with a pair potential is a first-order approximation for very dilute systems, ie. $\exp(-\beta w(r)) \xrightarrow{\rho \rightarrow 0} \exp(-\beta v(r))$ for $v(r)$ an arbitrary pair potential, see discussion in Hansen and McDonald, Chapter 2. [34]. Here, the approximation only holds when the electrostatic interaction overwhelms all other interactions at all separations. This is equivalent to treating ions in the dilute limit, and fails even for the simple case of a fluid of charged hard spheres (ie. hard spheres with point charges at their centers) at moderate concentration [35]. Note that Eq. 2.2 applies for all r when the origin charge is a point charge, but only for $r > \sigma$ when the particles have an excluding volume.

We can combine the Poisson and Boltzmann equations, 2.1 and 2.2, to make the aptly

named Poisson-Boltzmann equation, and then linearize:

$$\begin{aligned} \nabla^2 V(r) &= -4\pi \sum_j q_j \rho_j \exp(-\beta Q q_j V(r)) \\ &\xrightarrow{\beta Q q_j V(r) \rightarrow 0} -4\pi \sum_j q_j \rho_j (1 - \beta Q q_j V(r)) \end{aligned} \quad (2.3)$$

Having linearized, we have made a second assumption. Just as the electrostatic interaction outweighed all other interactions, so too the thermal energy outweighs the electrostatic interaction (ie. $\beta Q q_j V(r) \ll 1$). Now we have a second order, inhomogeneous differential equation in the potential. The homogeneous solution is

$$V_h(r) = \frac{A}{r} \exp(-\kappa_D r), \quad (2.4)$$

with

$$\kappa_D = \sqrt{\frac{4\pi Q \sum_j q_j^2 \rho_j}{k_B T}}, \quad (2.5)$$

which is an inverse length scale that is variously referred to as the inverse Debye screening length and the Debye constant. The Debye screening length is a fundamental parameter which measures the strength of electrostatic interactions relative to the thermal energy and will be used throughout this work, see further discussion in Section 2.1.1. The particular solution is $V_p(r) = 1/(\beta Q q_j)$ and is unimportant for our purposes since we are interested in the charge density.

The electroneutrality condition, which requires that the ion cloud cancel out the charge at the origin, can be used to fix the constant A . From the Poisson equation, Eq. 2.1 and the DH potential Eq. 2.4, the charge density due to an origin point charge is

$$\phi_{pc}(r) = -\frac{A_{pc} \kappa_D^2}{4\pi r} \exp(-\kappa_D r), \quad (2.6)$$

and so the electroneutrality condition becomes

$$0 = q + 4\pi \int_0^\infty dr r^2 \phi_p(r) \quad (2.7)$$

from which $A_{pc} = q$. The only difference when including the hard sphere is that the integral in the electroneutrality constraint, Eq. 2.7, starts from σ rather than 0, as the fluid cannot access the excluded volume. Then for the hard sphere case, the normalization constant is found to be $A_h = \frac{q}{1+\kappa_D\sigma} \exp(\kappa_D\sigma)$, leading to a charge distribution of

$$\phi_{hs}(r) = -\frac{q\kappa_D^2}{1+\kappa_D\sigma} \frac{1}{4\pi r} \exp(-\kappa_D(r-\sigma)). \quad (2.8)$$

Thus, the DH theory predicts that an ion fixed at the origin within a continuum fluid of dilute charge induces an exponentially decaying cloud of charge of the opposite valence. It predicts that this cloud of charge has amplitude depending on the valence of the central charge, the Debye constant, and, for a hard sphere origin charge, σ . And it predicts that the cloud of charge decays over a length scale determined by the Debye constant.

2.1.1 *The Debye constant, or inverse screening length, κ_D*

Before moving on, it is worth spending some time to dwell on the Debye constant (or, equivalently, the inverse Debye screening length), κ_D (defined in Eq. 2.5) as it will be mentioned frequently through Chapters 3–6. The Debye constant defines the electrostatic length scale, and can be read as a measure of the ratio of the electrostatic and thermal energies. It will be seen that the Debye constant, in combination with another length scale such as the size of charged particles, σ , will be an important determining factor for when the DH theory can be applied with reasonable effectiveness. When $\kappa_D\sigma$ is small, the electrostatic length scale is much larger than the ion size, which validates the assumptions we made above in Section 2.1, namely, (1) the neglect of all interactions between particles except for electrostatics, and,

(2), that even electrostatics is overwhelmed by thermal energy. What happens when $\kappa_D\sigma$ approaches and eventually surpasses 1? Non-electrostatic interactions with length scale of the same order as the ion size may begin to play a role. Even neglecting other interactions, the inclusion of a hard sphere interaction will become increasingly important. The Debye-Hückel theory will no longer serve us well, and we will need to appeal to approaches that account for the other interactions, and hence correlations, between particles.

Throughout this work, we will be interested in the effects of varying the inverse Debye screening length, $\kappa_D\sigma$, upon the measured inverse screening length, $\kappa_s\sigma$. When the DH theory works well, ie. for $\kappa_D\sigma \ll 1$, this is a trivial question, as the measured screening length and Debye screening length are equivalent, $\kappa_s \rightarrow \kappa_D$. However, as the DH theory begins to break down for larger values of $\kappa_D\sigma$, we will find that $\kappa_s\sigma \neq \kappa_D\sigma$. It will turn out that the way in which we vary $\kappa_D\sigma$ seems to have little effect on the resulting measured screening length, $\kappa_s\sigma$. Thus, we can imagine a variety of different methods to vary $\kappa_D\sigma$: changing the concentration of ions in solution, changing the solvent (and hence the permittivity), changing the valence of ions, changing the size of ions, or varying the temperature. We will alter whichever is most convenient: in experiments to date, it will often be the case that changing the concentration is easiest, while in our simulation work, we will mainly focus on varying the temperature. Ultimately, the important parameter seems to be the Debye constant relative to the ion size, $\kappa_D\sigma$.

In the next section, we outline some of the tools that we use to relate the correlations within an unperturbed fluid and the response of a fluid to the inclusion of a colloid, which we will leverage later to compute the free energy of interaction between two colloids.

2.2 Linear response: the connection between liquid-liquid correlations and solute-liquid interactions

The response of a liquid to a small perturbation – ie. the linearized approximation to the response or the “linear response” – is integrally tied to the fluctuations of the fluid when unperturbed [34]. A small perturbation can be a liquid particle fixed at the origin, or a solute plate, provided the interaction with the fluid is not too strong, and so linear response gives us access to the correlations induced by a solute within a liquid.

Let’s examine a simple toy model to illustrate the procedure that we will use to extract the structure of a fluid due to a perturbation. To extract the response function, which characterizes the response of the fluid to perturbation, we will write down a simple model of a dilute ionic fluid (which will turn out to equivalent to the DH theory!), starting with the Hamiltonian. The partition function and free energy can be written down with the Hamiltonian in hand, and we will extract the linear response relation and a form of the fluctuation-dissipation relation from functional derivatives of the free energy. We will then specialize to a mean field free energy using the saddle-point approximation to simplify the formalism for future use in Chapters 3–6, because in our case, at temperatures far about any phase transition, the mean field free energy has everything we need and the formalism is simplified. An additional reason to make the saddle-point approximation is that it allows connection with other mean field theories, such as the one developed starting from a lattice in Section 3.6. Functional differentiation of the mean field free energy gives us another route to the linear response relation. Finally, we use the linear response relation to compute the density profiles due to a point particle fixed at the origin and due to a plate-like solute. We discuss some of the consequences of the linear response relation for these density profiles.

We start with a model fluid with a coarse-grained, continuum order parameter field, $\phi(\mathbf{r})$, that describes the local deviation from uniform charge density at each point, ie. $\phi(\mathbf{r}) = \rho_+(\mathbf{r}) - \rho_-(\mathbf{r})$ with $\rho_\pm(\mathbf{r})$ the local density of + or – ions. We can write down

a phenomenological, Landau-Ginzburg-style Hamiltonian [36, 37, 38, 39]:

$$H[\phi] = \frac{\sigma^3}{2} \int d^3r a [\phi(\mathbf{r})]^2 + \frac{\sigma^3}{2} \int d^3r d^3r' \rho Q \phi(\mathbf{r}) V(|\mathbf{r} - \mathbf{r}'|) \phi(\mathbf{r}'), \quad (2.9)$$

with σ a coarse-graining parameter with units of length,³ a a parameter dependent on temperature (here, $a \sim k_B T$ with k_B the Boltzmann constant), ρ the uniform density of ions, $V(r)$ the electrostatic potential derived from the Poisson equation, here for point charges, $V(r) \sim 1/r$, and Q a parameter controlling the strength of the electrostatic interaction (as introduced in the last section). In Fourier space⁴ it can be written

$$\begin{aligned} H &= \frac{\sigma^3}{2} \int \frac{d^3k}{(2\pi)^3} \left| \tilde{\phi}(\mathbf{k}) \right|^2 \left[a + \frac{4\pi\rho Q}{k^2} \right] \\ &= \frac{1}{2} \int \frac{d^3k}{(2\pi)^3} \left| \tilde{\phi}(\mathbf{k}) \right|^2 \tilde{\chi}^{-1}(k), \end{aligned} \quad (2.10)$$

where in the second line, we define the function

$$\tilde{\chi}(k) = \frac{1}{a\sigma^3} \frac{1}{k^2 + \kappa_D^2}, \quad (2.11)$$

known as the response function, which will play an important role as we soon discuss. Here, $\kappa_D^2 \equiv 4\pi\rho Q/a$ is the Debye constant, compare with Eq. 2.5. The Hamiltonian defined above describes the energy of an unperturbed dilute fluid of ions. We are also interested in the

3. In the derivation of a Landau-Ginzburg theory from a lattice model in Section 3.6, σ is the lattice length. In a system not constrained to the lattice, it might instead be the relevant correlation length, particle size, or mean spacing between particles. That derivation also shows that the “square gradient” term which commonly appears in Landau-Ginzburg field theories is due to nearest neighbor interactions, and so neglecting it as we do here is analogous to the “dilute ions” approximation made in the DH theory.

4. Fourier conventions are described in Appendix Section 9.2.

case where an external potential, $h(\mathbf{r})$, perturbs the fluid, which can be written

$$\begin{aligned} H_{ext} &= - \int d^3r h(\mathbf{r})\phi(\mathbf{r}) \\ &= - \int \frac{d^3k}{(2\pi)^3} \tilde{h}(\mathbf{k})\tilde{\phi}(-\mathbf{k}). \end{aligned} \quad (2.12)$$

The partition function for our fluid, Z , is written

$$\begin{aligned} Z &= \int \mathcal{D}\phi \exp \left[-\beta \left(H[\phi] - \int d^3r h(\mathbf{r})\phi(\mathbf{r}) \right) \right] \\ &= \int \mathcal{D}\phi \exp \left[-\beta/2 \left(\int \frac{d^3k}{(2\pi)^3} \chi^{-1}(k) |\tilde{\phi}(\mathbf{k})|^2 - 2\tilde{h}(\mathbf{k})\tilde{\phi}(-\mathbf{k}) \right) \right], \end{aligned} \quad (2.13)$$

where $\int \mathcal{D}\phi$ indicates a functional integral, ie. an integral which samples every possible value of $\phi(\mathbf{r})$ at every point \mathbf{r} , $\beta = (k_B T)^{-1}$ is the inverse thermal energy, and in the second line we have written the argument of the exponential in Fourier form. Here, we will use the external potential for two purposes. First, to perturb the fluid from its uniform ground state. Second, to learn about the relation between fluctuations in the unperturbed fluid and the response of the fluid to perturbations, which we do now.

Because the partition function functional integral in Eq. 2.13 is Gaussian in the charge density $\tilde{\phi}$, we can use a continuum limit extension of Gaussian integration to compute the partition function, which has the form [37, 39]

$$Z \sim \exp \left(\beta/2 \int \frac{d^3k}{(2\pi)^3} \chi(k) |\tilde{h}(\mathbf{k})|^2 \right). \quad (2.14)$$

Functional derivatives of the free energy, $F = -k_B T \log Z$, with respect to the external field, \tilde{h} then give the following results [37, 39]

$$\frac{\delta F}{\delta \tilde{h}(-\mathbf{k})} = \langle \tilde{\phi}(\mathbf{k}) \rangle = \chi(k) \langle \tilde{h}(\mathbf{k}) \rangle, \quad (2.15)$$

where the middle expression is found by differentiation of Eq. 2.13 and the right expression is found from differentiation of the result Eq. 2.14. Differentiating twice gives

$$\frac{\delta^2 F}{\delta \tilde{h}(-\mathbf{k}) \delta \tilde{h}(\mathbf{k}') } = \left\langle \tilde{\phi}(\mathbf{k}) \tilde{\phi}(\mathbf{k}') \right\rangle = k_B T \chi(k) \delta(\mathbf{k} + \mathbf{k}'). \quad (2.16)$$

The first expression, Eq. 2.15, tells us that the presence of an external field \tilde{h} , will lead to an average density profile $\langle \tilde{\phi} \rangle$ which is the product of the external field and the response function, $\chi(k)$. We will use this linear response relation frequently in the rest of this work. The second expression, Eq. 2.16, is a form of the fluctuation-dissipation relation that relates the fluctuations of the unperturbed fluid, ie. the Fourier form of the charge-charge correlation function $\langle \tilde{\phi}(\mathbf{k}) \tilde{\phi}(\mathbf{k}') \rangle$ to the response function, ie. $\chi(k)$ which encodes information about how the fluid relaxes in the presence of perturbations. This second result also allows us to immediately find both the response function and the charge-charge correlation function upon writing down a Hamiltonian that is quadratic in ϕ , which can be seen easily in Eq. 2.10.

Now, we simplify the free energy expression for future use. We do so because the mean field expression is sufficient for our purposes going forward, and its simplicity allows for clearer manipulation and connections to other mean field formalisms (compare, for example, with the results of the derivation of a variational mean field theory of a lattice model in Section 3.6). There exists some special charge density, $\phi^*(\mathbf{r})$, that minimizes the Hamiltonian H subject to the external potential $h(\mathbf{r})$. We will approximate the functional integral for Z in Eq. 2.13 with the contribution from only this ϕ^* . This is known as the saddle-point approximation, and the intuition driving it is that the exponential weighting in the partition function will make other contributions negligible relative to the one from ϕ^* . In the saddle-

point approximation, the mean field free energy can be written

$$\begin{aligned} F_{mf} [\phi^*] &= -k_B T \log \left(\exp \left[-\beta \left(H [\phi^*] - \int d^3r h(\mathbf{r}) \phi^*(\mathbf{r}) \right) \right] \right) \\ &= H [\phi^*] - \int d^3r h(\mathbf{r}) \phi^*(\mathbf{r}). \end{aligned} \quad (2.17)$$

Small fluctuations about the mean field ϕ^* can be accounted for using standard Gaussian integration techniques [37, 39]. For the models that we study later in this text (eg. Section 2.6 and 3.6), the correction due to Gaussian fluctuations is only important near the critical point (which for those models separates a “high temperature” phase in which charge correlations decay exponentially with distance from a “low temperature” phase in which they persist throughout the entire fluid) [40, 41, 19, 42]. Therefore, throughout this document, we start from the mean field free energy in the saddle point approximation, unless otherwise noted (such as in Section 3.6 where we derive a similar Landau-Ginzburg-style mean field free energy starting from a lattice). We will use the notation F , rather than F_{mf} and ϕ rather than ϕ^* for simplicity, but it is understood that we are writing down the mean field versions of these variables.

Proceeding, we write down the mean field free energy explicitly:⁵

$$\begin{aligned} F &= \frac{\sigma^3}{2} \int d^3r a [\phi(\mathbf{r})]^2 - h(\mathbf{r}) \phi(\mathbf{r}) + \frac{\sigma^3}{2} \int d^3r d^3r' \rho Q \phi(\mathbf{r}) V(|\mathbf{r} - \mathbf{r}'|) \phi(\mathbf{r}') \\ &= \frac{\sigma^3}{2} \int \frac{d^3k}{(2\pi)^3} |\tilde{\phi}(\mathbf{k})|^2 \left[a + \frac{4\pi\rho Q}{k^2} \right] - \tilde{h}(\mathbf{k}) \tilde{\phi}(-\mathbf{k}), \end{aligned} \quad (2.18)$$

The perturbation of the fluid due to a potential can be derived in a different method than in Eq. 2.15, namely by extremizing the free energy using the Euler-Lagrange equation, discussed in Appendix Section 9.1.2. Application of the result of that analysis, Appendix

5. In the derivation of the mean field free energy of an ionic fluid starting from a lattice in Section 3.6, the source of the first term with prefactor a is the lowest order part of an expansion of the entropy.

Eq. 9.6, to the mean field free energy, Eq. 2.18, leads to

$$\begin{aligned}\frac{\delta F}{\delta \tilde{\phi}(-\mathbf{k})} &= \sigma^3 \left[a + \frac{4\pi\rho Q}{k^2} \right] \tilde{\phi}(\mathbf{k}) - \tilde{h}(\mathbf{k}) \\ &= \tilde{\chi}^{-1}(k) \tilde{\phi} - \tilde{h}(\mathbf{k}),\end{aligned}\tag{2.19}$$

where in the second line, the inverse response function $\tilde{\chi}^{-1}(k)$, defined in Eq. 2.11 has been substituted in. The free energy is extremized when the functional derivative is 0, and so

$$\tilde{\phi}(\mathbf{k}) = \tilde{\chi}(k) \tilde{h}(\mathbf{k}).\tag{2.20}$$

Confirming our previous linear response result in Eq. 2.15, Eq. 2.20 should be read as saying that, when perturbed, the order parameter field responds in a manner that is dictated by the product of the response function with the external potential, to first order. In real space, this equation would take the form of a convolution, but its content would remain unchanged.

This is a powerful result. The usefulness of this linear response relation, Eq. 2.20, can be seen by considering the effect that placing an idealized particle into a fluid will have. Placing a particle at the origin in a fluid can be recast as placing an external potential – the potential due to a particle at the origin – upon the fluid. Then, the structuring of a fluid due to a particle at the origin can be found using the linear response function and the pairwise potential of particles in the fluid. Thus, the response function contains information that describes the structuring of the fluid, a manifestation of the fluctuation-dissipation relation. In a similar manner, the response function can be used to compute the correlations induced by a solute within a fluid. Specifically, if the solute is considered to be an infinite plate with normal in the positive- z direction, the order parameter field can be determined by computing the product of the inverse response function and the potential of the infinite plate.

In the two cases just discussed, the simplest model of the perturbing potential is a delta function at the origin. In the case of a particle fixed at the origin, a model potential can be

written

$$h_3(\mathbf{r}) = \epsilon_3 \sigma^3 \delta(\mathbf{r}) = q\epsilon_3 \sigma^3 \delta(x)\delta(y)\delta(z), \quad (2.21)$$

with ϵ_3 a constant with units of energy that controls the strength of the local interactions between the fixed particle and the fluid. Using this model potential and the linear response relation Eq. 2.20 gives a charge density

$$\tilde{\phi}(k) = \frac{q\epsilon_3}{a} \frac{k^2}{k^2 + \kappa_D^2}, \quad (2.22)$$

which leads, upon inverse Fourier transformation, to a perturbed solvent profile that goes as

$$\phi(r) = -\frac{q\epsilon_3}{a} \frac{\kappa_D^2}{4\pi r} \exp(-\kappa_D r). \quad (2.23)$$

Comparing to the result of the DH theory for a central point charge, Eq. 2.6, we have exactly the same result within a prefactor that describes the temperature-scaled potential due to the point charge. Thus, the Hamiltonian Eq. 2.9 and the corresponding saddle-point mean field free energy Eq. 2.18 are shown to correspond to the DH dilute fluid of charges. However, armed with the mean field free energy and linear response formalism, we can go beyond our DH results and compute the charge density induced by the inclusion of solutes. For an infinite plate with normal in the z -direction, a similar model potential to describe the surface-fluid interaction is

$$h_1(z) = q\epsilon_1 \sigma^3 \delta(z), \quad (2.24)$$

leading to a solvent profile:

$$\phi(z) = -\frac{1}{2} \frac{q\epsilon_1}{a} \kappa_D \exp(-\kappa_D z). \quad (2.25)$$

We emphasize again that the decay profile is dictated by the length scale $1/\kappa_D$ that depends

exclusively on the properties of the fluid as encoded in the response function – the role of the particle at the origin or the solute is only to perturb the fluid, influencing the prefactor.

Now with a formalism, admittedly approximate, for relating the correlations in an unperturbed bulk fluid to the response of a fluid due to a solute, we proceed to study the stability of colloids within dilute ionic fluids. The DLVO model we develop in the next section is limited in its range of application because we use the DH set of assumptions, but the techniques we develop are surprisingly applicable to more complicated models, such as the one developed in Chapter 3, which better account for high ionic strength fluids. We will discuss this further in Chapter 4.

2.3 DLVO theory and Derjaguin approximation

Colloids are solute particles within a solvent. They encompass a broad ranges of both solutes and solvents, and are important in a wide range of contexts. A few examples include milk, where globules of fat and protein are dissolved within an aqueous solution; nanoparticles with bulky ligands in organic solvents; proteins interacting within a lipid bilayer membrane [43]; charged solutes in ionic fluids [29]; and water-droplets within a bulk nematic [44]. A fundamental question in colloidal science is whether the colloids will stay dispersed in solution for a given period of time, ie. if they are colloidally stable. Colloidal stability is a constant battle between the attractive van der Waals interaction, which biases colloids to come together (or “flocculate”), and some repulsive interaction, which varies depending on the specifics of the colloid and solvent system. Two of the main repulsive interactions that frequently appear in colloidally stable systems are steric repulsion and “double layer” electrostatic forces. The repulsive force is steric in the case of nanoparticles with bulky ligands mentioned above: two nanoparticles are prevented from assembling too closely because such a configuration would necessitate significant overlap between their respective bulky ligand “clouds”. “Double layer” forces occur when charged solutes, whose charged surface is the first of the two

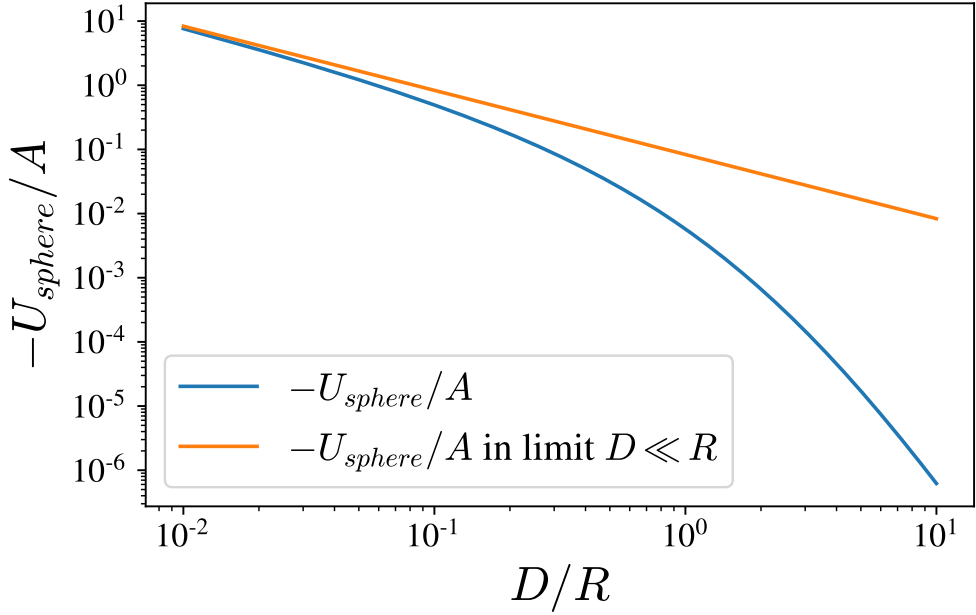


Figure 2.1: The van der Waals interaction energy of two spheres of radius R at a distance of closest approach D . The exact expression is shown in blue, while the short distance ($D \ll R$) limit is plotted in orange.

layers in the “double layer”, are placed within dilute electrolyte solutions, which respond by associating a cloud of opposite charge near the surface forming the second of the layers, and are the subject of the DLVO theory, which will be discussed in more detail in the next section.

To make the discussion more concrete, consider two solutes interacting within a fluid medium via van der Waals (vdW) interactions. Let us assume that these solutes are close to one another, which allows us to neglect the time it takes for the electrons involved to react to one another; this is known as the “nonretarded” limit [29]. The interaction energy can then be written down as [29]

$$U_{plate}(D) = -\frac{A}{12\pi} \frac{1}{D^2}, \quad (2.26)$$

for two large plates with separation D , or [29]

$$U_{sphere}(D) = -\frac{A}{6} \left[\frac{2R^2}{(4R+D)D} + \frac{2R^2}{(2R+D)^2} + \log \frac{(4R+D)D}{(2R+D)^2} \right], \quad (2.27)$$

for two spheres of radius R and with distance of closest approach D . In the limit that $D \ll R$, the interaction energy between spheres simplifies to

$$U_{sphere}(D) = -\frac{AR}{12D}. \quad (2.28)$$

In both of these expressions, A is the Hamaker constant, which contains information about the material of the solutes that are interacting as well as the medium they are interacting through [29]. Figure 2.1 shows a plot of the sphere interaction energy versus separation, D . The Hamaker constant can be computed via the Lifshitz theory [29], but in the media and solutes we will be considering, $A \sim 5 \times 10^{-20} J$ [25, 26].

The Hamaker constant is often small enough that at large separations, the vdW interaction is weak, but when the separation is small, the power law nature of the interaction means that it can overwhelm repulsive interactions. Then, for colloids to be stable, there needs to exist a repulsive potential between them which, at some separation, outweighs the vdW potential. For example, see Fig. 2.2, which compares the vdW interaction to a mock repulsive potential. At a separation of $\sim 0.25R$, the sum of the two potentials peaks at $\sim 2k_B T$. This mock potential showcases that colloidal stability is often a matter of kinetics, rather than thermodynamics. In the case of Fig. 2.2, a fluctuation of energy $\sim 2k_B T$, which occurs relatively frequently, will be sufficient for the colloids to cross the barrier and find the global free energy minimum at $D = 0$, irreversibly binding. Frequently, the term “stable colloids” refers to colloids that are not thermodynamically stable, but instead have a potential peak much larger than $k_B T$ and, hence, will not flocculate over any reasonable time scale.

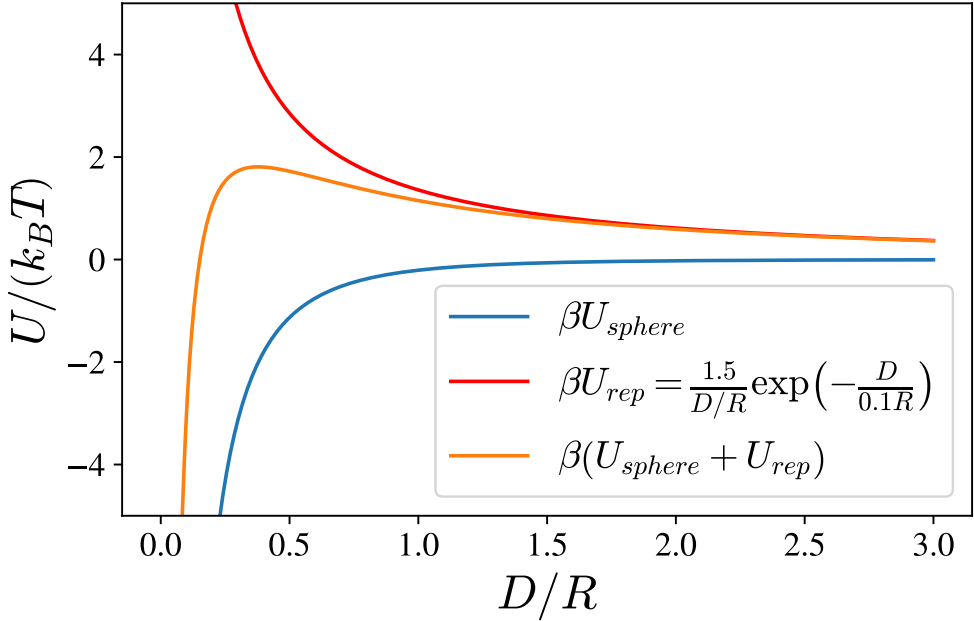


Figure 2.2: The van der Waals interaction energy of two spheres of radius R at a distance of closest approach D paired with a mock repulsive, exponential potential.

2.3.1 The DLVO theory for flat plates

The Derjaguin-Landau-Verwey-Overbeek, or DLVO, theory is concerned with the interaction between solutes with surface charge in a dilute ionic solution, and can be used to predict whether these solutes will be colloidally stable. The DLVO theory describes the competition between the van der Waals interaction, introduced above, and a repulsive interaction due to the correlations between the charged colloid surface and ions in solution. Ions in solution are treated in a DH paradigm, which means that all the approximations used in deriving the DH theory apply here. The solute surface charge leads to a diffuse cloud of ions around each solute, which act to repel other solutes with their own clouds of charge. Much like repulsive steric interaction between ligands attached to a colloid surface, the accumulation of a dilute cloud of charge around each solute in the DLVO theory leads to a free energy penalty when these clouds overlap. Our ultimate goal is to study the stability of spherical colloids within ionic fluids, but as a first step, we will consider a plate-like solute. We will then map

the interaction free energy between plates to spherical colloids using an approximation first derived by Derjaguin.

We now provide a brief derivation of the DLVO theory from a linear response perspective. Readers interested in a more traditional approach through the electrical potential are referred to standard texts [29].

The strategy will be to take the charge density of the fluid induced by a single charged plate and to superpose that charge density with that of an equivalent plate a distance D away. When plates are separated by a large distance, $D \gg 1/\kappa_D$, an even simpler approximation may be employed, namely, to approximate the two-plate profile up to the midplane by a single-plate profile. As the plates approach from very large separations, the magnitude of the charge density at the midplane begins to increase from 0 as the plates are no longer completely screened out. The free energy due to the fluid as a function of separation, D , is related to the “unscreened” portion of the charge density within expressions for the entropy and electrostatic energy of the fluid [45, 46]. After computation of the “double layer” free energy, the stability of the system can be determined by adding the free energy to the van der Waals energies of the two plates: if a barrier much larger than the thermal energy results, the colloids are said to be stable (see discussion in previous section).

From the past discussion of the DH theory in Sections 2.1 and 2.2, we know the response function, Eq. 2.20. The charge density within a dilute ionic fluid induced by a plate was also found, see Eq. 2.25. For convenience, define $\phi_0 \equiv -q\epsilon_1\kappa_D/(2a)$, so that $\phi(z) = \phi_0 \exp(-\kappa_D z)$.

The charge density induced by two plates a distance D away from each other is approximated by the simple superposition of two single-plate charge densities. For plates with surfaces at 0 and D ,

$$\phi_2(z) = \phi(z) + \phi(-z + D) \quad (2.29)$$

When $D \gg 1/\kappa_D$, we can further approximate the superposed charge density profile up to

the midplane by the one-plate charge density profile:

$$\phi_2(z) \xrightarrow{D \gg 1/\kappa_D} \phi(z), \quad z < D/2. \quad (2.30)$$

We use the free energy for a DH fluid, Eq. 2.18, as a starting point, except here, due to the one-dimensional symmetry of the plate-plate system, the free energy has an additional prefactor $1/A$ which represents the area of the plate, and integration occurs only over z and then only over a specific portion of z . To compute the free energy for the two-plate system, let the separation be large, $D \gg 1/\kappa_D$. When the separation tends to the limit, the free energy tends to a constant. As the separation decreases, the charge density at the midplane starts to increase. This occurs because the fluid does not have enough space to fully screen the surface charge of each plate. The free energy cost of the plate-fluid system at a separation D is proportional to the magnitude of the unscreened charge [45, 46], or equivalently, to the charge density due a single plate beyond the midplane, $D/2$:

$$\begin{aligned} F(D) &= \frac{\sigma^3}{2A} \int_{D/2}^{\infty} dz a [\phi_2(z)]^2 + \frac{\sigma}{2} \int_{D/2}^{\infty} dz \int_{D/2}^{\infty} dz' \rho Q \phi_2(z) V(|z - z'|) \phi_2(z') \\ &\sim \frac{a \phi_0^2 \sigma}{\kappa_D} \exp(-\kappa_D D). \end{aligned} \quad (2.31)$$

Thus, the interaction between charged plates within a dilute solution of ions decays with the same length scale, $1/\kappa_D$, that characterizes the correlations between ions in an equivalent bulk solution.

The colloidal stability of a particular solute-solvent system can be evaluated by taking the sum of the free energy due to the solute-solvent interaction, discussed here, and the van der Waals energy (see Section 2.3). When the electrostatic energy outweighs the vdW energy at any separation by many multiples of the thermal energy, the colloids are said to be stable. Because the DLVO theory follows DH in treating ions in solution, smaller Debye constant (ie. lower ion concentration or higher temperature) leads to increasing stability.

Up to this point, we've only discussed the stability of plate-like colloids, but it is much more common that colloids are spherical. Fortunately, there is a simple approximation that allows for the computation of the interaction between large spherical colloids in terms of the interaction between plates. As we will see later in this work in Chapters 4 and 5, small spherical colloids require some additional considerations (“small” or “large” size is relative to the separation between particles), but for now, we lay out the Derjaguin approximation [29].

2.3.2 The Derjaguin approximation

Consider two large spherical colloids, each with radius R , at a separation D , with $D \ll R$. To compute the interaction between spheres, here, say a general function $g_{sphere}(D)$ that can be specialized to force per area or energy per area later, imagine that the surface of the spheres are divided up into rings, radius r , which are interacting at a distance $z(r)$. The rings have radius $2\pi r dr$, and so the interaction between spheres can be written, using $g_{plate}(D)$ as the interaction between flat plates per unit area, as

$$g_{sphere}(D) = 2\pi \int_0^\infty dr r g_{plate}(z), \quad (2.32)$$

where the upper bound of the integral at ∞ is due to the large colloid assumption. The change of variables from $r \rightarrow z$ can be found using the diagram in Fig. 2.3, specifically

$$\begin{aligned} z &= D + 2R(1 - \cos(\theta)) \\ &\xrightarrow{r \ll R} D + \frac{r^2}{R}. \end{aligned} \quad (2.33)$$

The limit in the second line can be made due to the assumption that $D \ll R$, since the colloid is so large relative to the interaction length scale that the interaction is assumed to die out by the time $r \sim R$.

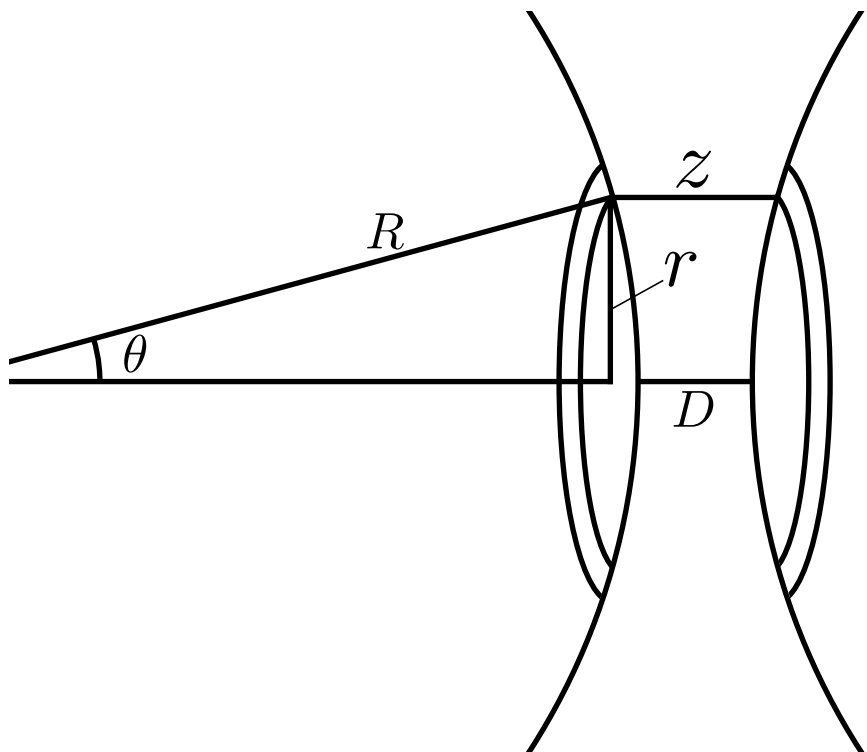


Figure 2.3: Schematic of the geometry used to derived the Derjaguin approximation. Two spheres of radius R have a distance of closest approach D , with $D \ll R$. The interaction between spheres is approximated as the integral of the interaction between plates a distance z apart over ring-like area sections of area $2\pi r dr$.

The change of variables in the integral in Eq. 2.32 can then be performed:

$$g_{sphere}(D) = \pi R \int_D^\infty dz g_{plate}(z). \quad (2.34)$$

If the g functions here are forces per area, then the integral on the right hand side becomes the interaction energy between the two plates, ie.

$$f_{sphere}(D) = \pi R U_{plate}(D). \quad (2.35)$$

The Derjaguin approximation tells us that spherical and plate-like colloids interact with the same decay length and differ only by a prefactor. We will return to the Derjaguin approximation in Chapter 4, where we study quasi-spherical nanocrystal colloids in molten salts and ionic liquids. There, the assumptions of dilute ions of the DH and DLVO theories are patently false, and new plate-plate interactions will have to be developed. Nonetheless, with only slight modifications, the Derjaguin approximation allows us to transfer these plate-plate interactions into sphere-sphere ones.

Next, we introduce some recent experimental results that highlight the breakdown of the DH and DLVO theories. These results serve to motivate our development of theory to treat the high ionic strength regime.

2.4 Selected experiments beyond the Debye regime

2.4.1 Measurements of screening lengths

Recent advances in surface-force apparatus techniques pioneered by the Israelachvili lab have allowed for the measurement of screening lengths in fluids with high ionic strength [21, 22, 1]. The experiment consists of the immersion of quartz or gold plates within a solvent, and the variation of the separation between the plates. The apparatus allows for careful measurement

of the force on, and the distance between, the plates. The results have been surprising. The first measurement was reported by Gebbie and coworkers [21] of an ionic liquid (BMIM-N_{Tf}₂), and showed that the screening length was far in excess of the predictions of the DH theory (ie. $\kappa_s > \kappa_D$, where κ_s is the measured screening length), and that the repulsive force was monotonic. They proposed that the ionic liquid should not be considered as fully dissociated, but instead as a percolating network, with only a small fraction of ions dissociated and able to screen. With fewer ions available to screen, the DH theory might still be valid.

After the work of Gebbie et al. [21, 47], members of the Perkin lab, initially skeptical [48, 49], confirmed Gebbie et al.'s experimental results, and extended the measurements to a variety of solvent systems over a range of concentrations [22, 1]. They found that the screening length followed a non-monotonic trend, see Fig. 2.4. For $\kappa_D\sigma \ll 1$, they found that the screening length and Debye length were equivalent, $\kappa_s\sigma \sim \kappa_D\sigma$. At around $\kappa_D\sigma \sim 1$, however, the screening length began to trend as $\kappa_s\sigma \sim (\kappa_D\sigma)^{-2}$. Lee and coworkers [1] proposed a scaling argument to explain the observed screening length trend and the monotonic nature of the repulsion. The physical picture they proposed was of high ionic strength fluids as similar to ionic crystals with many defects. Ionic crystals do not screen because the ions that make them up are immobilized within a crystal lattice. However, allowing for mobility of defects leads these defects to carry an effective charge. Thus, they propose that the effective charge carriers within these dense ionic fluids are defects, and not the ions themselves, which allows a reduction in the concentration of effective charge carriers and allows the application of DH for these carriers. To date, no statistical mechanical theory or molecular simulation has confirmed this proposed physical picture.

More recently, Gaddam and Ducker [23] reported another measurement of screening lengths in high ionic strength ionic fluids using a different experimental apparatus. Rather than a surface force apparatus, they used a thin, sloping crack between a silicon wafer bonded

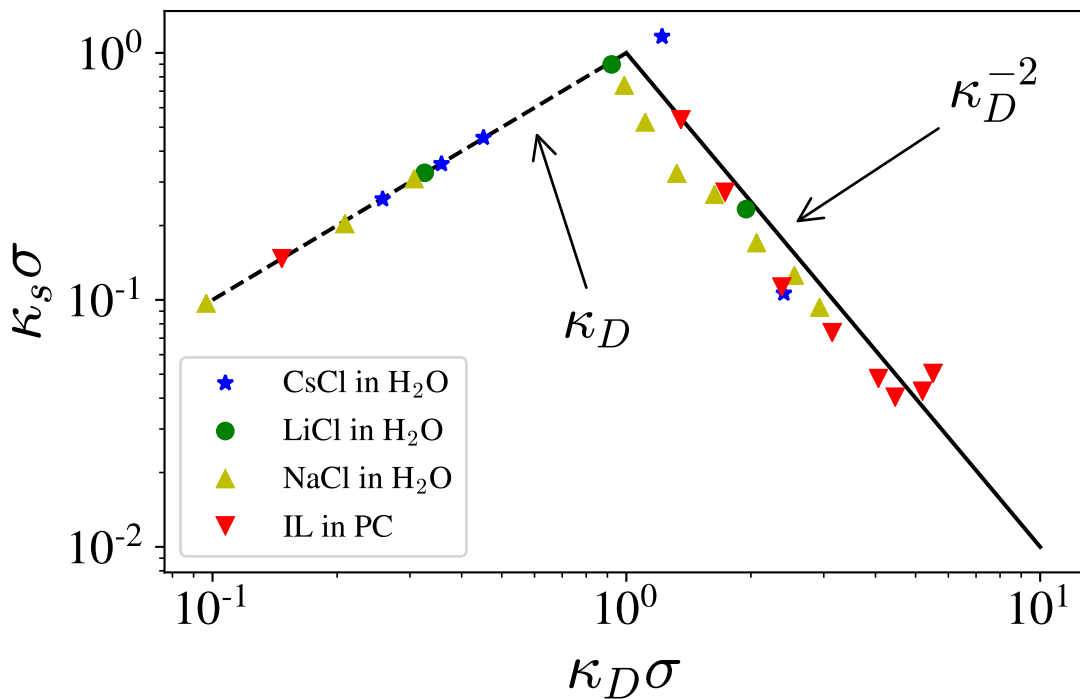


Figure 2.4: Measurement from Lee et al. [1] surface force aparatus experiments showing the measured screening length, $\kappa_s\sigma$ as a function of the Debye constant, $\kappa_D\sigma$, both scaled by the estimated ion size σ . The measurement is for a variety of ionic fluids and shows that for small Debye constant, the Debye-Hückel theory makes accurate predictions of the screening length. However, increasing the Debye constant past the inverse ion size, $\kappa_D\sigma > 1$, leads to a break from the DH theory, and specifically, a scaling of $\kappa_s\sigma \sim (\kappa_D\sigma)^{-2}$. Data reproduced from Ref. [1] with permission.

to a glass wafer. The crack was filled with aqueous solutions of LiCl, CsCl, or NaCl over a wide concentration range (0.5-10 M), with a small concentration of a fluorescein ion. They characterized the distance between the crack surfaces at each point using the interference of one color of light, and measured the concentration of fluorescein at each point based on its fluorescence intensity. They reported the same trend of screening length as the Perkin lab.

We highlight what we view to be a few key results of the Israelachvili, Perkin, and Ducker labs. First, the interaction between plates is shown to be monotonic. As we will see in our discussion of some theories that go beyond DH in Section 2.6, the high ionic strength regime is predicted to have an oscillatory charge density. We might reasonably suspect that an oscillatory charge density implies an oscillatory interaction between solutes (we confirm this in Chapter 4). Thus, it appears that some new physics is involved in producing these long-range monotonic forces, perhaps a reduction in ions available to screen as suggested above [21, 1]. Second, the trending of the screening length as $\kappa_s\sigma \sim (\kappa_D\sigma)^{-2}$ is intriguing. Though different theories, discussed in Section 2.6 and 3.4, disagree as to how the screening length should trend, none of them predict it to scale with the power -2 . Finally, the results hold for a wide range of solvent systems and two different experimental apparatus, which indicate that these results are not just due to, for example, some unexpected effect in bulky ionic liquids, but are instead a fundamental feature of fluids with high ionic strength. These experiments provide the motivation to study a general, minimal framework for ionic fluids in Chapter 3.

2.4.2 Unexpected stability of nanocrystals in molten salts and ionic liquids

Molten salts and ionic liquids have been used for, or proposed to be used for, a variety of scientific and industrial endeavors. These include thermal energy storage for photovoltaic power plants [50] and as synthesis environments for a broad range of materials, including nanoparticles [27] and pharmaceutical products. Recent work in the Talapin lab has demon-

strated that a variety of bare nanocrystals (or NCs), including semiconductors such as CdSe and metals such as Pt, are colloidally stable in certain molten salts and ionic liquids [25, 26]. This is surprising because established mechanisms such as steric or electrostatic stabilization through the DLVO theory cannot be applied here. Dispersions of NCs might be used to modify the thermal conductivity of a molten salt [50], increasing efficiency as an energy storage/transfer medium, or as a means to alter local concentrations of reactants within an ionic liquid synthesis environment. Molten salts or ionic liquids might also be useful synthesis environments for NCs themselves. On the theoretical front, theory and simulation of charge-dense fluids remain an underexplored subject. Molecular dynamics simulations are expensive, and much of the theory applies only for dilute solutions of ions. As discussed in the past section, standard wisdom in the field of ionic liquids regarding ion dissociation and screening length has recently been overturned by new experimental results, indicating the need for new theory [21, 22, 1]. We began a collaboration with the Talapin lab to study the colloidal stability of NCs in charge-dense fluids [25, 26], and these studies are detailed in Chapters 4 and 5. We found, using molecular dynamics models, that mean field theory and linear response could explain a surprising number of the results, but there were some clear breakdowns of the theory and MD models as well.

Before discussing some recent work on the theoretical front to study ionic fluids with high ionic strength in Section 2.6, we take a brief detour to introduce some liquids state concepts. These will help give us useful intuition for the high ionic strength regime which, as we will see, theory suggests can be thought of as having “liquid-like” correlations between ions, contrasting to the low ionic strength DH regime with “gas-like” ion correlations.

2.5 Spatial correlation functions and the structure of liquids

The liquid state is a consistent backdrop in the work that follows, and so it behooves us to briefly review some of the basics of how liquid structure is described. Due to the fluctuation-

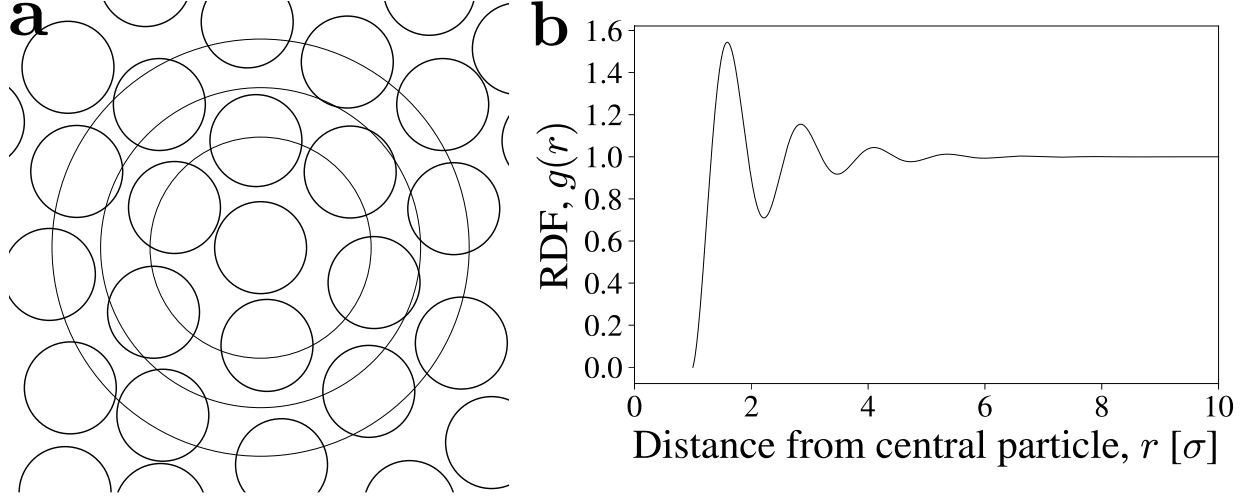


Figure 2.5: Cartoons showing structuring in a simple liquid of hard spheres in two dimensions. (a) Cartoon of two-dimensional hard sphere fluid. Particles are arranged roughly in concentric shells. The concentric circles are meant as guides the eye to draw attention to the arrangement into concentric shells. (b) The radial distribution function, or RDF, $g(r)$, captures the correlations between particles at a distance r from a particle fixed at the origin. The normalization is such that a value of 1 corresponds to the ideal gas, or uncorrelated, case.

dissipation relation, discussed in Section 2.2, the structure of an unperturbed liquid provides detailed information about how that liquid will respond to the inclusion of a solute. With information about the bulk structure, then, predictions can be made about how solutes interact with fluids and, as a result, with each other.

The reader is referred to standard statistical mechanics texts for a derivation of the pair distribution function, which characterizes the spatial correlations between particles [34, 51], see cartoon in Fig. 2.5a. Physically, the pair distribution function is a measure of the probability that, given a particle fixed at \mathbf{r} , another particle is observed at position \mathbf{r}' . It is normalized such that it tends to 1 in the large separation limit, $|\mathbf{r} - \mathbf{r}'| \rightarrow \infty$, as the particles become uncorrelated, similar to an ideal gas. One way to express the result of standard derivations is

$$g_{\alpha\beta}(\mathbf{r}, \mathbf{r}') = \left\langle \sum_i^N \sum_{j \neq i}^N \delta_{t_i}^\alpha \delta_{t_j}^\beta \delta(\mathbf{r} - \mathbf{r}_i) \delta(\mathbf{r}' - \mathbf{r}_j) \right\rangle, \quad (2.36)$$

for an N particle system of types $\{t_i\}$, where $\alpha, \beta \in \{t_i\}$, δ_λ^η is 1 if $\eta = \lambda$, and zero otherwise, $\delta(r)$ is 1 if $r = 0$ and 0 otherwise, and $\langle \dots \rangle$ denotes an ensemble average. In isotropic systems, $g_{\alpha\beta}(\mathbf{r}, \mathbf{r}') \rightarrow g_{\alpha\beta}(r)$ and the function becomes known as the radial distribution function. A mock radial distribution function is plotted in Fig. 2.5b, which shows the characteristic exponentially damped oscillations which decay to 1, indicating that particles have become uncorrelated. The peaks roughly correspond to the packing of concentric shells of particles around a central one, see Fig. 2.5a for a cartoon.

A closely related spatial correlation function is referred to as the density-density correlation function which measures fluctuations in the density:

$$\begin{aligned} G_{\alpha\beta}(\mathbf{r}, \mathbf{r}') &= \langle [\rho_\alpha(\mathbf{r}) - \langle \rho_\alpha(\mathbf{r}) \rangle][\rho_\beta(\mathbf{r}') - \langle \rho_\beta(\mathbf{r}') \rangle] \rangle \\ &= \langle \rho_\alpha(\mathbf{r}) \rangle \langle \rho_\beta(\mathbf{r}') \rangle (g_{\alpha\beta}(\mathbf{r}, \mathbf{r}') - 1) + \langle \rho(\mathbf{r}) \rangle \delta(\mathbf{r} - \mathbf{r}'), \end{aligned} \quad (2.37)$$

where $\rho(\mathbf{r}) = \sum_i^N \delta(\mathbf{r} - \mathbf{r}_i)$ is the local density and $\rho_\alpha(\mathbf{r}) = \sum_i^N \delta_{t_i}^\alpha \delta(\mathbf{r} - \mathbf{r}_i)$ is the local density of type α . As we saw in Section 2.2 the structure of the fluid, encoded in the density-density correlation function, provides information about how the fluid responds to perturbations such as the inclusion of solutes, a property that we will make extensive use of in our description of the interactions between solutes and fluids.

In ionic fluids, which will be the subject of the large part of this work, the charge-charge correlation function supersedes the density-density correlation function in importance to some degree. It is defined somewhat similarly to the density-density correlation function as

$$\begin{aligned} G_q(\mathbf{r}, \mathbf{r}') &= \langle [\rho_q(\mathbf{r}) - \langle \rho_q(\mathbf{r}) \rangle][\rho_q(\mathbf{r}') - \langle \rho_q(\mathbf{r}') \rangle] \rangle \\ &= \sum_{i \in \{+, -\}} \sum_{j \in \{+, -\}} \langle \rho_i(\mathbf{r}) \rangle \langle \rho_j(\mathbf{r}') \rangle q_i q_j g_{ij}(\mathbf{r}, \mathbf{r}') + \langle \rho(\mathbf{r}) \rangle \delta(\mathbf{r} - \mathbf{r}'), \end{aligned} \quad (2.38)$$

where $\rho_q = \sum_i^N q_i \delta(\mathbf{r} - \mathbf{r}_i)$ is the local charge density and $q_i = +1$ when $i = +$ and $q_i = -1$ when $i = -$.

Next, we discuss some recent theoretical frameworks that have been developed to treat the correlations between ions in ionic fluids, which DH theory neglects. As we will see, we can think of the high ionic strength regime as having “liquid-like” correlations between ions, while the DH regime has “gas-like” ones. This intuition will be further developed in Chapter 3.

2.6 Selected theory beyond Debye and Hückel

A variety of theoretical techniques have been used to extend the DH theory to the high $\kappa_D\sigma$ regime. The literature is extensive, and we only discuss a few examples, but the common thread amongst these works is the more careful accounting for correlations, or short-range interactions, between ions. One such method was by Attard, who used a standard closure from the theory of liquids [35]. In that work, he writes out the correlation functions for charged hard spheres, also known as the restricted primitive model (or RPM), and uses the hypernetted chain approximation in order to produce a closure for the Ornstein-Zernicke equation. Another approach was developed by Kjellander and coworkers [52, 53, 54], who incorporate the short-range correlations into an effective ion atmosphere or “dressing” of the ions. A third approach was pioneered by Lee and Fisher who studied the effect of a perturbing oscillatory potential that intuitively arises from the preference of oppositely charged ions to arrange in alternating layers [55]. Some more recent works have built on and simplified these past works including work by Frydel [56], who showed how a treatment of a finite-sized charge as having some distribution (such as Gaussian) within its spherical radius could lead to a non-DH regime, and work by Adar et al. [57] showing that accounting for the finite size of ions can provide a simple route to the non-DH regime. We will discuss the method of Adar et al. [57] momentarily in Section 2.6.1, as their method complements work to be discussed later in Chapter 3.

The unifying feature of all the theories mentioned above is a regime at large $\kappa_D\sigma$ where

spatial correlations between ions cannot be ignored as they are in the DH theory [32]. Indeed, the manifestation of these correlations as oscillations in the charge density was predicted long ago by Kirkwood [58]. In this large $\kappa_D\sigma$ regime, the charge correlation length can become much longer than the screening length predicted by DH theory, qualitatively similar to observations of anomalous screening in the aforementioned surface force experiments. More recent work based both on simulations and phenomenological theories reproduce this oscillatory, large $\kappa_D\sigma$ regime [53, 59, 60, 61, 56, 62, 57]. However, none of these theoretical studies reproduces the universal scaling observed in Ref. [1]. We now discuss the model of Adar et al. [57].

2.6.1 Accounting for the finite size of ions in a continuum theory for charged hard spheres

Consider a fluid of hard sphere particles of diameter σ , which contain point charges at their centers of valence $q = \pm 1$. This model is sometimes referred to as the restricted primitive model (RPM) [35]. The goal will be to study the correlations of charges in this fluid at low temperatures or high concentrations relative to the dilute regime studied by Debye and Hückel. The free energy will take the same form as in the DH theory, Eq. 2.18, but we will modify the electrostatic potential to account for the finite size of the RPM particles. The electrostatic potential, V , is given in terms of the charge density, ϕ , by the Poisson equation, Eq. 2.1, whose Fourier form is written

$$\tilde{V}(k) = \frac{4\pi}{k^2} \tilde{\phi}(k). \quad (2.39)$$

The Coulomb interaction, $1/r$ in real space or $4\pi/k^2$ in Fourier space, is the solution to the Poisson equation for the potential due to a point charge, ie. $\phi(\mathbf{r}) = \delta(\mathbf{r})$ leading to $\tilde{\phi}(k) = 1$. Here, we modify the electrostatic potential to account for the hard sphere finite

size by postulating a modified electrostatic potential of the form

$$V(r) = \frac{1}{r} \Theta(r - \sigma), \quad (2.40)$$

where $\Theta(r)$ is the Heaviside step function, defined as

$$\Theta(r) = \begin{cases} 0 & , r < 0 \\ 1 & , r > 0. \end{cases} \quad (2.41)$$

The Fourier form of the potential, Eq. 2.40, is then

$$\tilde{V}(k) = \frac{4\pi}{k^2} \cos(k\sigma). \quad (2.42)$$

The free energy for this RPM system with modified electric potential, Eq. 2.42, in place of the potential due to point charges, can be written from Eq. 2.18 as [57]

$$F = \frac{\sigma^3}{2} \int \frac{d^3 k}{(2\pi)^3} \left| \tilde{\phi}(\mathbf{k}) \right|^2 \left[a + \frac{4\pi\rho Q}{k^2} \cos(k\sigma) \right] - \tilde{h}(\mathbf{k}) \tilde{\phi}(-\mathbf{k}), \quad (2.43)$$

and following from Section 2.2, the response function can be read off from the free energy as

$$\tilde{\chi}(k) = \frac{1}{a\sigma^3} \frac{k^2}{k^2 + \frac{4\pi\rho Q}{a} \cos(k\sigma)}. \quad (2.44)$$

Then with the linear response relation, Eq. 2.20, and a simple model external potential $h(\mathbf{r}) = q\epsilon\sigma^3\delta(\mathbf{r})$, the charge density is

$$\tilde{\phi}(k) = \frac{q\epsilon}{a} \frac{k^2}{k^2 + \frac{4\pi\rho Q}{a} \cos(k\sigma)}. \quad (2.45)$$

Though the charge density, Eq. 2.45, can't be analytically inverse Fourier transformed,

there are two limits worth examining. In the limit of point charges, $\sigma \rightarrow 0$, the charge density reduces to that of the Debye-Hückel theory, with $\kappa_D = \sqrt{\frac{4\pi\rho Q}{a}}$, compare to Eq. 2.22. The other interesting limit is the small- k limit, expanding the cosine in the denominator to fourth-order and rearranging coefficients,

$$\begin{aligned}\tilde{\phi}(k) &\xrightarrow{k\sigma \ll 1} \frac{q\epsilon}{a} \left(\frac{k}{\kappa_D}\right)^2 \left[\frac{\sigma^4}{24} k^4 + \left(\kappa_D^{-2} - \frac{\sigma^2}{2}\right) k^2 + 1 \right]^{-1} \\ &= 24\sigma^{-4} \frac{q\epsilon}{a} \left(\frac{k}{\kappa_D}\right)^2 \left[k^4 + 12\sigma^{-2} \left(\frac{2}{(\kappa_D\sigma)^2} - 1\right) k^2 + 24\sigma^{-4} \right]^{-1},\end{aligned}\quad (2.46)$$

This charge density can be inverse Fourier transformed analytically. Using the second line in Eq. 2.46 with $\alpha = 6\sigma^{-2} \left(\frac{2}{(\kappa_D\sigma)^2} - 1\right)$, $\beta = 24\sigma^{-4}$, the result is, from Appendix Eq. 9.13,

$$\phi(r) = \frac{A}{4\pi r} \exp(-\kappa r) \sin(\omega r + \theta), \quad (2.47)$$

when $-\sqrt{\beta} < \alpha < \sqrt{\beta}$ (corresponding to low temperature), and, from Eq. 9.12,

$$\phi(r) \xrightarrow{r \gg 1} \frac{B}{4\pi r} \exp(-\kappa r), \quad (2.48)$$

when $\alpha > \sqrt{\beta}$ (corresponding to high temperature) with A and B normalization constants dependent on α and β , κ and ω the inverse length scales which are found by analyzing the poles of the Fourier form of the charge density function, Eq. 2.46, and θ a phase factor enforcing charge neutrality (see Appendix Section 9.3 for more details about the computation and the constants).

The key point here is that this k^4 expansion is sufficient to predict two regimes. At high temperatures, the charge density due to an origin charge decays with the same form as in the Debye-Hückel theory, while at low temperatures, the decay is oscillatory in nature. Importantly, as discussed in Appendix Section 9.3.1, the scaling of the decay length $1/\kappa$ changes between the two regimes as well. Specifically, in the high temperature regime, the

decay length increases with temperature, while in the low temperature regime it decreases with temperature. Physically, the decay length trending with respect to temperature can be understood as corresponding to “gas-like” and “liquid-like” correlations. For a gas, an increase in temperature at constant pressure leads to an expansion and, hence, an increase in the mean separation of particles. When the “gas” particles are ions, an increased mean separation means fewer ions are around to screen potentials which means that potentials persist for a longer distance. In contrast, for a liquid, an increase in the temperature means that the liquid becomes less ordered and so oscillations die out more quickly. The existence of the two screening regimes is qualitatively in agreement with the results of the Perkin lab, discussed earlier in Section 2.4 [22, 1], but there are some important differences between the k^4 theory and the experimental results. For one, in the “non-DH” regime of the theory, charge correlations are predicted to decay in an oscillatory manner, while the Perkin results are monotonic. And, as we will discuss in more detail in Chapter 3, next, the “non-DH” regime predicted by the k^4 theory does not display the same scaling of the screening length, $1/\kappa$, as the parameters of the fluid are manipulated so as to vary the Debye constant, κ_D . Motivated to understand these similarities and differences in more detail, we explore the frustrated Ising model next.

Before moving on, note that although the poles and inverse Fourier transform can’t be computed analytically for the full charge correlation function Eq. 2.45, the real space form is similar to the k^4 forms Eq. 2.47 and 2.48, (ie. it displays damped oscillatory or exponential correlations, depending on the regime) and the poles can be computed numerically. The results are qualitatively similar to the k^4 expansion. Though the full form has more information about the short-range structure and correlations of the RPM model, the expansion to fourth order in the denominator preserves the essential features.

In the next three chapters, Chapters 3–5, we use the simple tools, such as linear response, that we have developed in this chapter with surprising success to accomplish our strategic

vision of, (i) describing ion-ion correlations (Chapter 3); (ii) using linear response to find solute-ion correlations (Chapters 4 and 5); and, (iii) computing the solvent-mediated interaction between solutes (Chapters 4 and 5). However, we also find breakdowns in these simple theoretical tools, which is why our simulations in those sections are so important, as they allow us to go beyond the mean field limit. We find some experimental results that cannot be reproduced with simulation or theory (in Chapter 5), which demonstrate that, although these tools are far reaching, they do have their limits. Overall, it is surprising and heartening that such simple theoretical tools can be applied with any success at all to these complicated and strong-interacting ionic fluids. Without further ado, we introduce the charge-frustrated Ising model.

CHAPTER 3

DESCRIBING SCREENING IN DENSE IONIC FLUIDS WITH A CHARGE-FRUSTRATED ISING MODEL

This chapter reproduces material previously published in Ref. [24], with the permission of AIP publishing. That work was in collaboration with Kinjal Dasbiswas, Dmitri V. Talapin, and Suriyanarayanan Vaikuntanathan. I was the first author, and contributed to both theory and simulation portions of the work. I also wrote the simulation code from scratch.

In the past chapters we have shown that linear response ideas can be applied to dilute solutions of ions, as in the case of the DH and DLVO theories. We have also introduced one framework that uses linear response ideas to move beyond the case of dilute ions by accounting for the finite size of ions in Section 2.6.1 [57]. Here, motivated by the new physics reported by a number of experimental labs [21, 22, 23], we study a lattice model with both mean field theory and simulation to build a foundation that captures both DH and non-DH regimes with the minimum possible complexity. The mean field theory we develop turns out to be a limiting case of the theory discussed in Section 2.6.1, and so the lattice model we use here, the charge-frustrated Ising model, in a truly minimal model for these two regimes. As a minimal model, it provides a basis that we extend in the next two chapters to model systems accompanying the experimental work of our collaborators. And though we don't, in this chapter, develop the model specifically to describe the solvent response to the inclusion of solutes, the linear response formalism we've developed in the past chapter leads us to expect that we can apply the response functions that we derive here. We will return to the question of solutes in the next two chapters. For now, we will study the minimal charge-frustrated Ising model.

Charge correlations in dense ionic fluids give rise to novel effects such as long-range screening and colloidal stabilization which are not predicted by the classic Debye-Hückel theory. We show that a Coulomb or charge-frustrated Ising model, which accounts for both

long-range Coulomb and short-range molecular interactions, simply describes some of these ionic correlations. In particular, we obtain at mean field level and in simulations, a non-monotonic dependence of the screening length on the temperature. Using a combination of simulations and mean field theories, we study how the correlations in the various regimes are affected by the strength of the short ranged interactions.

3.1 Introduction

The thermodynamic properties of ionic fluids are governed by long-range Coulomb interactions between ions [32] in addition to the short-range molecular interactions present in neutral liquids. Strong electrostatic correlations lead to counter-intuitive phenomena in dense ionic fluids such as charge inversion [63, 53, 59, 60, 61, 56, 62], altered capacitance at electrode-fluid interfaces [61, 64, 65, 66], and the recently observed “anomalous screening” in surface force experiments [21, 22]. These effects could be important in the self-assembly of a variety of biomolecules [67] and soft materials [68]. Electrostatic correlations can be particularly pronounced in molten salts and ionic liquids which comprise ions alone and no neutral solvent molecules. The novel properties of such purely ionic fluids make them useful for a variety of scientific and technological applications, such as energy storage [69, 70], as industrial lubricants [71], and of serving as media capable of supporting stable colloidal nanoparticles. [25, 27].

Pure ionic fluids are ideal model systems for theoretical study of the statistical physics of strongly correlated electrostatics without the complicating ion-specific effects of hydration in aqueous solution [72]. A theoretical description of dense ionic fluids must go beyond the classic Debye-Hückel (DH) theory, which is valid only for dilute electrolytes with weak inter-ionic correlations [73], or equivalently, small inverse Debye screening length (also known as the Debye constant) in relation to the inverse molecular size: $\kappa_D \sigma \equiv \sqrt{(4\pi\rho q^2)/(\epsilon k_B T)} \sigma \ll 1$, where ρ is the concentration of ions (per unit volume), q is the unit charge, ϵ is the

dielectric constant of the electrolyte, $k_B T$ is the thermal energy, and σ is the ion diameter. Indeed, recent surface force experiments using concentrated solutions of salts and ionic liquids measure screening lengths, $1/\kappa_s$, well in excess of the DH prediction, $1/\kappa_D$, and show non-monotonic dependence of $\kappa_s \sigma$ on $\kappa_D \sigma$ [21, 22, 1]. Especially surprising is the universal scaling collapse of $\kappa_s \sigma$ when plotted against $\kappa_D \sigma$, despite the use of a range of ion types, solvent types, and ion concentrations [22, 1]. The particular scaling behavior in the dense ionic regime, $\kappa_s \sigma \sim (\kappa_D \sigma)^{-2}$, is not predicted by existing theoretical results, suggesting the need to go beyond standard approaches in the field.

A variety of theoretical techniques have been used to extend the DH theory to the strong Coulomb coupling or high $\kappa_D \sigma$ regime [74]. To take two examples, Attard uses a standard closure from the theory of liquids [35], while Lee and Fisher generalize the DH theory by considering an oscillatory potential that intuitively arises from the preference of oppositely charged ions to arrange in alternating layers [55]. Both of these theories result in a regime at large $\kappa_D \sigma$ where spatial correlations between ions cannot be ignored as they are in the DH theory [32]. Indeed, the manifestation of these correlations as oscillations in the charge density was predicted long ago by Kirkwood [58]. In this large $\kappa_D \sigma$ regime, the charge correlation length can become much longer than the screening length predicted by DH theory, qualitatively similar to observations of anomalous screening in the aforementioned surface force experiments. More recent work based both on simulations and phenomenological theories reproduce this oscillatory, large $\kappa_D \sigma$ regime [53, 59, 60, 61, 56, 62]. However, none of these theoretical studies reproduces the universal scaling reproduced in Ref. [1].

Here, we use a model framework to investigate long length scale phenomena in ionic fluids: the Coulomb or charge-frustrated Ising model (FI) [75, 76, 65], a lattice model which accounts for both the long-range Coulomb and the short-range molecular interactions present in ionic fluids. While many statistical mechanical formulations of ionic correlations treat ions as charged hard spheres within the minimal Restrictive Primitive Model (RPM) [77, 35], we call

attention here to the importance of short-range attractive interactions, such as dispersion (or van der Waals) forces. The short-range molecular interaction is included in the FI model as a nearest neighbor “ferromagnetic” interaction (similar molecular species tend to attract), and we show that it controls the crossover between the small and large $\kappa_D\sigma$ regimes. Intuitively, the length scale of the short-range interaction, l_c , competes with that of the electrostatic interaction, $1/\kappa_D$, and when the two become similar, the DH theory breaks down.

In the rest of the paper, we first introduce the FI model and its simple, continuum mean field form which is sufficient to predict a crossover in regimes between small and large $\kappa_D\sigma$. The mean field theory is only valid when the ratio of Coulomb and ferromagnetic interaction strength is small, and fails as this ratio is increased. We then present our Monte Carlo simulation results. The simulation results are quantitatively well described by the mean field theory in the limit of low Coulomb interaction strength and are in qualitative agreements with them in other regimes. The simulations allows us to comment on the screening behavior in regimes inaccessible by the mean field theory. The simulations and the mean field theory also elucidate how a short-ranged attractive interaction can modify the screening behavior of ionic fluids, such as the crossover to the strong Coulomb coupling regime as well as the scaling of the screening length with the Debye constant seen in simulations.

3.2 Model

We study the Coulomb or charge-frustrated Ising model on a three dimensional ($d = 3$) simple cubic lattice with each site occupied by a positive or negative charge as a simple model for ionic fluids. Since the positive and negative ions in an ionic fluid are chemically different species, the differences in their size or van der Waals interactions may lead to a preferential attractive interaction between like ions [65]. In this model, the charges interact through a nearest-neighbor ferromagnetic Ising interaction, representing short-range molecular attraction between like charges, as well as the Coulomb interaction. The corresponding

Hamiltonian is

$$H = \frac{1}{2} \sum_i^N \sum_{j \neq i}^N q_i \left(\frac{Q}{r_{ij}} - J_{ij} \right) q_j, \quad (3.1)$$

with N the number of lattice sites, $q_i = q_{\mathbf{r}_i} = \pm 1$ the instantaneous charge density at site i located at position \mathbf{r}_i , $Q > 0$ the Coulomb interaction strength, $r_{ij} = |\mathbf{r}_i - \mathbf{r}_j|$, and

$$J_{ij} = \begin{cases} J & i, j \text{ nearest neighbors,} \\ 0 & \text{otherwise,} \end{cases} \quad (3.2)$$

where $J > 0$ governs the strength of the Ising interaction. The ensemble average of the charge density $\langle q_{\mathbf{r}} \rangle \rightarrow 0$ in the bulk and the unit of length is the lattice length, or nearest neighbor distance, σ .

We can use the Fourier form of the charge-charge correlation function $\tilde{G}_q(\mathbf{k}) = \langle q_{\mathbf{k}} q_{-\mathbf{k}} \rangle$ (sometimes referred to as the static charge structure factor), to extract a screening length, where $q_{\mathbf{k}}$ is the Fourier transform of the instantaneous charge density $q_{\mathbf{r}}$. In the continuum limit of the mean field theory, $k\sigma \ll 1$, the Fourier form of the charge-charge correlation function has the form [65],

$$\rho^2 \tilde{G}_q(k)/T = k^2 / \left[\sigma^2 J k^4 + (T - 2dJ) k^2 + 4\pi\rho Q \right], \quad (3.3)$$

with T the temperature and the Boltzmann constant, k_B , set to 1, and $\rho = 1/\sigma^3$ in this study. The Ising critical temperature is defined by $\bar{T}_c^I \equiv 2dJ$ (overbarred variables are continuum mean field results). Inverse Fourier transforming $\tilde{G}_q(k)$ gives the charge-charge correlation function, $G_q(\mathbf{r}, \mathbf{r}') = \langle q_{\mathbf{r}} q_{\mathbf{r}'} \rangle$. The continuum $\tilde{G}_q(k)$ in Eq. 3.3 corresponds to, for an isotropic fluid at large r , the real space charge correlations given by,

$$G_q(r) = \frac{A}{4\pi r} \exp(-\kappa_s r) \sin(\omega r + \theta), \quad (3.4)$$

with A a normalization constant dependent on the parameters T, J and Q ; ω , the spatial oscillation frequency; θ , a phase factor fixed by the electroneutrality condition; and κ_s , the calculated screening constant corresponding to the decay of charge correlations. The latter may differ from the Debye inverse screening length, which for the FI model is identified with,

$$\kappa_D \equiv \sqrt{\frac{4\pi\rho Q}{T}}. \quad (3.5)$$

The phases and regimes of the FI mean field theory are revealed by examining how the inverse length scales κ_s and ω vary while changing the parameters Q, J , and T . In the rest of the paper, we fix the value of Q and treat κ_D as a parameter. By varying κ_D at fixed Q we access different temperature regimes.

Long-range modulated order characterizes the phase below the critical point [76, 20], and so the FI continuum mean field critical temperature is simply given by the temperature at which $\kappa_s\sigma \rightarrow 0$ from positive values:

$$\bar{T}_c^{FI} = \bar{T}_c^I - \sqrt{16\pi\sigma^2 J \rho Q}. \quad (3.6)$$

In this work we focus on the fluid-like regime above the critical point where there is no real long-range order ($\kappa_s\sigma > 0$). There are two regimes above the critical point which are differentiated by the value of $\omega\sigma$: when T is very high, $\omega\sigma = 0$, while at intermediate temperatures, $\omega\sigma > 0$. The transition between these two regimes occurs at

$$\bar{T}^* = \bar{T}_c^I + \sqrt{16\pi\sigma^2 J \rho Q}. \quad (3.7)$$

At high temperatures, $T > \bar{T}^*$, or equivalently, small $\kappa_D\sigma$, charge correlations decay exponentially. Further, the screening constant tends to the Debye constant when temperature is very large, $T \gg \bar{T}^*$: $\kappa_s\sigma \rightarrow \kappa_D\sigma$. This small $\kappa_D\sigma$ regime corresponds to low Coulomb

coupling, and is equivalent to the Debye-Hückel theory. For large $\kappa_D\sigma$, obtained at low temperatures (equivalent to strong coupling), oscillations with frequency $\omega\sigma$ appear in the charge correlations, while the inverse decay length $\kappa_s\sigma$ decreases with $\kappa_D\sigma$:

$$\bar{\kappa}_s = \frac{1}{2\bar{l}_c} \equiv \sqrt{\frac{T - \bar{T}_c^{FI}}{4\sigma^2 J}}, \quad T < \bar{T}^*, \quad (3.8)$$

where l_c is the mean field FI correlation length, and

$$\bar{\omega} = \sqrt{(\bar{\kappa}_s^*)^2 - (\bar{\kappa}_s)^2}, \quad T < \bar{T}^*, \quad (3.9)$$

with

$$\bar{\kappa}_s^* \equiv \left(\frac{4\pi\rho Q}{\sigma^2 J} \right)^{1/4} \quad (3.10)$$

the maximum screening constant, achieved at \bar{T}^* (see the peak in Fig. 3.1, which occurs at the $\bar{\kappa}_D^*\sigma$ corresponding to \bar{T}^* , Eq. 3.7). Thus, in the FI mean field theory, $\bar{\kappa}_D^*\sigma$ describes the transition between a DH-like regime with “gas-like” charge correlations and a second regime with “liquid-like” charge correlations where $\kappa_s\sigma$ has inverse dependence on temperature as in the DH regime: $\kappa_s\sigma \sim (\kappa_D\sigma)^{-1}$. The temperature dependence of $\kappa_s\sigma$ in the “liquid-like” regime can be seen in Eq. 3.8 when $\bar{T}_c^{FI} \ll T < \bar{T}^*$. The mean field prediction for $\kappa_s\sigma$ is plotted against $\kappa_D\sigma$ in Fig. 3.1 for $\rho Q/J = 0.5/\sigma^2$. The analogy with gas and liquid-like correlations is useful intuitively (and has been noted by others in connection with the so-called Fisher-Widom line [56]), but one important difference here is that the oscillation frequency is not fixed by the ion size, and can instead vary significantly for different $\kappa_D\sigma$ (see $\bar{\omega}\sigma$ given in Eq. 3.9).

The correlation length associated with short-range Ising interactions, l_c , defines a molecular length scale in addition to the lattice size, σ . In Fig. 3.1, we plot the inverse length scales associated with the competing interactions of the FI model: namely, the Debye con-

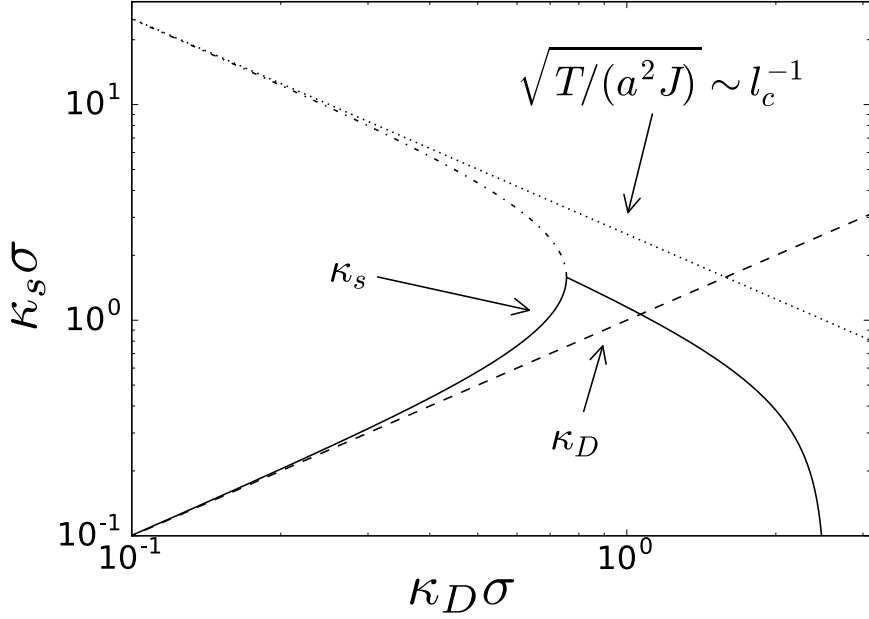


Figure 3.1: Mean field screening constant, $\kappa_s\sigma$, identified with the inverse decay length of charge correlations, displays non-monotonic trend as the Debye screening constant, $\kappa_D\sigma = \sqrt{4\pi\rho Q/T\sigma}$, (Eq. 3.5) is increased, plotted here for $\rho Q/J = 0.5/\sigma^2$. The solid black line shows the predicted screening constant, κ_s , in the two regimes. Note the inverse dependence of κ_s on T in the two regimes (see Eq. 3.8). Near, but slightly above the regime change, the screening constant from simulation shows an apparent scaling: $\kappa_s\sigma \sim (\kappa_D\sigma)^{-1}$. The dashed line shows the Debye constant $\kappa_D\sigma$, and the dotted line shows the temperature scaling of the inverse Ising correlation length $\sqrt{T/(\sigma^2 J)} \sim 1/l_c$. The dash-dotted line is a second inverse length scale which goes as $1/l_c$ for small $\kappa_D\sigma$; it merges with $\kappa_s\sigma$ at the regime change $\bar{\kappa}_D^*\sigma$, which also marks the peak in the screening constant, $\bar{\kappa}_s^*\sigma$.

stant, $\kappa_D\sigma$, originating in Coulomb interactions, and the inverse FI correlation length, l_c^{-1} , given in Eq. 3.8. The larger of the two length scales approximately determines the effective screening length, κ_s^{-1} , found within the FI model. The regime change of screening lengths in ionic fluids may then be understood in terms of these two competing length scales that are equal near the crossover point, $\bar{\kappa}_D^*\sigma$. At small $\kappa_D\sigma$, the correlations between ions are dominated by electrostatics, while at large $\kappa_D\sigma$, the short-range Ising correlations dominate. Importantly, even in the regime dominated by short-range interactions, electrostatics still plays a vital role, placing constraints on the system which appear as electroneutrality and

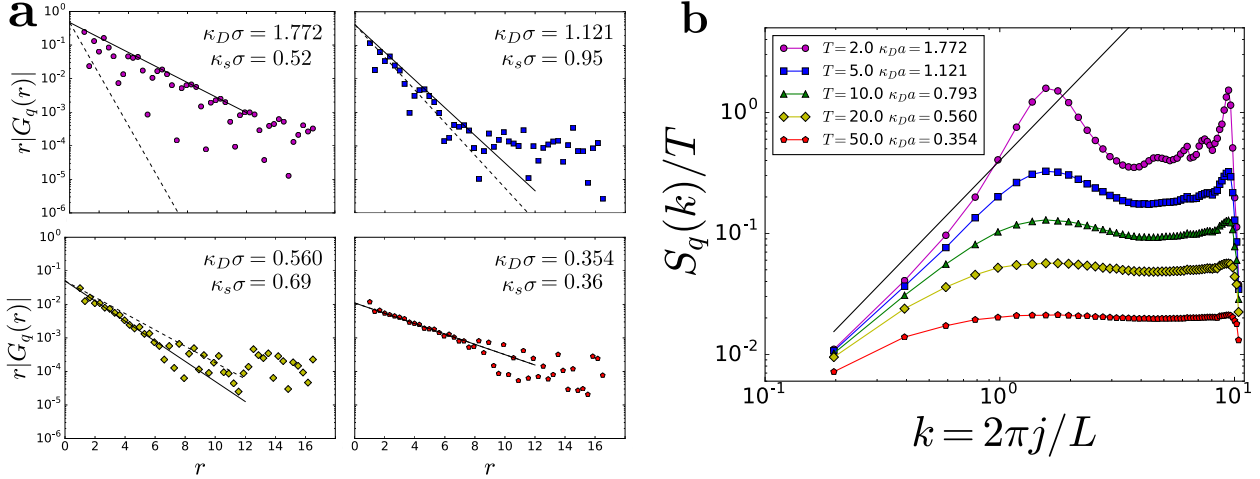


Figure 3.2: Spatial correlations in FI model for various inverse Debye screening length, κ_D , for the parameter $\rho Q/J = 0.5/\sigma^2$. **a**, absolute values of charge-charge correlation functions, $r|G_q(r)|$, plotted on log-linear scale for various Debye constants. For $\kappa_D \ll \kappa_D^*$, the correlations decay purely exponentially as shown in the bottom two plots, while oscillations appear when $\kappa_D \gg \kappa_D^*$, see the top two plots. The solid black lines correspond to the envelope of these functions from which κ_s can be extracted. The dotted black line is the DH prediction for the decay of correlations. **b**, Fourier charge correlation functions scaled by temperature, $\tilde{G}_q(k)/T$, for various κ_D . j is an integer in $[0, L]$. For small k , the correlation functions scale as k^2 (solid black line). For $\kappa_D \ll \kappa_D^*$, $\tilde{G}_q(k)$ plateaus when k becomes large, but as κ_D increases, oscillations appear. The peak at $k \sim 1$ shifts towards larger k with increasing Debye constant. The largest k value peak corresponds to the lattice length σ .

higher moment conditions [77, 35].

At large $\rho Q/J$ [$\rho Q/J > d^2/(4\pi\sigma^2)$], the continuum mean field theory breaks down, as noted by Grousson and Viot [42]. One way the breakdown in the theory can be seen is through the FI critical temperature, Eq. 3.6, which becomes unphysically negative for large $\rho Q/J$. The regime of validity can also be cast in terms of $\bar{\kappa}_s^*\sigma$, Eq. 3.10: $(\bar{\kappa}_s^*)^{-1} > \sigma/\sqrt{d}$ for validity. This form makes clear that the breakdown occurs when the minimum screening length for the system becomes similar to the lattice cell size. Grousson and Viot offer a correction by explicit treatment of the lattice [42], neglected here, and another route to improve the theory might be a more careful treatment of the finite size of ions. A third method to go beyond mean field theory, the incorporation of fluctuations, was considered

as the correlation length is strongly renormalized near the critical temperature. [40, 19] However, because the regimes we study are at temperatures far above criticality, the mean field results are not changed qualitatively. We use simulations of the FI model to investigate screening lengths and crossovers in the regime where the mean field theory breaks down.

3.3 Simulation

We perform Monte Carlo simulations of the FI model to investigate its screening length behavior, see snapshots from simulation in Fig. 3.3. We study parameter ranges strictly above the FI critical point [76]. We simulate a wide range of temperatures and extract the charge-charge correlation function, $G_q(r)$, from simulations (see Fig. 3.2a for $\rho Q/J = 0.5/\sigma^2$). For small $\kappa_D\sigma$, $\kappa_D\sigma < \kappa_D^*\sigma$, the charge-charge correlation functions trend purely exponentially as predicted by the DH theory. For large $\kappa_D\sigma$, $\kappa_D\sigma > \kappa_D^*\sigma$, oscillations develop. By fitting the envelope of $r|G_q(r)|$, which has the form of a decaying exponential (mean field, or large r , form of $G_q(r)$ shown in Eq. 3.4), we can find the screening constant for a given κ_D . We plot the trending of the screening constant with $\kappa_D\sigma$ for $\rho Q/J = 0.5/\sigma^2$ in blue dots in Fig. 3.4. For small $\kappa_D\sigma$, agreement between the DH theory, the continuum FI mean field theory, and the FI simulation is excellent. As $\kappa_D\sigma$ increases beyond $\kappa_D^*\sigma$, estimates of the screening constant from both simulations and mean field theory begin to fall, with mean field scaling as in Eq. 3.8 and simulation scaling similarly: roughly as $(\kappa_D\sigma)^{-1}$ near the screening constant peak. Overall, the agreement between the continuum mean field theory and simulation is excellent for small $\rho Q/J$. The mean field theory is still reasonable at moderate $\rho Q/J$, for example, see Fig. 3.5 where $\rho Q/J = 1/\sigma^2$.

Fitting the envelope of the charge-charge correlation function, $G_q(r)$, works well to extract the screening constant except when the screening constant is large. In principle, the oscillation frequency can also be extracted by fitting a decaying oscillatory function, such as Eq. 3.4, to simulation data directly. However, due to constraints arising from the finite

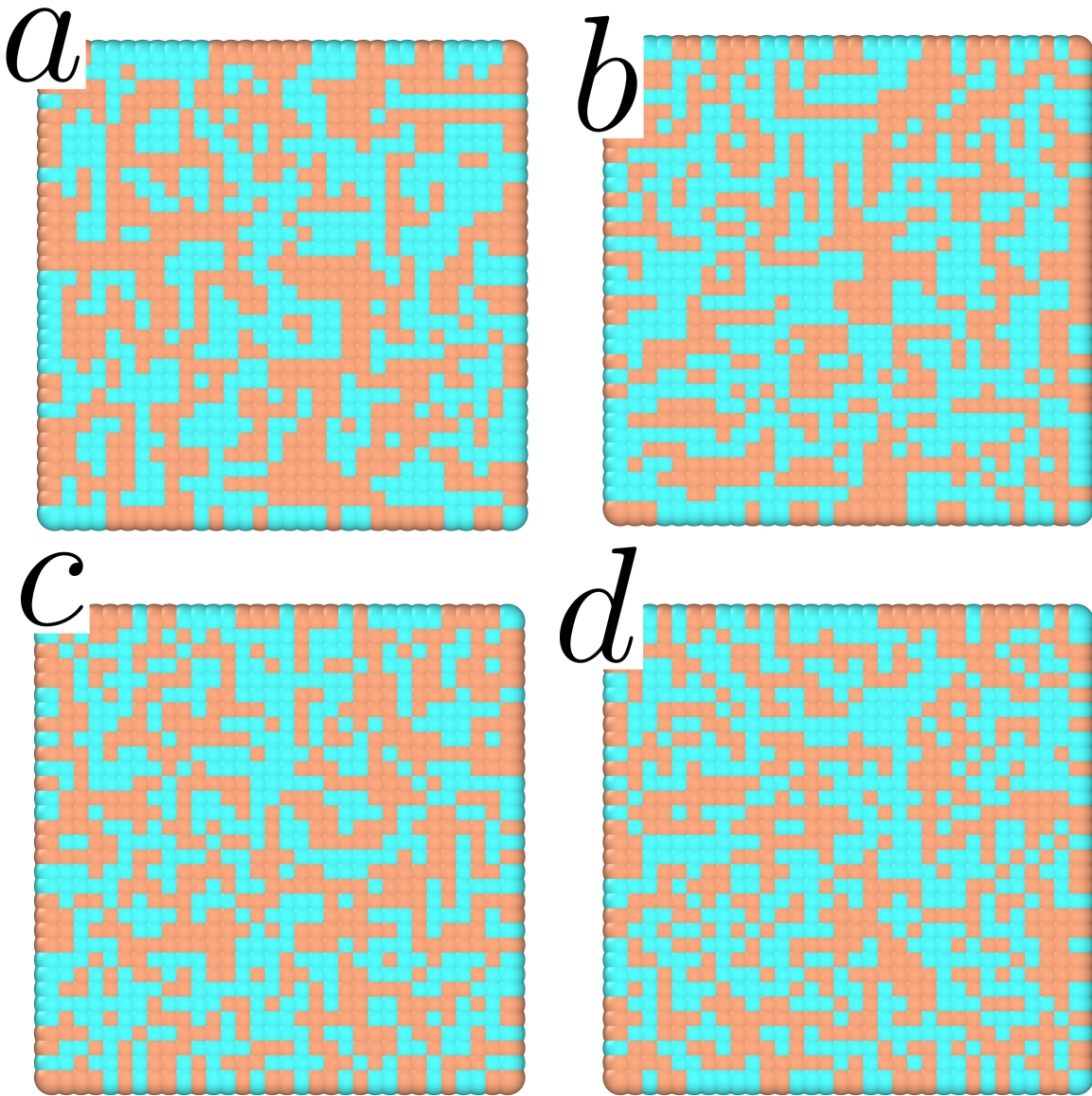


Figure 3.3: Snapshots from simulation for different temperatures with $\rho Q/J = 0.5/\sigma^2$. Plus charges are brown, minus charges are blue. Simulations are visualized using Ovito [2]. **a**, $T=3$. **b**, $T=5$. **c**, $T=20$. **d**, $T=100$.

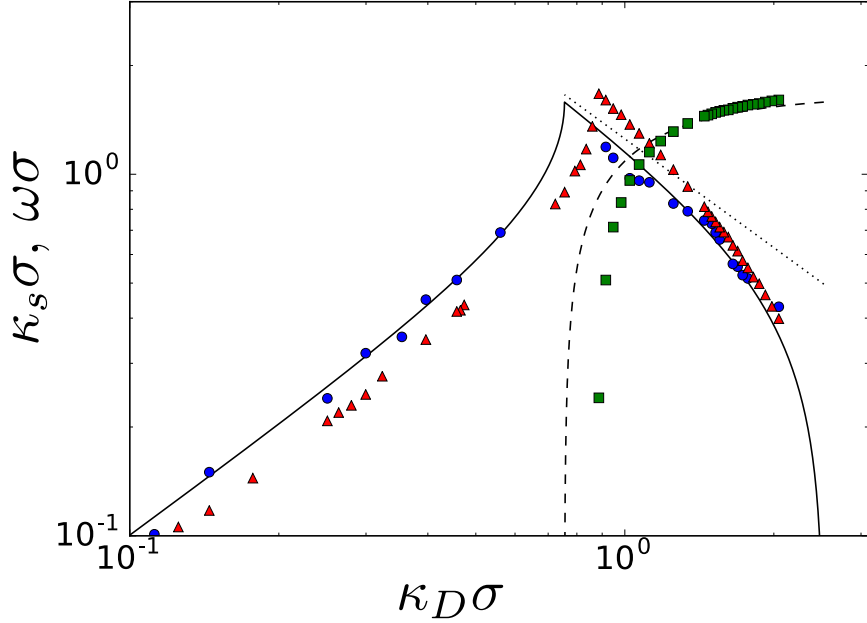


Figure 3.4: Screening constant, $\kappa_s \sigma$, for different extraction methods and oscillation frequency, all from simulation for $\rho Q/J = 0.5/\sigma^2$ and compared with theory. Solid and dashed black lines shows mean field theory prediction for screening length and oscillation frequency, respectively. Blue dots show screening constant extracted from envelope fits of charge-charge correlation functions (method shown in Fig. 3.2a). Red triangles show screening constant while green square show oscillation frequency extracted from small- k course of simulation $\tilde{G}_q(k)$ (see Simulation section). The length scales from $\tilde{G}_q(k)$ fits consistently overestimate length scale in small $\kappa_D \sigma$ regime, and underestimate it in the large $\kappa_D \sigma$ regime.

nature of the lattice, length scales extracted from such a fitting procedure can be error prone particularly in regimes where the length scale is comparable with the lattice size. We instead extract the oscillation frequency by first computing the Fourier charge-charge correlations from simulation. We use the standard definition [34]

$$\tilde{G}_q(\mathbf{k}) = \frac{1}{N} \sum_{j,l} q_j q_l \exp\left(-\frac{2\pi i}{L} \mathbf{k} \cdot (\mathbf{r}_j - \mathbf{r}_l)\right), \quad (3.11)$$

from which $\tilde{G}_q(k)$ can be easily computed; see Fig. 3.2b for some $\tilde{G}_q(k)$ from simulation with $\rho Q/J = 0.5/\sigma^2$. We then fit the large wavelength or small- k region of $\tilde{G}_q(k)$ using the

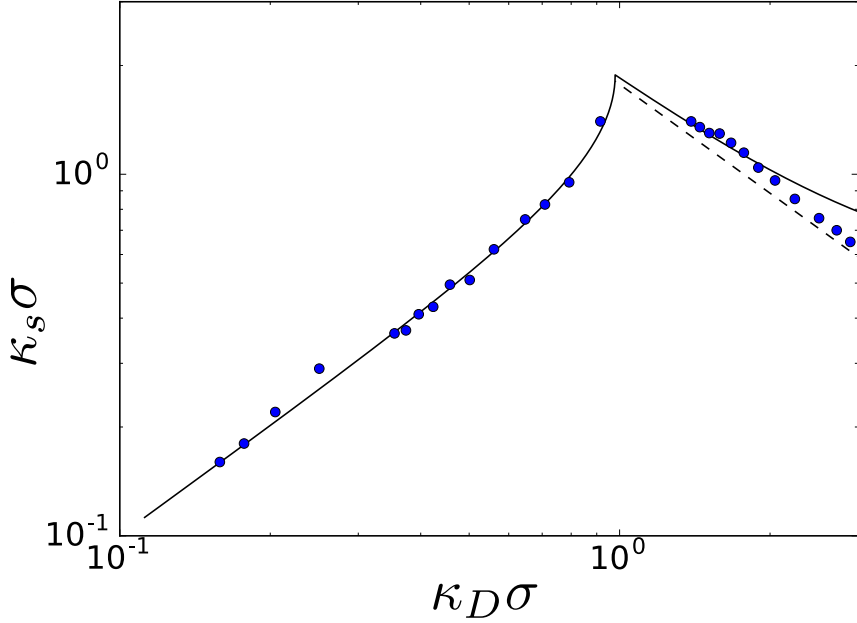


Figure 3.5: Screening constant, $\kappa_s\sigma$, displays non-monotonic trend as $\kappa_D\sigma$ is increased, shown here for $\rho Q/J = 1/\sigma^2$. Solid black line is continuum mean field theory prediction. Blue dots are screening constants extracted from the envelope of charge-charge correlation functions, $G_q(r)$, in simulations. The effect of the negative \bar{T}_c^{FI} is visible in the slight positive curvature of the mean field prediction when $\kappa_D\sigma > \bar{\kappa}_D^*\sigma$. Near, but slightly above the regime change, simulation $\kappa_s\sigma \sim (\kappa_D\sigma)^{-1}$.

inverse quartic form of the mean field expression in Eq. 3.3. As mentioned in the Model section, $\tilde{G}_q(k)$ contains information about the length scales of the system, which can be extracted from the pole,

$$k_0 = \omega + i\kappa_s, \quad (3.12)$$

with κ_s and ω the length scales appearing in the charge-charge correlation function, Eq. 3.4. Thus, fitting the small- k form to simulation $\tilde{G}_q(k)$ allows us to extract estimates of both κ_s and ω from simulation.

The values of $\kappa_s\sigma$ extracted from simulation using the large wavelength $\tilde{G}_q(k)$ fits exhibit the same qualitative trends as those extracted from charge-charge correlation fits, see Fig. 3.4. Importantly, the scaling of the two regimes, $\kappa_s\sigma \sim \kappa_D\sigma$ when $\kappa_D\sigma \ll \bar{\kappa}_D^*\sigma$ and $\kappa_s\sigma \sim$

$(\kappa_D \sigma)^{-1}$ just above the regime changeover, is the same between the two methods. When $\kappa_D \sigma$ is small, the $\tilde{G}_q(k)$ fits underpredict the screening constant. Relative to mean field, the $\tilde{G}_q(k)$ fits also predict $\kappa_D^* \sigma > \bar{\kappa}_D^* \sigma$. In the large $\kappa_D \sigma$ regime, the $\tilde{G}_q(k)$ fits overpredict the screening constant. The $\tilde{G}_q(k)$ fit inverse length scales are essentially shifted to the right with respect to mean field and charge-charge correlation fits, but capture the qualitative features.

Given the qualitative agreement between values of $\kappa_s \sigma$ estimated from direct simulations and from the fitting method described above, it is reasonable to speculate that the oscillation frequencies extracted via $\tilde{G}_q(k)$ small- k fits will capture the qualitative trends exhibited by the simulations. We compare the oscillation frequencies and screening constants extracted from the Fourier correlation function fits, to mean field predictions in Fig. 3.4. The oscillation frequency grows rapidly as $\kappa_D \sigma$ increases past $\kappa_D^* \sigma$, but saturates towards an asymptotic value as $\kappa_D \sigma$ continues to increase, in line with the continuum mean field theory ($\bar{\omega}$ given in Eq. 3.9).

We also simulate a range of ratios $\rho Q/J$ to extend our results beyond the continuum mean field theory which is only strictly valid for small $\rho Q/J$ [42]. The short ranged ferromagnetic Ising interaction, described by J , causes spins which are alike to cluster, leading to a length scale, l_c , which acts as a molecular length scale aside from the lattice length, σ . As recognized some time ago in the context of RPM models [77, 35], it is the frustration between a short-range length scale and the Coulomb length scale that results in non-DH behavior. While RPM models have a fixed molecular length scale, the hard sphere size, the FI model can potentially afford tunability of the molecular length scale, as J can be varied.

In Fig. 3.6 we plot the screening constant trending, extracted from large wavelength fits of the simulation $\tilde{G}_q(k)$, for different $\rho Q/J$ ratios. We see that $\kappa_D^* \sigma$ changes as $\rho Q/J$ is varied, but the same qualitative trends hold for all $\rho Q/J$ examined here. Namely, there are two regimes, one governed by the Debye constant, and the other governed by the inverse Ising

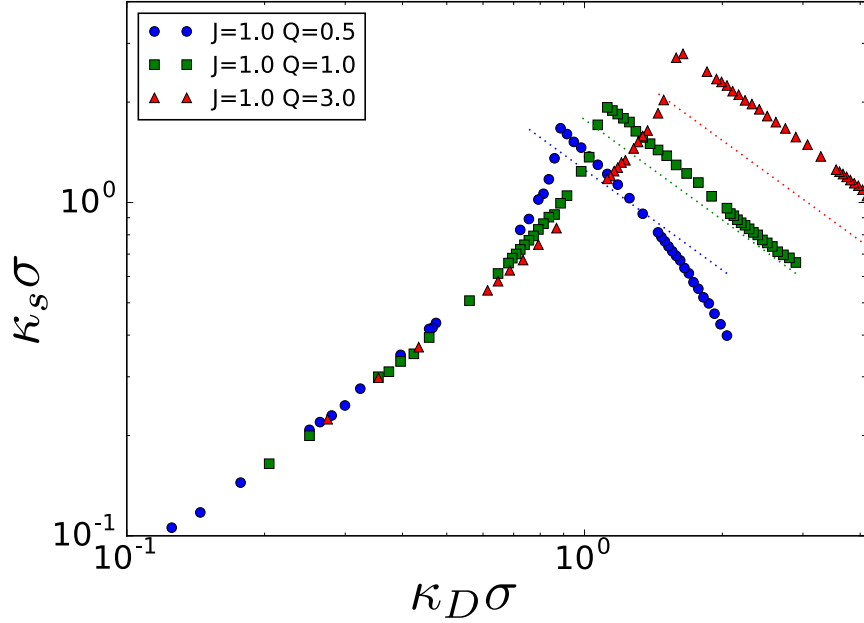


Figure 3.6: The screening constant, $\kappa_s\sigma$, against $\kappa_D\sigma$ for different $\rho Q/J$ ratios. We extract $\kappa_s\sigma$ here using the small- k coarse of $\tilde{G}_q(k)$ discussed in the Simulation section. Increasing $\rho Q/J$ shifts $\kappa_D^*\sigma$ to the right, also increasing the maximum screening constant, $\kappa_s^*\sigma$. Near but slightly above the regime change, simulation $\kappa_s\sigma \sim (\kappa_D\sigma)^{-1}$ for each $\rho Q/J$ (the dotted lines show the scaling $\sqrt{T/J} \sim (\kappa_D\sigma)^{-1}$ for each parameter set).

correlation length analogous to the mean field prediction in Eq. 3.5, 3.8. The scaling of $\kappa_s\sigma$ in the two regimes remains unchanged — $\kappa_s\sigma \sim \kappa_D\sigma$ when $\kappa_D \ll \kappa_D^*$ and $\kappa_s\sigma \sim (\kappa_D\sigma)^{-1}$ just after the regime changeover —despite changing the ratio $\rho Q/J$. Thus, the two distinct regimes are robust even beyond the validity of the continuum mean field theory; within the range of parameters studied here, increasing $\rho Q/J$ monotonically increases $\kappa_D^*\sigma$. The division between the DH and overscreened regimes can thus be controlled by tuning J , as predicted in Eq. 3.7 and borne out in simulations in Fig. 3.6.

Finally, we consider the limiting case that exists when varying $\rho Q/J$, namely when $J \rightarrow 0$. That limit allows us to make some connection with previous work on the lattice RPM [78, 79] whose short-range interaction is purely repulsive. We find that two regimes occur in simulation for $J = 0$, just as in the $J > 0$ case, see Fig. 3.7. Note that the simple FI

continuum mean field theory fails in this regime, predicting that the $J = 0$ case is identical to the Debye-Hückel theory for all values of $\kappa_D\sigma$. The simulation lattice plays a role directly analogous to the RPM hard sphere interaction, providing a sense of finite size to each ion.

3.4 Conclusions

The recent experimental discovery of universal scaling of the screening length, $\kappa_s\sigma \sim (\kappa_D\sigma)^{-2}$, in concentrated electrolytes and ionic liquids has rekindled theoretical interest in the large κ_D or strong Coulomb coupling regime [1]. Past theoretical work based on the RPM of electrolytes using closure relations such as hypernetted chain approximations [35, 53] and a generalization of the Debye charging process [55], as well as a molecular dynamics simulation study of molten NaCl salt [59], suggest $\kappa_s\sigma \sim (\kappa_D\sigma)^{-1/2}$ for κ_D just above the peak κ_D^* . Considering additional effects such as the formation of Bjerrum ions pairs may modify the scaling to $\kappa_s\sigma \sim (\kappa_D\sigma)^{-1}$ within a Poisson-Boltzmann framework [80].

In this work, we focus on the properties of the FI model well above its critical point, and find that it captures important features required to model the correlations of bulk ionic fluids. From simulations of the FI model, we find that $\kappa_s\sigma \sim (\kappa_D\sigma)^{-1}$ in the strong Coulomb coupling regime. The introduction of short length scale fluctuations affects only the temperature at which the crossover from the DH to the oscillatory regime occurs and leaves the scaling behavior unchanged. This scaling is different from the universal scaling experimentally observed in Ref. [1]. However, it may be possible to alter the scaling of the FI model in the overscreened regime via simple modifications such as the introduction of defects in the lattice [66], or creating asymmetry in the charge carriers, either in magnitude or shape [81]. These possibilities will be explored in future work. We also note that while the experimental universal scaling [1] and much previous theoretical work [35, 82, 53] place an emphasis on the ion size as a determining factor for the strong coupling regime, the ion size is not as simple to interpret in the FI model and appears to some extent through the

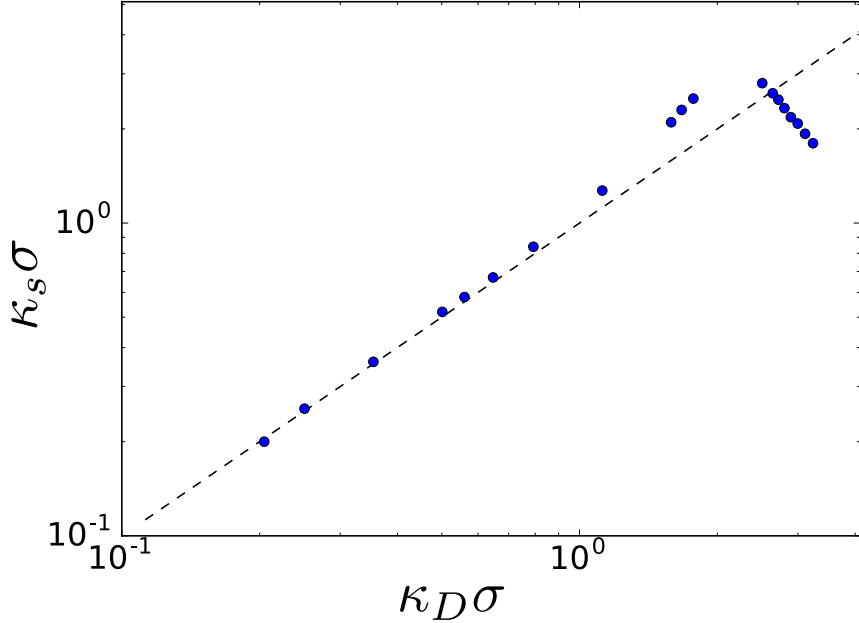


Figure 3.7: Screening constant, $\kappa_s\sigma$, displays non-monotonic trend as $\kappa_D\sigma$ (Eq. 3.5) is increased, shown here for $\rho Q = 1/a^2$ and $J = 0$. Dashed black line is the Debye constant, $\kappa_D\sigma$, which is also the prediction of the continuum mean field theory presented in the Model section when $J = 0$. Blue dots are screening constants extracted from the envelope of simulation charge-charge correlation functions, $G_q(r)$. Note that the domain and range of this plot differ from previous $\kappa_s\sigma$ vs $\kappa_D\sigma$ plots in this paper.

Ising coupling J .

In conclusion, the FI model complements other theoretical techniques commonly used to describe ionic fluids, such as mean-field Poisson-Boltzmann theories [29], integral equations [35], field theories [83] or their hybrids [84], and molecular simulations [59], and has the merit of reproducing the essential features of ionic correlations relatively simply. The FI model may be generalized to model surfaces and solvents in ionic fluids — which are systems of great current experimental interest [1, 25]. Overall, the Coulomb-frustrated Ising model is an attractive framework for the study of long-range non-DH correlations in ionic fluids due to its simplicity and its capture of broad qualitative trends.

3.5 Appendix: Simulation Methods

The Coulomb interaction is implemented using the Ewald summation technique [85, 86]. The long-range part is precomputed at the start of a run, since the separation between all lattice sites is fixed [75]. We use periodic boundary conditions in all three dimensions. Our simulation box has sides of length $L = 32a$ with $a = 1$ the lattice cell length. The lattice is initialized with an equal number of positive and negative charges. We use cluster moves which preserve the net charge of the system ($\sum_j^N q_j = 0$) and greatly reduce the autocorrelation times at low temperatures, improving efficiency [76]. Monte Carlo move random numbers are generated using the PCG pseudo-random number generator [87]. Lattice trajectories were visualized using VMD [88].

We use fundamental requirements for statistical mechanical electrostatic systems as a check for our simulations. The Stillinger-Lovett second moment (SL2) condition constrains the long-length scale fluctuations of a Coulomb system [77]. A formulation of the SL2 condition is that the charge structure factor (or equivalently, the Fourier charge correlation function) tends to zero as k^2 for small k [35]. We have demonstrated that our simulation produces the required trend, see in particular Fig. 3.2b. In addition, the high- T energy scaling of a Coulomb system must reduce to that of the Debye-Hückel theory: $U \sim -T^{-1/2}$ [33]. We confirm that condition as well.

Cluster moves are implemented as described in Ref. [76]. Briefly, two random sites and an axis of rotation are selected. One of the sites is the initial site of a cluster. The other random site is the center of a rotation of π about the rotation axis; the initial site of the second cluster is the result of the rotation of the first initial cluster site by π about this axis. If the two initial cluster sites are oppositely charged, the clusters are grown; otherwise the move is rejected. Each cluster is composed entirely of one type of spin. The two clusters are grown according to the rotational symmetry (ie. the rotation of π about the selected axis) as follows. The nearest neighbors of the first cluster are each proposed to be added in turn. To add a site,

it must have the same spin as it's cluster and it's symmetry pair (ie. rotated counterpart adjacent to the other cluster) must also have the same spin as it's cluster. When this occurs, they are both added to their respective clusters with probability $1 - \exp(-4\beta_{eff}J)$, where β_{eff} is a parameter tuned to maximize the cluster move acceptance ratio (here set to $1/5$ as suggested by Grousson and Viot [76]). The nearest neighbors of these newly added sites are added to the set of spins that must be checked for possible inclusion in the clusters. Only one attempt is made to add a given spin. Once no more spins can be added to the clusters, the move is accepted with probability $\exp(-\beta\Delta E_{Coul} + (\beta_{eff} - \beta)\Delta E_{Ising})$, where ΔE_{Coul} is the contribution from the Coulomb interaction to the change in energy of the proposed move and ΔE_{Ising} is the Ising contribution.

3.6 Appendix: Detailed Derivation of Mean Field Theory from a Lattice

In this section, we walk through the derivation of the continuum theory we use here (and in future chapters) from a variational mean field theory of a lattice. First, we consider a mean field theory for a pairwise \pm spin model with the goal of specializing to the Coulomb-frustrated Ising (or FI) model. We show that the mean field theory for the FI model maps essentially directly onto the Landau-Ginzburg ϕ^2 theory with Coulomb interaction. Finally, we extract the response function from the LG free energy, and compare it to a response function found previously showing that the LG Fourier charge correlation function can be considered a small- k expansion of the more complicated charge correlation function, and make the mapping concrete.

The work shown here is important because it establishes that the Coulomb-frustrated Ising model in the mean field approximation contains the same small- k information as other theories of dense ionic fluids.

This derivation draws from the texts by Safran [38] and Pathria [89].

3.6.1 Variational mean field theory for pairwise \pm spin model

Consider a pairwise \pm spin lattice model, ie. one with a Hamiltonian

$$H = - \sum_{ij} s_i H_{ij} s_j, \quad (3.13)$$

with $s_i = \pm 1$. As an example, if H_{ij} has only nearest neighbor (NN) interactions, such a Hamiltonian would represent the Ising model. We can make a variational approximation to a pairwise \pm spin model using a mean field, trial Hamiltonian

$$H_0 = - \sum_i s_i h_i \quad (3.14)$$

with h_i the mean field felt by spin s_i . Using the variational theorem, we can upper bound an uncorrelated estimate for the free energy of the full Hamiltonian,

$$F_{uc} \sim \langle H(\Gamma) + T \log p(\Gamma) \rangle_\Gamma, \quad (3.15)$$

by

$$F_{uc}^{(0)} \sim \langle H(\Gamma_0) + T \log p_0(\Gamma_0) \rangle_{\Gamma_0}. \quad (3.16)$$

Here, Γ is a vector-valued configuration variable (ie. it is equivalent to a specification of the set s_i of spins that make up a particular state), F is a free energy, T is the temperature-related energy (k_B set to 1 for convenience), $p \propto \exp(-H(\Gamma)/T)$, and $\langle f(\Gamma) \rangle_\Gamma = \sum_\Gamma p(\Gamma) f(\Gamma)$. Then to find the desired upper bound, $F_{uc}^{(0)}$, we must find the average energy and entropy with respect to p_0 .

First, consider the probability of observing a state $\{s_i\}$. Using the trial Hamiltonian

Eq. 3.14:

$$\begin{aligned} p_0 \{s_i\} &\propto \exp(-H_0/T) \\ &= \prod_i p_0(s_i), \end{aligned} \tag{3.17}$$

with $p_0(s_i) \equiv \exp(s_i h_i/T)$ the probability a single spin, i is in state s_i . Then using the trial Hamiltonian in which spins do not interact with each other, but instead with a mean field, leads to a set of independent spins.

Next, consider the partition function. Since the spins are independent, it follows that the partition function of the system, Z_0 , is a product of the individual spin partitions, z_i . Writing down the partition of a spin:

$$z_i = \sum_{s_i=\pm 1} \exp(s_i h_i/T), \tag{3.18}$$

which implies that

$$Z_0 = \prod_i (\exp(h_i/T) + \exp(-h_i/T)). \tag{3.19}$$

It will be convenient to work mostly with individual spin probabilities/partition functions.

Now, consider the average value of spin i , $\phi_i \equiv \langle s_i \rangle$:

$$\begin{aligned} \phi_i &= \sum_{s_i=\pm 1} s_i p(s_i) \\ &= \frac{\exp(h_i/T) - \exp(-h_i/T)}{\exp(h_i/T) + \exp(-h_i/T)}. \end{aligned} \tag{3.20}$$

Finally we are ready to compute the quantities we want to calculate: $\langle H \rangle_{p_0}$ and $\langle T \log p_0 \rangle_{p_0}$

:

$$\begin{aligned}
\langle H \rangle_{p_0} &= \sum_{s_i, s_j = \pm 1} p_0(s_i) p_0(s_j) \left(- \sum_{ij} s_i H_{ij} s_j \right) \\
&= - \sum_{ij} H_{ij} \sum_{s_i, s_j = \pm 1} p_0(s_i) s_i p_0(s_j) s_j \\
&= - \sum_{ij} \phi_i H_{ij} \phi_j,
\end{aligned} \tag{3.21}$$

and, noting that $1 + \phi_i = \frac{2}{z_i} \exp(h_i/T)$ and $1 - \phi_i = \frac{2}{z_i} \exp(-h_i/T)$,

$$\begin{aligned}
\langle T \log p_0 \rangle_{p_0} &= T \sum_{s_i = \pm 1} \sum_i p_0(s_i) \log p_0(s_i) \\
&= T \sum_i \frac{\exp(h_i/T)}{z_i} \log \left(\frac{\exp(h_i/T)}{z_i} \right) + \frac{\exp(-h_i/T)}{z_i} \log \left(\frac{\exp(-h_i/T)}{z_i} \right) \\
&= -NT \log 2 + \frac{T}{2} \sum_i (1 + \phi_i) \log(1 + \phi_i) + (1 - \phi_i) \log(1 - \phi_i).
\end{aligned} \tag{3.22}$$

We can simplify the sum over logs by expanding about $\phi_i \rightarrow 0$, which holds for $T > T_c$. In this limit,

$$\langle T \log p_0 \rangle_{p_0} \rightarrow -NT \log 2 + \frac{T}{2} \sum_i \phi_i^2 + O(\phi_i^4). \tag{3.23}$$

Combining,

$$\begin{aligned}
F_{uc}^{(0)} &= \langle H \rangle_{p_0} + \langle T \log p_0 \rangle_{p_0} \\
&= - \sum_{ij} \phi_i H_{ij} \phi_j + \frac{T}{2} \sum_i \phi_i^2 - NT \log 2.
\end{aligned} \tag{3.24}$$

3.6.2 Specializing to the Coulomb-frustrated Ising model

In the last section, we considered some general coupling between spins, H_{ij} in our full Hamiltonian. Now, we specialize to the Coulomb-frustrated Ising case, where

$$H_{ij} = \frac{1}{2} (J_{ij} - \rho Q V(r_{ij})) , \quad (3.25)$$

with

$$J_{ij} = \begin{cases} J & \text{if } i, j \text{ NNs} \\ 0 & \text{else,} \end{cases} \quad (3.26)$$

$V(r)$ the with electrostatic potential given by solution to the Poisson equation, and r_{ij} Euclidean distance between spins $i \neq j$. Here, we use the relaxed definition for the potential due to a point charge, giving the well-known Coulomb form $V(r) = 1/r$. Strictly speaking, the potential on a lattice of charges is not given by the Coulomb form [42], and our choice to use this approximate form leads to some unphysical effects, such as a critical temperature that can become negative for certain parameter settings (see discussion in the main text). We choose to use this approximate form because it allows us to make a connection with continuum field theories for the charge density, as we will see at the end of this derivation.

With the useful separation $\phi_i \phi_j = \frac{1}{2} [\phi_i^2 + \phi_j^2 - (\phi_i - \phi_j)^2]$, we can rewrite

$$\begin{aligned} F_{uc}^{(0)} &= \langle H \rangle_{p_0} + \langle T \log p_0 \rangle_{p_0} \\ &= - \sum_{ij} \phi_i \left(\frac{J_{ij}}{2} - \frac{\rho Q}{2} \frac{1}{r_{ij}} \right) \phi_j + \frac{T}{2} \sum_i \phi_i^2 - NT \log 2 \\ &= \frac{\rho Q}{2} \sum_{ij} \frac{\phi_i \phi_j}{r_{ij}} + \frac{1}{4} \sum_{ij} J_{ij} (\phi_i - \phi_j)^2 - \frac{1}{4} \sum_{ij} J_{ij} (\phi_i^2 + \phi_j^2) + \frac{T}{2} \sum_i \phi_i^2 - NT \log 2. \end{aligned} \quad (3.27)$$

We will now simplify term-by-term. Consider the third term. Since the summation runs

over i and j , $\phi_i = \phi_j$: the index variable is unimportant. Further, considering a particular i , we can write $\sum_j J_{ij} = 2dJ$ because there are $2d$ nearest neighbors for each i , and J_{ij} is zero for non-nearest neighbors. So

$$\sum_{ij} J_{ij} (\phi_i^2 + \phi_j^2) = 4dJ \sum_i \phi_i^2. \quad (3.28)$$

Next, consider the second term. The squared difference is symmetric, and has similar form to a squared gradient. Due to the symmetry and summation over i and j , each gradient between i and j is considered twice; once again we can replace the sum over j of J_{ij} with $2dJ$. Finally, to convert to a square gradient from a squared difference, we need to preserve units, and so we need to multiply by a length scale squared. The relevant length scale is the lattice cell length, σ , since we are considering nearest neighbors. Then

$$\begin{aligned} \sum_{ij} J_{ij} (\phi_i - \phi_j)^2 &= \sum_i (2dJ) [2\sigma^2 (\nabla \phi_i)^2] \\ &= 4\sigma^2 dJ \sum_i (\nabla \phi_i)^2. \end{aligned} \quad (3.29)$$

As in the case of the Poisson potential, it is possible to treat this “square-gradient”-like term in a manner that is closer to the underlying lattice nature of the problem. Again, we make our choice here so that we can make a connection with continuum field theories.

Making substitutions and regrouping, we find that

$$F_{uc}^{(0)} = \sum_i \left[\left(\frac{T}{2} - dJ \right) \phi_i^2 + \sigma^2 dJ (\nabla \phi_i)^2 \right] + \frac{\rho Q}{2} \sum_{ij} \left[\frac{\phi_i \phi_j}{r_{ij}} \right] - NT \log 2. \quad (3.30)$$

If $Q = 0$, ie. in the limit of an Ising model, our mean-field prediction for the critical temperature is $T_c = 2dJ$. For $d = 2$, the mean-field prediction of $T_c^{2D.MF} \sim 4$ is almost twice the actual value of $T_c^{2D} \sim 2.3$ [90], but for $d = 3$, the mean-field prediction of $T_c^{3D.MF} \sim 6$ is relatively closer to the numerical value of $T_c^{3D} \sim 4.5$ [91]. Mean-field theory is known

to become more exact as the dimensionality increases, and so it is comforting that our mean-field model has the expected trend.

The form of the free energy is very similar to a Landau-Ginzburg form, with a ϕ^2 term, and a square-gradient term. We can make this analogy explicit by defining a mapping. For a Landau-Ginzburg free energy of the form

$$F[\phi] = \frac{\sigma^3}{2} \int d^3r a [\phi(\mathbf{r})]^2 + m [\nabla\phi(\mathbf{r})]^2 + \frac{\sigma^3}{2} \rho Q \int d^3r \int d^3r' \phi(\mathbf{r}) V(|\mathbf{r} - \mathbf{r}'|) \phi(\mathbf{r}'). \quad (3.31)$$

where $V(r)$ is the electrostatic potential given by solution of the Poisson equation (for point charges, $V(r) = 1/r$) and we map from the mean-field Coulomb-frustrated Ising model as follows:

$$\begin{aligned} a &\leftrightarrow T - 2dJ = T - T_c^{MF} \\ m &\leftrightarrow c^2 2dJ = c^2 T_c^{MF} \\ Q &\leftrightarrow Q. \end{aligned} \quad (3.32)$$

In Fourier space, the free energy of the Landau-Ginzburg model is

$$F[\phi] = \frac{\sigma^3}{2} \int d^3k \left| \tilde{\phi}(k) \right|^2 \left[a + mk^2 + \rho Q \tilde{V}(k) \right], \quad (3.33)$$

with corresponding response function

$$\tilde{\chi}(k) = \frac{1}{m\sigma^3} \frac{k^2}{k^4 + a/mk^2 + 4\pi\rho Q/m}. \quad (3.34)$$

This derivation shows that the mean field theory of a lattice model, and specifically the charge-frustrated Ising model, can be mapped to a Landau-Ginzburg-like continuum field theory in the charge density. In fact, the continuum form is of the same form as a k^4 expansion of the theory of Adar et al. [57] discussed in Section 2.6. We make use of this

continuum form in the main text of this chapter. We also use the intuition developed from this model throughout the next two chapters. Thus, the mean field theory of the charge-frustrated Ising model presented here serves as a minimal model that we use as a foundation which we can relate our other results to. As we will see in Chapters 4 and 5, the mean field theory is surprisingly effective. However, we also show that it fails to explain some features of our colleagues' experiments, and our simulations are able to extend the range of our explanatory capability.

CHAPTER 4

STABLE COLLOIDS IN MOLTEN INORGANIC SALTS

The following chapter reproduces material previously published in Ref. [25]. That work was in collaboration with Hao Zhang, Kinjal Dasbiswas, Gang Han, Byeongdu Lee, Suriyanarayanan Vaikuntanathan, and Dmitri V. Talapin. I was the third author of the paper, and contributed to the simulation and theory portions of the work. Readers are referred to the original publication for more of the experimental details, which are only summarized here.

In the past chapter, we developed the charge-frustrated Ising model, and showed using mean field theory and simulations that two regimes emerge. At high temperature, or low $\kappa_D\sigma$, the theory and simulations reduce to the DH theory, as expected. However, when $\kappa_D\sigma \gtrsim 1$, a regime change occurs and correlations between ions become oscillatory. In addition, the length scale of the decay now increases with $\kappa_D\sigma$. The mean field theory was shown to agree with simulation for a specific range of parameters, but also with other theories [35, 52, 55, 56, 57], some qualitatively and some nearly quantitatively. However, one feature we did not address was the inclusion of solutes within ionic fluids. Though the linear response theory developed in Chapter 2 leads us to believe that charge-charge correlations should be intrinsically tied to solute-liquid correlations, we need to put this belief to the test within the context of high ionic strength fluids, which we do within this chapter in the context of nanocrystal colloids within molten salts.

4.1 Experimental Summary

In this work, we report the observation of colloidal systems of solute particles dispersed in molten inorganic salts. Various solutes – nanocrystals (NCs) of metals, semiconductors, rare earth, and magnetic materials – were synthesized by my experimentalist colleagues using organic surfactants (e.g., n-alkyl carboxylic acids) that stabilize colloidal solutions in non-

polar solvents. These organic surfactants are not compatible with molten inorganic salts, but they can be exchanged with inorganic surface ligands [92], which is expected to reduce the free energy of the interface between the NC surface and inorganic solvent. Moreover, surfactant-free (or “bare”) colloidal NCs can be prepared using ligand-stripping agents [93]. These recent developments in NC surface chemistry have been utilized to integrate NCs in inorganic hosts by co-precipitation from suitable solvents [94, 95].

It appears that traditional stabilization mechanisms cannot explain the colloidal stability of NCs in a molten inorganic salt. The refractive index of NCs is generally higher than that of the molten salt (e.g., $n \sim 2.5$ for CdSe vs $n \sim 1.4$ for molten KCl) and van der Waals attraction cannot be eliminated because of index matching. A very high charge density in a molten salt is expected to result in strong electrostatic screening, making Coulomb repulsive forces short-ranged and weak compared to van der Waals attraction [96]. The absence of brush-like molecules tethered to the NC surface also rules out the possibility of classical steric colloidal stabilization [29].

To understand the origin of colloidal stabilization in molten inorganic salts, we carried out a series of experimental and computational studies. My experimentalist colleagues found that only certain NC-MS combinations were colloidally stable. In particular, they found that systems were stable when there was strong binding between the molten salt and nanocrystal surface. This led us to postulate that, due to the high concentration of ions, ion layers might be formed at the surface of the nanocrystals, as shown in the cartoon in Fig. 4.1a.

4.2 Summary of Simulation and Theory

To test our hypothesis regarding the origin of colloidal stability, we modelled the interface between the CdSe crystal and molten KCl using molecular dynamics (MD) simulations (Fig. 4.1b and Section 4.4). Solvent structuring takes place near every solid-liquid interface, regardless of the interaction between the surface and solvent [29]; it typically creates de-

caying solvent density oscillations that propagate for several molecular diameters [97]. Ion layering near interfaces has been reported in molten salts and organic ILs [98], and it was also observed in our simulations. Near the interface with a chemically inert hard wall, both K^+ and Cl^- ions showed identical oscillatory density profiles that decayed to the bulk density within less than 0.5 nm (Fig. 4.1c, top panel). In contrast, cadmium-terminated [001] and [111] CdSe surface, which are the typical facets of zinc-blende CdSe NCs [99], induced a qualitatively different behavior in the molten salt. In agreement with previous experimental data [100], CdSe NCs showed a strong affinity toward Cl^- ions that formed a dense, nearly epitaxial surface layer (see Section 4.4). These co-ions templated strong ordering in the molten salt, with alternating K^+ and Cl^- shells extended into the liquid phase for about 2 nm (Fig. 4.1b and bottom panel in Fig. 4.1c). The ion shells created charge density oscillations around each NC, which were robust with respect to temperature above T_m .

When two NCs approach each other to a distance smaller than twice the length of the structured ion layers, the interference between charge density oscillations contributes to attraction or repulsion of NC cores. To evaluate the free energy of this interaction, we carried out umbrella sampling simulations (see Section 4.4). For two parallel surfaces, the surface-templated charge density oscillations can interfere constructively or destructively, depending on the distance, which leads to an exponentially decaying oscillatory interaction energy (Fig. 4.1d). However, any tilt between two surfaces causes suppression of the oscillatory component and development of a repulsive force between approaching surfaces due to frustration of the molten salt layers (Fig. 4.1e). Using a linear combination of differently tilted surfaces, the interaction energy between two 10 nm spheroid NCs can be modeled (Fig. 4.1f and Section 4.4). This repulsive-oscillatory force of ion structuring by far exceeds the van der Waals and double layer electrostatic contributions at all interparticle separations, except at very short sub-nm distances (Fig. 4.1f), and is responsible for the colloidal stability.

To rationalize MD simulations, we applied a phenomenological Landau-Ginzburg theory

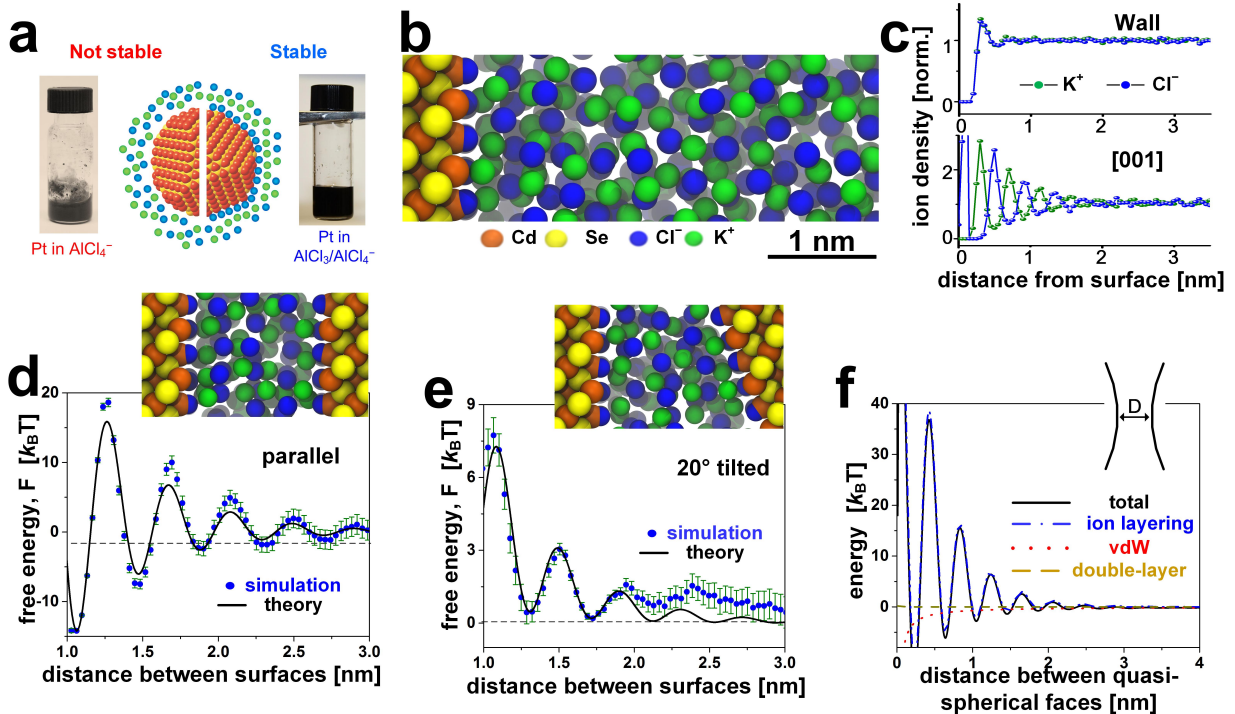


Figure 4.1: The origin of colloidal stability in molten salts. **(a)** The relationship between chemical affinity of the NC surface to species in molten salt (represented by blue and green spheres), and colloidal stability. Corresponding examples of stable and unstable colloidal dispersions are shown in the photographs. **(b)** A snapshot of MD simulation of the interface between the Cd-terminated [001] surface of zinc-blende CdSe crystal and molten KCl. **(c)** Density profiles of K^+ and Cl^- ions showing the structuring of molten salt near the interface with a chemically inert wall (top) and with Cd-terminated [001] (bottom) surface of zinc-blende CdSe crystal. The crystal surface templates strong ordering of the molten salt. **(d,e)** Simulated free energy of ion structuring in molten KCl (blue dots) between two [001] CdSe surfaces (d) parallel to each other and (e) tilted by 20° . Black lines are the predictions from continuum Landau-Ginzburg theory. **(f)** Simulation free energy of the interactions between two spheroid NCs (diameter 10 nm), including the total energy and the contributions from the ion layer structuring, the van der Waals (vdW), and the electrostatic double layer interactions, respectively. Details of the protocol to estimate the free energy of interacting spheroids is discussed in the text.

to solvation in molten salts. Using the Derjaguin approximation, the interaction energy of ion structuring between spherical particles can be derived as having two parts, one a damped oscillatory function and one a repulsive exponential decay (see Eq. 4.18). Our theory shows very good agreement with MD simulations, as seen in Fig. 4.1d,e, and further supports the important role of the ion structuring near curved surfaces for colloidal stabilization of NCs in molten salts. In the absence of surface-templated charge density oscillations, only attractive force between NCs was predicted by the theoretical analysis and also observed in simulations, in agreement with the experimental data. One can see the similarity of the oscillatory-repulsive forces between NCs in molten salts and the hydration repulsion between polar surfaces in water [101, 102], although the physical origin of these forces appears to be different.

We now describe the continuum theory we used to study the interaction between nanocrystal colloids within molten salts.

4.3 Continuum theory for interacting surfaces in molten salts

In this section, we develop a phenomenological theory similar to the ones developed in Sections 2.6 and 3.2 to explain the colloidal stability observed in suspensions of various nanocrystals in inorganic molten salts. We use this phenomenological theory to predict and rationalize the layering seen in simulations purely in terms of physical interactions ubiquitous in both inorganic molten salts and organic room-temperature ionic liquids: short-range steric (present in all liquids [34]) and long-range electrostatic (Coulomb) interactions between ions. Such a phenomenological theory has been used successfully to describe experimentally observed capacitive transitions at electrode-room temperature ionic liquid interfaces [61, 65].

In the traditional DLVO theory of interactions between colloidal particles, as discussed in Section 2.3, double layer or electrostatic forces lead to a repulsion between charged surfaces in a solution [103]. Due to the high density of ions in a molten salt, the electrostatic forces

between charged surfaces are expected to be screened out over very short distances [65]. The colloidal particles are therefore predicted by the DLVO theory to aggregate because of attractive van der Waals or solute-mediated interactions.

Here we show that colloidal stabilization in molten salts can be explained by interactions not accounted within DLVO theory. We consider a different scenario here that surface-induced ordering or layering in the molten salt [104, 105] contributes to the colloidal stability, as observed both in experiments and simulations. Such layering is expected to be pronounced and extend a long distance into the bulk if the salt is reasonably close to its crystallization temperature. In the following, we present our calculation for the free energy of interaction between two planar, infinite surfaces in an inorganic molten salt from a continuum Landau-Ginzburg theory perspective, taking into account both the short-range steric and long-range electrostatic interactions [106]. We first derive the oscillatory interaction energy between a pair of symmetric, parallel surfaces. We then show that a relative tilt between the two surfaces can lead to a repulsive free energy profile superimposed on the oscillatory profile. Such a tilt is important to account for faceting, curvature, and also surface roughness on real nanocrystal (NC) surfaces. The effects of curvature, faceting and roughness are expected to frustrate the layering and attenuate the oscillations in free energy. But it still maintains large repulsive barriers between two approaching NCs, as shown in our simulations. Finally, the force between two plane surfaces can be generalized to that between two finite, spherical colloidal particles by using the Derjaguin approximation, previously discussed in Section 2.3. This theory is general for investigating the interactions between particles in a solvent composed solely of ions, including colloidal NCs in inorganic molten salts. As an example, we choose CdSe NCs in molten KCl and analyze their interactions using this theory.

4.3.1 Approximate continuum Hamiltonian for charge density ordering

The layering of ions normal to a flat nanocrystal (NC) surface (with normal along the z -axis) can be described using a Landau-Ginzburg model for the free energy above the critical temperature. The bulk free energy of the system including the effect of long range interactions in the solvent is [22], from considerations in Section 2.6 and Chapter 3,

$$\begin{aligned} F[\phi(z)] &= \frac{\sigma^3}{2A} \int dz a [\phi(z)]^2 + m [\nabla \phi(z)]^2 + \frac{\sigma^3}{2A} \rho Q \int dz \int dz' \phi(z) V(|z - z'|) \phi(z') \\ &= \frac{1}{2A} \int dk |\tilde{\phi}(k)|^2 m \sigma^3 \left[k^2 + a/m + \left(\frac{(\kappa^*)^2}{k} \right)^2 \right], \end{aligned} \quad (4.1)$$

where σ is a coarse-graining length, a is dependent on temperature, m governs the elasticity which comes from particle interactions, ρ is the density of ions in the fluid, Q describes the electrostatic interaction strength, and

$$\kappa^* \equiv \left(\frac{4\pi\rho Q}{m} \right)^{1/4}, \quad (4.2)$$

is the fluids preferred wavenumber for which the free energy is minimized and also the inverse of the shortest length scale the system can support (also the decay length scale at the change between DH-like and oscillatory regimes) – see discussion in the context of the FI model in Section 3.2. The response function is written

$$\tilde{\chi}(k) = \frac{1}{m\sigma} \frac{k^2}{k^4 + a/mk^2 + (\kappa^*)^4}. \quad (4.3)$$

In Eq. 4.1, $\phi(z)$ is the local charge density of the solvent expressed as the difference in number density of cations and anions normalized by the total number density of salt. The free energy $F[\phi(z)]$ in Eq. 4.1 is the effective one-dimensional Hamiltonian for describing the

molten salt. We ignore the $(\phi(z))^4$ and higher order terms because the molten salt (KCl) is above its bulk melting temperature and is a disordered liquid far from the colloidal interface. The effect of long-range interactions is simplified in Fourier space, as shown in the second line in Eq. 4.1. Following a similar procedure as in the derivation of the DLVO interaction energy in Section 2.3, the free energy of the fluid between the plates is related to the amount which the confinement interrupts the screening of each plate's surface charge [45, 46]:

$$F_p(D) \xrightarrow{D \gg 1/\kappa} m \frac{\sigma^3}{2A} \int_{D/2}^{\infty} dz \frac{a}{m} [\phi(z)]^2 + [\nabla \phi(z)]^2 + \frac{\rho Q}{m} \int_{D/2}^{\infty} \int_{D/2}^{\infty} dz dz' \phi(z) V(|z - z'|) \phi(z'), \quad (4.4)$$

with κ the decay length of the correlations, to be defined momentarily (in the DH regime, $\kappa \rightarrow \kappa_D$).

The wavelength of ordering can be a few angstroms which is about one ionic layer thick as expected. The solvent can thus exhibit layering up to a long length scale as a result of the competition between steric and Coulomb interactions. Indeed, estimates of the screening length obtained by analyzing the poles of the structure factor are much larger than the Debye length (even in the Gaussian approximation used here).

Such an effective Hamiltonian has been used to describe a variety of materials whose ordering is governed by a competition between short- and long-range interactions [18] – for example, magnetic films, diblock copolymers, Langmuir monolayers, and more recently, ionic liquids [61, 65, 107] – and the corresponding phase diagram has been extensively studied and characterized [106, 20]. This is richer than that for a simple liquid: as the temperature is lowered towards the bulk ordering temperature, the liquid can go from being disordered to an intermediate regime characterized by local structural order before long-range crystalline order is established. In Eq. 4.1, we consider the molten salt to be above its ordering temperature, so that while the bulk is disordered, a nanocrystal surface can template local order in its

vicinity [18, 98].

The linear response of the fluid in the bulk results in a fourth-order linear differential equation that can be solved analytically (especially easily in Fourier space), or which follows from linear response Eq. 2.20,

$$\tilde{h} = \tilde{\chi}^{-1} \tilde{\phi}. \quad (4.5)$$

With the appropriate surface boundary condition (determined by the chemical interaction of the surface with ions) and charge neutrality conditions, one can solve the charge density profile, $\phi(z)$. A solution for $\phi(z)$ induced by one surface that satisfies a simple boundary condition that puts a energetic potential on the fluid at $z = 0$, and global charge neutrality, is given by Eq. 9.15, and reproduced here:

$$\phi(z) = \phi_0 \exp(-\kappa z) \sin\left(\omega z + \frac{\theta}{2}\right), \quad (4.6)$$

where $\theta = -\arctan\left(\sqrt{(\kappa_D l_c/2)^2 - 1}\right)$ is the phase, which ensures charge neutrality in the bulk of the solvent and

$$\phi_0 \equiv -\frac{A}{4l_c^2 \kappa^* \sqrt{1 - (2l_c \kappa_D)^{-2}}}, \quad (4.7)$$

with $A = \beta\epsilon$ as in the DLVO case in Section 2.3. This form of the charge density arises since the NC (e.g., Cd-terminated CdSe NCs) surface has a strong preference for one type of ions (i.e. Cl^-) in the melt, which in turn leads to successive alternating layers of cations and anions (with wavenumber ω) decaying with distance from the surface (with a range of κ).

4.3.2 Charge density order and free energy in two-surface geometry

Having solved the charge density ordering near one surface, we now solve for the corresponding order between two surfaces. This can be used to calculate a free energy profile for the interaction between two NC surfaces as a function of their distance of separation. Colloidal

stability may result from large barriers (compared to $k_B T$) in this free energy landscape.

Parallel surfaces

The linear response equation, Eq. 4.5, corresponds to the Hamiltonian that describes the competition between short- and long-range interactions (Eq. 4.1). It is analytically solvable and can be generalized easily to the case where there are two symmetric surfaces in parallel (located at $z = 0$ and $z = D$) that induce order. The solution can be approximated as the superposition of two one-plate solutions, similar to the DLVO case in Eq. 2.29, leading to

$$\phi_2(z) = \phi(z) + \phi(-z + D). \quad (4.8)$$

In the limit of large separation, $D \gg 1/\kappa$, the profile up to the midplane can be approximated as the single plate profile,

$$\phi_2(z) \xrightarrow{D \gg 1/\kappa} \phi(z), \quad z < D/2. \quad (4.9)$$

As in the DLVO discussion in Section 2.3, the free energy due to the confinement of the fluid between two charged plates is related to the surface charge of each plate which remains unscreened [45, 46], or equivalently, the integral of the one-plate charge density beyond the midplane, Eq. 4.4. We use this simple expression to calculate the fluid-plate electrostatic free energy by inserting the expression in Eq. 4.8 into Eq. 4.4, finding

$$F_p(D) \sim \frac{a\phi_0^2\sigma}{\kappa} (\kappa^*)^2 \frac{m}{a} \exp(-\kappa D) \sin(\omega D), \quad (4.10)$$

and for convenience later, defining

$$F_0 \equiv \frac{a\phi_0^2\sigma}{\kappa} (\kappa^*)^2 \frac{m}{a}. \quad (4.11)$$

Tilted surfaces

Our simulations show that there is an exponentially decaying repulsive component over and above the oscillatory features in the free energy, particularly apparent in the 20° tilted plates (Fig. 4.1e and 4.5b). This is related to the large energy cost of removing the last few remaining ionic layers as the two NC surfaces approach very close to each other [29]. Here, we present a qualitative way of understanding this repulsion in terms of the phenomenological theory.

An obvious effect of tilting one surface with respect to the other is that the separation between the two plates is different at different positions, leading to an averaging out of the oscillatory interactions to some extent. By integrating Eq. 4.10 over the range of separation $D_{max} - D_{min} = l_p \sin \theta_t$, where l_p is the linear size of the plate (corresponding to the size of the NC facet) and θ_t is the angle of tilt, one can obtain the factor by which the oscillations are attenuated. For large facet areas and/or large angles of tilt, the oscillations are averaged out to a large extent and an approximate form for the attenuation factor is $\eta \sim \omega l_p \sin \theta_t$, whereas for small plates tilted at small angles, i.e. in the limit $\kappa l_p \sin \theta_t \ll 1$, the attenuation factor scales as $\eta \sim 1 + \kappa l_p \sin \theta_t$. We indeed see an attenuation in the free energy oscillations in the simulation results for plates tilted at larger angles (Fig. 4.5b). However, for NCs of small size, such as used in this experiment, and strong surface-induced layering (i.e., high energy peaks), the attenuation is not strong enough to completely wash out these oscillatory features.

When one of the order-inducing surfaces is tilted with respect to the other, the order is induced along different axes (see simulation snapshot in Fig. 4.1e). This can be analyzed as an effective one-dimensional problem by considering variations of the charge density along the z -axis, assuming the two surfaces induce different effective layering wavenumbers, ω_l and ω_r , respectively, where $\omega_r = \omega_l \cos \theta_t$. The density profile can be approximately calculated

by superposing the one-surface solutions from the left and the right,

$$\phi_t = \phi_0 \left[\exp(-\kappa z) \sin \left(\omega_l z + \frac{\theta}{2} \right) + \exp(\kappa z) \sin \left(\omega_r (-z + D) + \frac{\theta}{2} \right) \right], \quad (4.12)$$

where the asymmetry between the surfaces leads to different preferred wavelength of order induced by left and right surfaces. We expect this Ansatz to be more accurate when the plate separation, D , is significantly larger than the decay length, $1/\kappa$. The tilt free energy can be computed numerically using the profile in Eq. 4.12 and the approximate free energy in Eq. 4.4, or can be represented with a scaling argument as we discuss now.

The relative tilt between the ordering from the right and left surfaces (see snapshot in Fig. 4.1e) is reminiscent of a grain boundary in a crystalline ordered phase. The creation of a grain boundary, which is a defect in the ordering, causes a free energy penalty. The energy cost increases with the tilt angle [37] as has been shown in the context of defects in lamellar ordering in block copolymers [108]. The two surfaces would therefore tend to move away from each other to reduce this free energy cost (which scales as square of the amplitude of order parameter), therefore resulting in an effective repulsion. We expect this repulsive free energy cost to scale as

$$F_t(D, \theta_t) \sim F_0 \frac{\kappa}{\kappa^*} \exp(-\kappa D) \theta_t^2. \quad (4.13)$$

To summarize, the interaction between two parallel flat surfaces is a decaying and oscillatory function of their distance of separation, D , being minimized at the special separations where commensurate layering can occur, i.e. an integer number of ionic layers can fit in between the two plates. On top of this, there are repulsive interactions between two tilted plates which is an effective function of the angle of tilt, θ_t . The total free energy of interaction between two mutually tilted flat surfaces, for a small angle of tilt, can then be captured

by the following semi-empirical expression where the effect of the tilt is taken into account

$$\begin{aligned} F(D, \theta_t) &= F_p(D) + F_t(D, \theta) \\ &\sim F_0 \exp(-\kappa D) \left[\sin(\omega D) + \frac{\kappa}{\kappa^*} \theta_t^2 \right]. \end{aligned} \quad (4.14)$$

Curved surfaces

Now, we use the interactions between parallel and tilted plates to approximate the interaction between spherical colloids using an adaptation of the Derjaguin approximation. The Derjaguin approximation, discussed in Section 2.3, is appropriate for the typical solvent structuring interactions between colloids. However, DLVO forces, dilute electrostatic or van der Waals, depend only on the distance of separation of the surfaces and their area. To apply the Derjaguin approximation to oscillatory and directed interactions, such as the colloid-induced layering observed in MD simulation, we have to modify this procedure to effectively account for the tilt. First, we compute the contribution to the free energy as if the layers templated by each point of the colloid surfaces were parallel, and then find the contribution due to the relative tilting of the surfaces at each point.

The parallel contribution is easily computed using the integral derived in Eq. 2.34 and the expression for parallel plate free energy Eq. 4.10 (scaled by the parallel plate area, A_{pl}):

$$\begin{aligned} F_{p.sphere}(D) &= \pi R \int_D^\infty dz F_p(z)/A_{pl} \\ &= \frac{\pi R F_0}{A_{pl} \sqrt{\kappa^2 + \omega^2}} \exp(-\kappa D) \sin(\omega D), \end{aligned} \quad (4.15)$$

where $\sqrt{\kappa^2 + \omega^2} = \kappa^*$ as seen in Appendix Eq. 9.27.

To compute the tilt contribution, we integrate over the same circular surface elements as in the standard Derjaguin approximation, and using the first line in the geometric relation

Eq. 2.33, we can write a relation between the separation and the tilt angle θ_t

$$z(\theta_t) \xrightarrow{\theta_t \rightarrow 0} D + R\theta_t^2, \quad (4.16)$$

for small angles. The total interaction energy is then found by performing the integral of F_t introduced in Eq. 4.13 (scaled by the parallel plate area, A_{pl}) over the surface elements described in Eq. 2.34,

$$\begin{aligned} F_{t,sphere}(D) &= \pi R \int_D^\infty dz F_t(z)/A_{pl} \\ &\sim \frac{\pi F_0}{A_{pl} \kappa \kappa^*} \exp(-\kappa D). \end{aligned} \quad (4.17)$$

The contribution to the free energy of interaction from the tilt scales with a lower power in R than the interaction between parallel surfaces. The physical meaning of this is apparent when we write the total effective energy of interaction between spherical surfaces by combining Eq. 4.15 and 4.17, leading to

$$F_{sphere}(D) \sim \frac{\pi RF_0}{A_{pl} \kappa^*} \exp(-\kappa D) \left[\sin(\omega D) + \frac{1}{\kappa R} \right]. \quad (4.18)$$

Eq. 4.18 shows that the oscillatory (and symmetric) interactions between parallel surfaces becomes more pronounced as R is increased, i.e. the surfaces approach the flat limit, while the repulsive component increases when R is small, as now the surface elements sample greater tilt angles. This R -dependence is as per our physical expectations and is illustrated in Fig. 4.1f and 4.6. We also compare the typical DLVO forces, discussed in Section 2.3 with the layering interactions for a typical spherical particle (4 nm diameter) used in experiment in Fig. 4.1f. The dependence of the colloidal interactions on the size of the colloidal nanoparticles suggested in Eq. 4.18 would be interesting to probe in subsequent experiments. Particularly, kinetic trapping by large oscillatory barriers may become increasingly relevant

for larger colloidal particles where the repulsive component becomes relatively smaller.

In the next section, we describe the molecular dynamics simulations we performed to study the interactions between nanocrystals in molten salts.

4.4 Molecular dynamics (MD) simulations of NCs in molten KCl

4.4.1 *Simulations of ion layering on a CdSe NC*

In addition to the analysis with continuum Landau-Ginzburg theory, we ran MD simulations of CdSe NCs in KCl solvent [109]. The details for MD simulations are included in the Appendix. Along the same lines as the theory discussed above, we start our MD simulations by considering ion layering around a single CdSe NC surface. Then we simulate the interactions between two parallel surfaces in molten salts, especially along the axis normal to NC surface. We generalize such interactions to two tilted surfaces and finally quasi-spherical NCs. For comparison, we also run simulations of structureless, or chemically inert, walls in molten KCl. There have been several reports on the influence of molecular layering on forces between colloids and nanoparticles using continuum theory and MD simulations in room temperature ionic liquids [110]. However, to the best of our knowledge, there has been no quantitative theoretical studies for the forces between colloids induced by an inorganic molten salt.

In general, solid surfaces are expected to induce liquid density oscillations [34, 97]. In densely charged liquids, solid surfaces with surface charge are known to induce even longer range charge density oscillations [65, 98]. As expected, we observed robust layering of the K^+ and Cl^- ions near the surfaces of the nanoparticles (normal to the NC surface: Fig. 4.2). In addition to ion layering in the direction normal to the interface, significant in-plane ordering of K^+ and Cl^- ions was observed near the crystal surface because of a good match between the in-plane periodicity of the CdSe surface and the diameters of ions in the molten salt. The

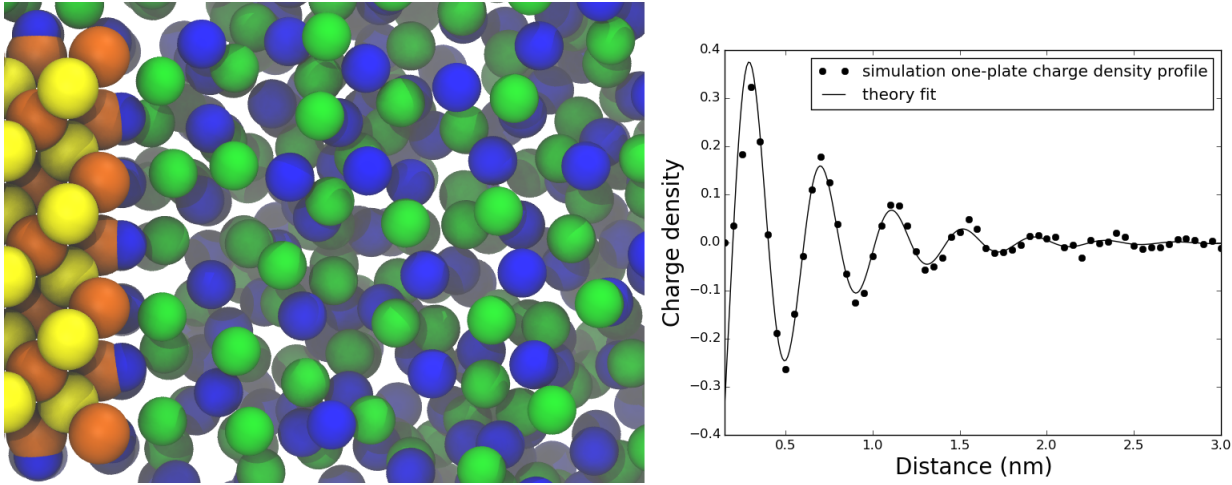


Figure 4.2: The chemical affinity between Cd-terminated [001] CdSe surface and Cl⁻ induces charge density oscillations in molten KCl. **(Left)** A snapshot of layering of ions between two [001] surfaces of CdSe nanocubes ($2.45 \times 1.85 \times 1.85 \text{ nm}^3$). **(Right)** Simulated charge density as a function of the distance between two surfaces; note the Cd-bound C peaks have been omitted from the charge density profile. Color code in the snapshot: Orange: Cd, yellow: Se, green: K⁺, and blue: Cl⁻. Here, the density profiles templated by the nanocubes constructively interfere, and so this configuration is at a free energy trough. Note that the bound layer of Cl⁻ ions are not shown in the charge density profile.

in-plane correlation functions describe the statistically averaged, in-plane distances between particles and their neighbors. As in-plane ordering increases, the peaks will become sharper and will decay less with distance. For example, a system with no in-plane ordering will display a constant value for all separations, while a solid will have sharp peaks that extend as far as desired without decay.

We quantified the net interaction between two rectangular cuboid zinc-blende CdSe NCs (hereon referred to as “nanocubes”) of dimension $2.45 \times 1.85 \times 1.85 \text{ nm}^3$ in solution along the axis normal to NC surface using standard enhanced sampling techniques (specifically umbrella sampling) [111, 112, 86]. In addition, we fit the charge density profile shown in Fig. 4.2 with the Landau-Ginzburg theory. In detail, we extracted the length scales, the correlation length ($1/\kappa$) and the oscillation frequency (ω) from the density profile in Fig. 4.2 by fitting the expression for the charge density with Eq. 4.6. Using κ and ω , we were able to find correspondence between simulation and theory using a two parameter fit of Eq. 4.14

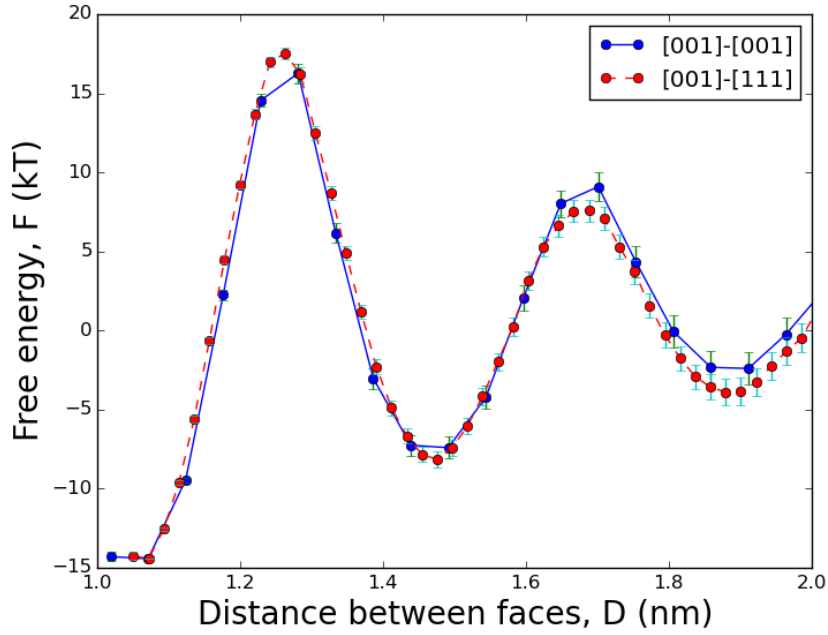


Figure 4.3: Simulated free energies of layering between two surfaces of CdSe nanocubes, [001]-[001] (blue) and [001]-[111] (red), in molten KCl. The indistinguishable free energies of interactions between different facets indicate the ion layering is the dominant factor.

for the amplitude, F_0 , and $f(\theta) \sim c\theta^2$, with c a fitting parameter.

We focused on interactions between Cd-terminated CdSe [001] facets, but also collected data for the interaction of a [001] Cd-terminated facet interacting with a [111] Cd-terminated facet; the nanocube interactions were indistinguishable (Fig. 4.3). We conclude that the main effect here is solvent layering along the surface normal, and that in-plane ordering effects due to surface atom arrangement is less important. For simplicity, we fixed the orientation of the nanocubes, and only allowed motion along one axis, which is normal to the NC surface.

Parallel nanocubes induced charge density oscillations in the KCl solvent which interfered at the midplane when the nanocubes came close together (Fig. 4.4). The interference leads to a decaying, oscillatory energy of interaction between nanocubes as a function of separation, D (Fig. 4.5A). If we envision two nanocubes coming together along a shared surface normal, there will be certain distances where the charge density templated by each cube align and

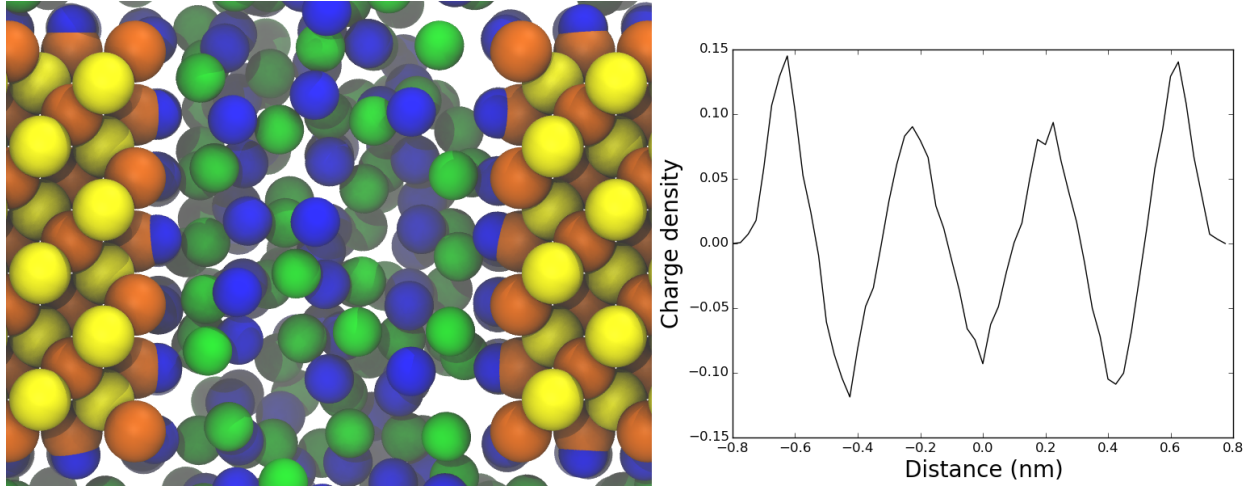


Figure 4.4: An example of parallel CdSe nanocubes in molten KCl and the corresponding charge density profile. (**Left**) A snapshot of layering of ions between two [001] surfaces of CdSe nanocubes ($2.45 \times 1.85 \times 1.85 \text{ nm}^3$). (**Right**) Simulated charge density as a function of the distance between two surfaces; note the Cd-bound Cl⁻ peaks have been omitted from the charge density profile. Color code in the snapshot: Orange: Cd, yellow: Se, green: K⁺, and blue: Cl⁻. Here, the density profiles templated by the nanocubes constructively interfere, and so this configuration is at a free energy trough. Note that the bound layer of Cl⁻ ions are not shown in the charge density profile.

reinforce (Figs. 4.5C,D). There will also be certain distances where the charge densities will be perfectly anti-aligned, leading to destructive interference of the charge density wave (Figs. 4.5E,F). Intuitively, destructive interference is energetically costly because planes of like charges interact without screening. As seen in Figs. 4.5E,F, the charge density at the midplane is near zero, indicating an equal mixture of charges, leading to a strong, repulsive interaction between the planes of like charge adjacent to the midplane. As will be discussed later, the high energy penalty for destructive interference leads to a unique phenomenology.

A decaying oscillatory interaction energy (Fig. 4.5A) will preclude nanocube flocculation since particles cannot assemble closer than a certain separation where the free energy maximum (peak) overpowers the thermal energy. However, such an energy profile also presents the possibility that nanocubes might become kinetically trapped (also known as reversible coagulation [29]) in local minima (e.g., point c in Fig. 4.5A). On the other hand, our simulations show that the colloidal stability can be increased by introducing slight tilting. In

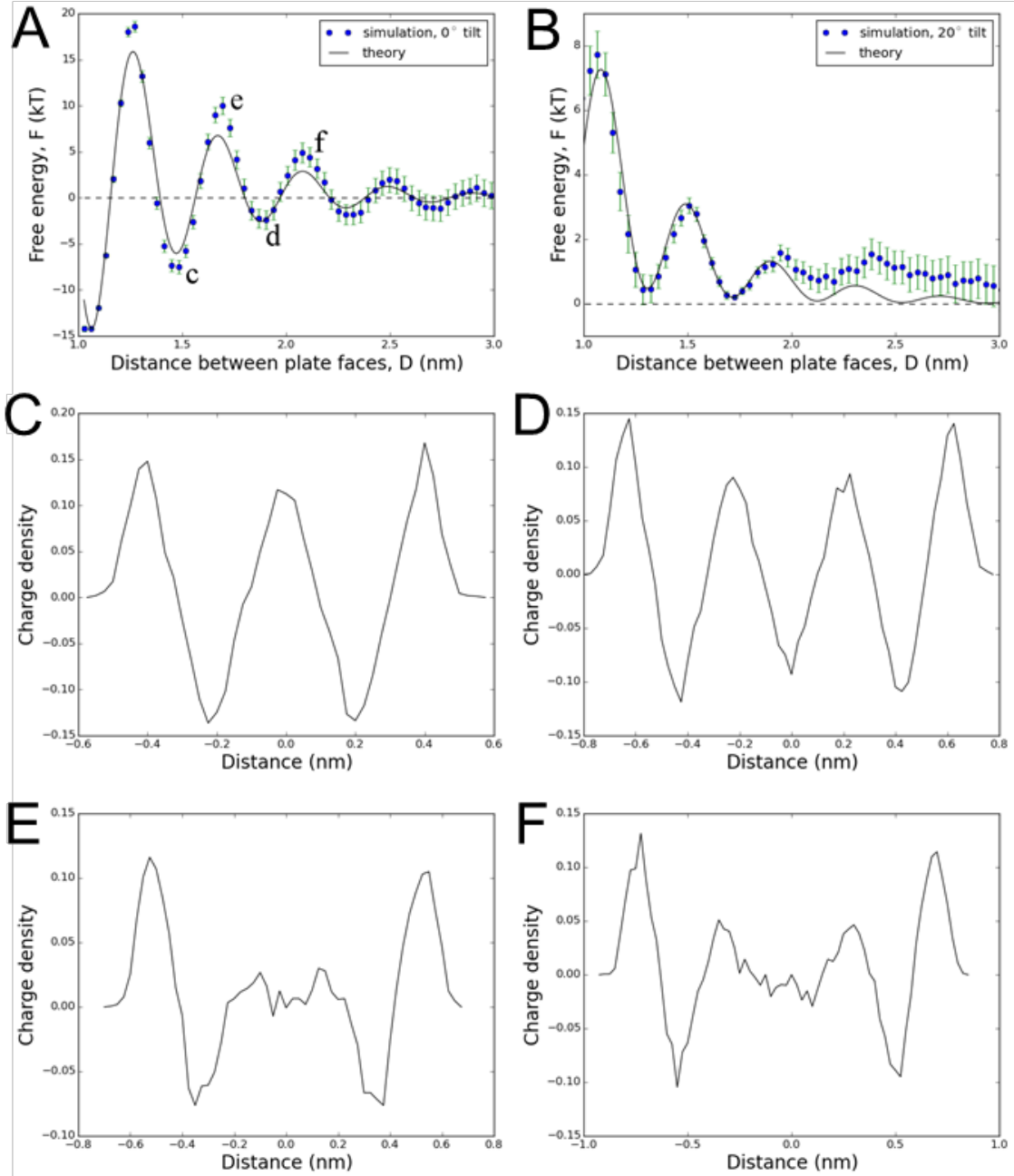


Figure 4.5: Simulated free energies of layering (blue dots with error range) for two parallel (**A**) and tilted (**B**) nanocubes ($2.45 \times 1.85 \times 1.85 \text{ nm}^3$), and fit (solid lines) by the Landau-Ginzburg theory with Coulomb interactions (Eq. 4.18). (**CF**) Simulated charge densities between two parallel nanocubes located at troughs (**C,D**) and peaks (**E,F**) as marked in (**A**); the Cd-bound Cl^- peaks have been omitted from the charge density profiles. Note that constructively interfering charge density profiles are low energy configurations and destructively interfering ones are high energy configurations.

detail, we introduced frustration into the system by varying the nanocube surface normals. A relative tilt between nanocubes washes out the peaks and troughs of the interaction energy to some extent. Two nanocubes with a relative tilt can be thought of as a linear combination of many parallel plates at slightly different separations, since the effect of tilt is to introduce a range of separations between the plates (see Fig. S2A). So the energy of interaction of two tilted plates is just the average of the energies of many parallel plates at slightly different separations. A larger relative tilt introduces a larger range of separations over which the average must be taken, decreasing the oscillatory character of the interaction compared to that of the parallel case. Thus, a purely repulsive interaction without much oscillatory character can be observed (Fig. 4.5B). Note there is a significant difference in energy scales shown in Figs. 4.5A,B due to the diminishing oscillatory contribution. Allowing rotations of the nanocubes in simulations would lead to additional repulsive free energy beneficial for colloidal stability. This and other possibilities will be explored in future work.

Real NCs typically have spheroidal shape truncated with various low-index planes. Thus, we use a linear combination of differently tilted nanocubes as a first approximation to these spheroid NC facets in the spirit of the Derjaguin approximation. There are a few important points to address with regards to the approximation made here. In a real spheroidal NC, different facets have different surface compositions. In our simulations, we only consider Cd-terminated facets. As mentioned above, interactions between [001] and [111] facets are equivalent to those between [001] and [001] facets (Fig. 4.3). Thus, we simplified the interactions between various Cd-terminated facets by replacing them with [001]-[001] interactions. In addition, we will be combining parallel nanocube and small tilt angle nanocube interactions only, which means we can treat these as interactions between flat plates, ignoring all nanocube faces except for the closest ones. Informed by the geometry of a faceted spheroidal zinc-blende CdSe NC, we show quasi-spheres formed from one parallel plate and four, six, or eight tilted plates (e.g., there are four [111]-like and four [011]-like facets for each [001]-like

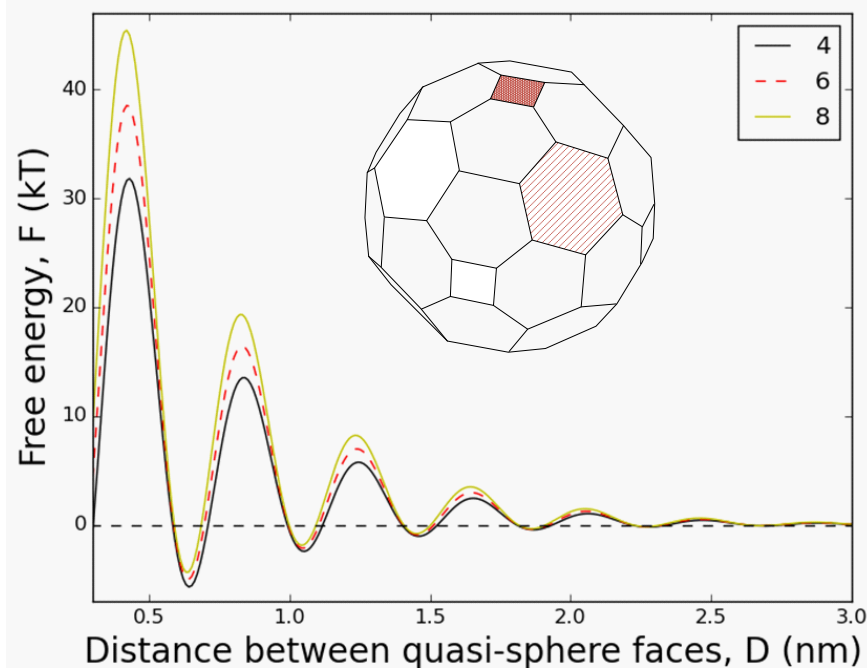


Figure 4.6: Simulated free energy of layering between two quasi-spherical CdSe NCs (10 nm in diameter) in molten KCl. The quasi-spheres are formed by one parallel facet and 4, 6, or 8 tilted facets. Inset shows an example of quasi-spherical particle. The highlighted facets have four and six adjacent tilted facets contributing to the repulsive force between NCs.

facet), as shown in Fig.4.6. For CdSe NCs with a diameter of 10 nm (close to the upper limit of NC size used in our experiments), we find that the troughs are significantly reduced, while the peaks remain high compared to thermal energy ($10\text{-}20 k_B T$) as the two NCs begin to approach within around 1 nm between the closest facets. Such high energy peaks are estimated to be capable to provide long term colloidal stability. These simulation results support our experimentally observed colloidal stability of NCs with finite curvature in molten inorganic salts.

In all the above simulations, we chose a temperature of 1250 K because it is well above the hysteresis loop for our molten salt model and still near the melting point of KCl (~ 1000 K). Note that our molten salt model does not account for polarization fluctuations. However, we expect the above results such as the layering effect and the charge density profile should be general for a wide range of temperatures. In Fig. 4.7, we extract the density profiles near

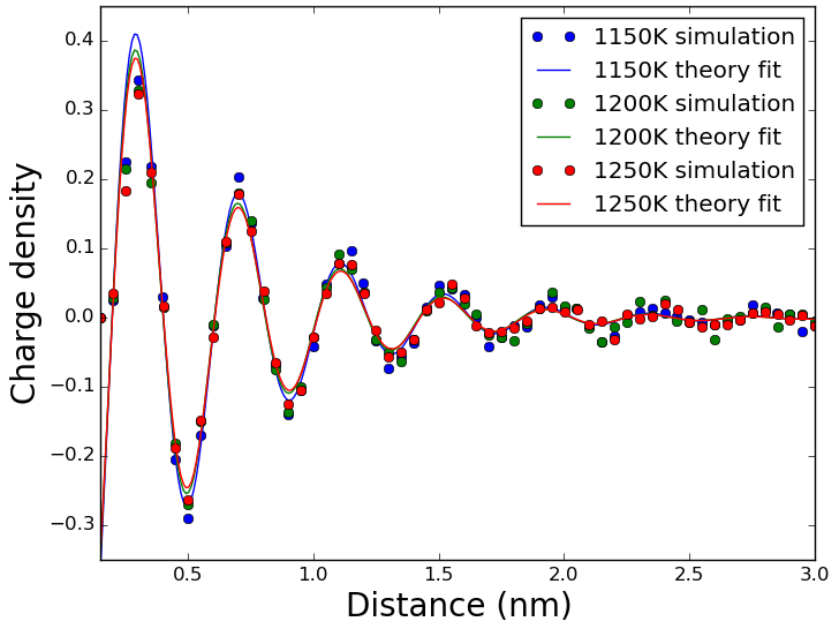


Figure 4.7: Temperature dependence of charge ordering induced by CdSe nanocubes ($2.45 \times 1.85 \times 1.85 \text{ nm}^3$) in molten KCl. Note the first Cd-bound Cl^- peak has been omitted from each charge density profile.

CdSe nanocubes at 1150 and 1200 K and measured the correlation lengths and peak heights. Our theory predicts that the amplitude of the energy of interaction should go as the square of the density at the NCs. Therefore these density profiles allow us to predict how to scale the free energy profiles for systems at these temperatures (Table S1).

4.4.2 Simulations of ion layering on a structureless (or chemically inert) wall

For comparison, we also ran MD simulations on a system with structureless surfaces without chemical affinity to either ion in the molten KCl. The system has LennardJones (LJ) interactions between the solvent and the structureless NC surfaces, and unmodified LJ and Coulomb interactions between the ions. We find that the ion density profiles templated by the structureless NC surfaces are similar to the density profiles of hard sphere templated by

a hard wall. The interaction between the structureless NC surfaces is also very similar to the hard sphere-hard wall system. Without surface charge and/or different chemical affinity for different solvent, oscillatory ion layering observed earlier in the simulation study does not occur. Since much of solvation theory is based on the hard sphere-hard wall system and our control system behaves analogously to the hard sphere-hard wall system, we will briefly compare the phenomenology of the molten salt-NC system (with chemical affinity) and the hard sphere-hard wall system.

In the absence of surface charge or chemical affinity, ion layers still form, but not the alternating oscillations that occur in the presence of surface charge or chemical affinity. Near a hard wall, the density profile of a hard sphere fluid oscillates about the bulk density. The correlation length of these oscillations is related to the radius of the spheres. The solvent-mediated (hard sphere-mediated) interaction between two hard walls is oscillatory, but the source of the oscillations is related to the packing of the hard spheres between the walls (Fig. 4.8). The important factor for the hard sphere-hard wall interaction energy is the space available to the hard spheres to move, i.e., the entropy of the hard spheres. The peaks and troughs of this energy profile are based on the density of hard spheres at the midplane between the two hard walls. When the midplane density is less than the bulk density, the hard wall energy is near a trough; when the midplane density is above bulk, the energy is near a peak. Beyond this oscillating regime (< 0.5 nm), the forces of interaction are usually attractive as demonstrated by our simulations and phenomenological theory (Fig. 4.8). These simulations on a structureless wall are in accordance with our experimental observations of destabilization of NCs in molten salts when there is no chemical affinity between NCs and the ions. We note that Landau-Ginzburg theory predicts repulsion between walls which each bind to a different component of the solvent, but we expect such interactions to be much weaker than the energy scales associated with frustration in inorganic molten salts [113].

Returning to the NC in molten salt system, troughs and peaks correspond to, as dis-

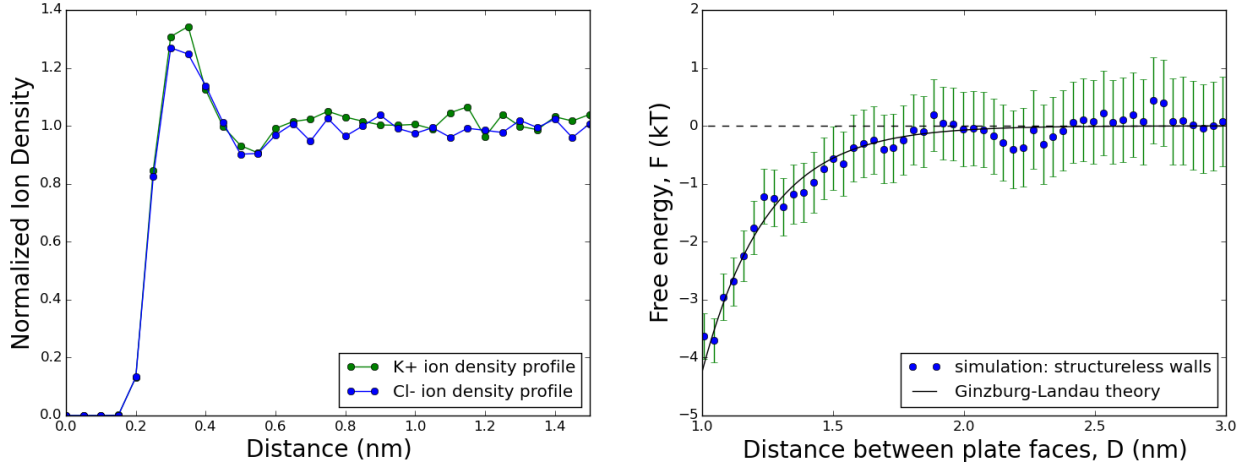


Figure 4.8: Structureless walls are purely attractive. (**Left**) Density profiles of K^+ (green) and Cl^- (blue) around a hard wall. (**Right**) Simulated free energy between two structureless walls in molten KCl and the fit by Landau-Ginzburg theory. Structureless walls do not induce charge oscillations. As a result, the free energy is as predicted by the Landau-Ginzburg theory for solutes which perturb a field in a symmetric manner.

cussed above, coherence and decoherence of the templated molten salt charge density. NC interaction energy is at a minimum when the charge density at the midplane is a peak or a trough. Peak energies occur when there is suboptimal shielding between like-charged solvent layers, i.e., when the charge density at the midplane is zero. The dominant energy contribution determines how the energy depends on the density profiles, and in molten salts, the Coulomb interaction between templated solvent layers is by far the most dominant.

4.4.3 Details of molecular dynamics (MD) simulation

We used the LAMMPS MD package [109] to simulate a molten salt-nanoparticle model system, specifically KCl salt with a CdSe NC. We adapted the models developed by Aguado et al. for molten salts [114] and by Grunwald et al. for solid CdSe [115]. These two models have different forms for the steric and dispersion interactions, with the molten salt using a Born-Mayer-Huggins form and the CdSe crystal using a 6-12 Lennard-Jones form [116]. We chose to use the Born-Mayer-Huggins potential, and adapted parameter values from

Grunwald's force field by finding σ and ϵ for the Cd and Se ions. The parameters used for our model are displayed in Table S2. We simulated an NVT ensemble, with temperature at 1250 K (the melting point for our model is around 1000 K) and with KCl density of 20.681 nm³. We chose box sizes so that neighboring images of the CdSe nanocubes would have negligible interactions: the axis of allowed motion was 21.2 nm in length while the other two axes were 8.9 nm in length. Since the cubes were of size 2.45 × 1.85 × 1.85 nm³ and the largest sampled separation was ∼ 3 nm, this box size leaves more than 16 nm between nearest nanocube images along the axis of motion. We used the LAMMPS-implemented particle-particle particle-mesh solver to implement the long-range Coulomb interactions. We implemented enhanced sampling using the PLUMED code plugin [111]. As a control, we simulated a structureless wall, with no charge and which interacted with solvent only through the 6-8 Lennard-Jones potential. The structureless walls displayed a standard solvent density profile. But long range charge-density oscillations were not observed as there was no surface charge to prefer one ion over the other. Two structureless walls assembled as predicted by the Landau-Ginzburg theory for solutes with a symmetric effect on the order parameter.

CHAPTER 5

NANOCRYSTALS IN MOLTEN SALTS AND IONIC LIQUIDS:

EXPERIMENTAL OBSERVATION OF IONIC CORRELATIONS EXTENDING BEYOND THE DEBYE LENGTH

This chapter reproduces material previously published in Ref. [26]. That work was in collaboration with Vladislav Kamysbayev, Vishwas Srivastava, Olaf J. Borkiewicz, Hao Zhang, Jan Ilavsky, Byeongdu Lee, Karena W. Chapman, Suriyanarayanan Vaikuntanathan, and Dmitri V. Talapin. I shared first authorship with V. Kamysbayev and V. Srivastava, and contributed to the simulation and theory portions of the work. Readers are referred to the original publication for more of the experimental details, which are only summarized here.

In the last chapter, we were motivated by the findings of our experimentalist colleagues, who showed that nanocrystal colloids were colloidally stable within molten salts and ionic liquids. We extended the theory developed in the context of the charge-frustrated Ising model in Chapter 3 as a basis to describe molten salts. With the help of our linear response toolkit, we adapted ideas from the DLVO theory and Derjaguin approximation described in Section 2.1 to apply the frustrated Ising mean field theory to rationalize our MD simulation results, and ultimately, the observed experimental colloidal stability. Specifically, we showed that the surfaces of model nanocrystal colloids interact with high ionic strength fluids and induce charge oscillations within those fluids. The solvent-mediated interaction between plate-like colloids is then oscillatory as well since the order templated by each colloid can interfere constructively or destructively depending on the separation between plates. We further showed that spherical colloids have an additional repulsive term which occurs due to the relative angle between surface normals as the surface of each colloid is traversed. When the plane waves templated in different surface normal directions intersect, no constructive

interference is possible, leading to a net repulsion. Although our simulation and theory coincided well with experimental observations, we lacked direct evidence of the templating of charge oscillations within experiment. Our experimental colleagues moved to remedy that fact, and this chapter begins by describing their observations using X-ray scattering on nanocrystal colloids within molten salts and ionic liquids. In this chapter, we report the results of our MD and theory work on BMIMCl and NaSCN solvent systems, respectively.

The nature of the interface between the solute and the solvent in a colloidal solution has attracted attention for a long time. For example, the surface of colloidal nanocrystals (NCs) is specially designed to impart colloidal stability in a variety of polar and non-polar solvents. This work focuses on a special type of colloids where the solvent is a molten inorganic salt or organic ionic liquid. The stability of such colloids is difficult to rationalize using traditional theories because solvents with high density of mobile charges efficiently screen the electrostatic double layer repulsion, and purely ionic molten salts represent an extreme case where the Debye length is only ~ 1 Å. We present a detailed investigation of NC dispersions in molten salts and ionic liquids using small-angle X-ray scattering (SAXS), atomic pair distribution function (PDF) analysis and molecular dynamics (MD) simulations. My colleagues' SAXS analysis confirms that a wide variety of NCs (Pt, CdSe/CdS, InP, InAs, ZrO₂) can be uniformly dispersed in molten salts like AlCl₃/NaCl/KCl (AlCl₃/AlCl₄⁻) and NaSCN/KSCN, and ionic liquids like 1-butyl-3-methylimidazolium halides (BMIM⁺X⁻, where X=Cl, Br, I). By using a combination of PDF analysis and molecular modeling, we demonstrate that the NC surface induces a solvent restructuring with electrostatic correlations extending an order of magnitude beyond the Debye screening length. These strong oscillatory ion-ion correlations, which are not accounted for by the traditional mechanisms of steric and electrostatic stabilization of colloids, enable colloidal stabilization in highly ionized media.

5.1 Experimental Summary

My experimentalist colleagues characterized the interaction between various ionic fluid-nanocrystal pairs. The interested reader is referred to the original publication for details of their work, [26] which we will only summarize briefly here. They first demonstrated, using transmission electron microscopy before and after, that the morphology of the NCs dispersed and recovered from molten salts was unchanged. Next, they used SAXS to determine which nanocrystal-solvent systems led to dispersed colloids, as compared to worm-like chains or aggregations. In particular, the NaSCN/KSCN and BMIM⁺X⁻ solvent systems were found to stabilize a variety of NCs. Then, they characterized the chemical nature of the ion-NC interaction using FTIR measurements to characterize the tight binding between NC surfaces and ions in SCN⁻ salt systems, and XPS measurements to extract similar binding information in BMIM⁺X⁻ solvent systems. After these characterizations, they proceeded to explore the restructuring of the ionic fluids due to the NCs.

Any changes in local structure of molten inorganic salts and ILs induced by the addition of NC solute can be probed directly with the atomic Pair Distribution Function (PDF) analysis of the high energy X-ray scattering patterns. PDFs are extracted by the Fourier transform of the total X-ray scattering data and can give information about both short-range order (arrangement of atoms within molecules, sharp peaks at 1–5 Å) and intermediate-range order (intermolecular arrangements, broad oscillations at 3–20 Å) in a liquid sample. This ability to probe intermediate-range order can give us valuable information about the solvent layer immediately next to the NC surface. My experimentalist colleagues chose to study the NaSCN/KSCN molten salt system and the BMIM⁺X⁻ ionic liquid system.

To characterize the structuring of ions near a NC, three measurements are required, one of a dry NC powder, one of the bulk solvent, and one of the NC-salt dispersion. The bulk measurement, referred to as the PDF, and shown in Fig. 5.1b, serves as a comparison. In addition, both the bulk and dry powder measurements are subtracted from the NC-salt

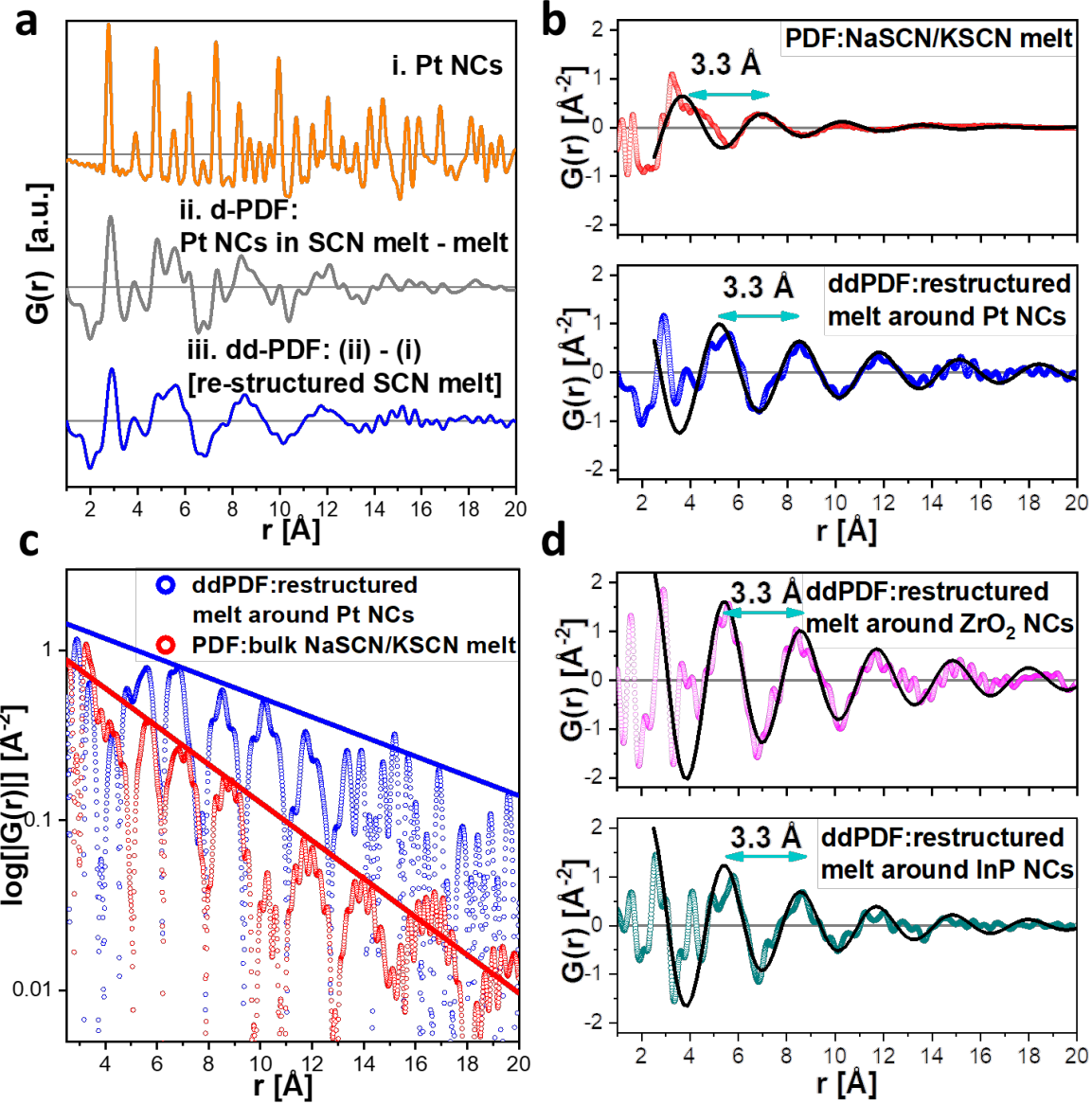


Figure 5.1: (a) Experimental PDF of Pt NCs in the dry powder, d-PDF of Pt NCs capped with S^{2-} ligands in NaSCN/KSCN after the bulk liquid PDF subtraction, and dd-PDF after additional subtraction of the NC contribution. (b) dd-PDF of Pt NCs and NaSCN/KSCN melt curves fitted using exponentially damped sinusoidal functions (black curves). (c) Log plot of the curves from (b) showing the difference in the decay lengths between the restructured and bulk melts. (d) Comparison of the dd-PDFs corresponding to the restructured NaSCN/KSCN melt around ZrO_2 and InP NCs (black curves represent fits).

measurement to give a final result, the “double-differential PDF” or dd-PDF (see Fig. 5.1a). The dd-PDF was observed to have a different structure for a variety of ionic fluid-NC systems. For example, Fig. 5.1b and c compare the PDF of NaSCN/KSCN to the dd-PDF of Pt NCs in NaSCN/KSCN on a linear and log scale, respectively. The phase and decay length are affected, but the wavelength is not, as the wavelength is closely related to the physical size of the ion pair [82]. The difference in the decay length can be most clearly visualized from a logarithmic plot of the absolute value of $G(r)$ (Fig. 5.1c). The decay length increases from 3.9 Å in the bulk to 7.5 Å near the Pt NC surface suggesting that the ion-ion correlations near the Pt surface are more persistent than the ion-ion correlations in the bulk melt. The change in decay length cannot be understood in terms of linear response theories discussed in Section 2.2, which predicts that the decay length is determined entirely by the fluid. The same restructuring was observed for other NCs in NaSCN/KSCN, such as ZrO₂ and InP, see Fig. 5.1d, indicating the phenomenon is somewhat general. In a control experiment using toluene and InP NCs did not show restructuring.

A similar set of experiments and analysis was performed for Pt NCs dispersed in BMIM⁺Cl⁻ IL. As in case of NaSCN/KSCN melt, the decay length increases from 3.6 Å for the bulk IL to 4.4 Å for the restructured IL. In addition to Pt NCs, CdSe and InP NCs in BMIM⁺Cl⁻ IL exhibited dd-PDFs with the distinct phase and increased decay length. These results are summarized in Fig. 5.2a,b and Fig. 5.3.

In a control experiment, my experimentalist colleagues dispersed organic ligand free CdSe NCs in the Lewis neutral BMIM⁺BF₄⁻ IL and performed analogous PDF analysis. The RSF had no signs of the solvent restructuring. Thus, the experiments in the present study led us to similar expectations as in the previous chapter. Specifically, the universal restructuring observed in the Lewis basic NaSCN/KSCN melt and BMIM⁺Cl⁻ IL around various classes of NCs and its absence in Lewis neutral BMIM⁺BF₄⁻ IL supports the hypothesis of Zhang et al. [25], discussed in Chapter 4, that ionic ordering near the NC interface is responsible

for the colloidal stability. SCN^- and Cl^- ions are able to act as X-type ligands which bind to electron-deficient metal-rich facets of NCs and hence form a dense surface-bound layer (Fig. 5.2d). BF_4^- ions, on the other hand, cannot act as X-type ligands and hence do not form a surface-bound layer.

5.1.1 Questions

We were left with a few questions to address through simulation. First, though the experimental dd-PDF gives us a clear picture about how the solvent structuring changes near a NC relative to the bulk, we lack a molecular-scale picture of the details. We cannot resolve the orientation of molecular ions such as BMIM^+ , and we also cannot separate the dd-PDF into components. Thus, a molecular simulation will give us more insight on a smaller scale. Second, we were very intrigued about the alteration of the decay length from the bulk to the NC surface-induced correlations. As repeatedly discussed throughout this text, the linear response relation leads us to expect a single decay length for both types of correlations (in particular see discussion in Section 2.2). We were intrigued to probe the molecular-scale origin of this effect, if possible. And finally, we were interested to extend our previous simulations from the extremely simple molten salt KCl , in which ions are both spherical, to a more complicated solvent system, such as BMIM^+Cl^- or a SCN^- salt.

5.2 Simulation on CdSe nanocrystal colloids in BMIM^+Cl^- solvent system

MD simulations of NCs in BMIM^+Cl^- capture the restructuring of the IL by a NC surface. Our choice to study BMIM^+Cl^- was in part motivated by the availability of the force fields for this IL, which enabled direct comparison of experimental data and MD models [117]. Unfortunately, we could not find the force fields and parameterizations for NaSCN and

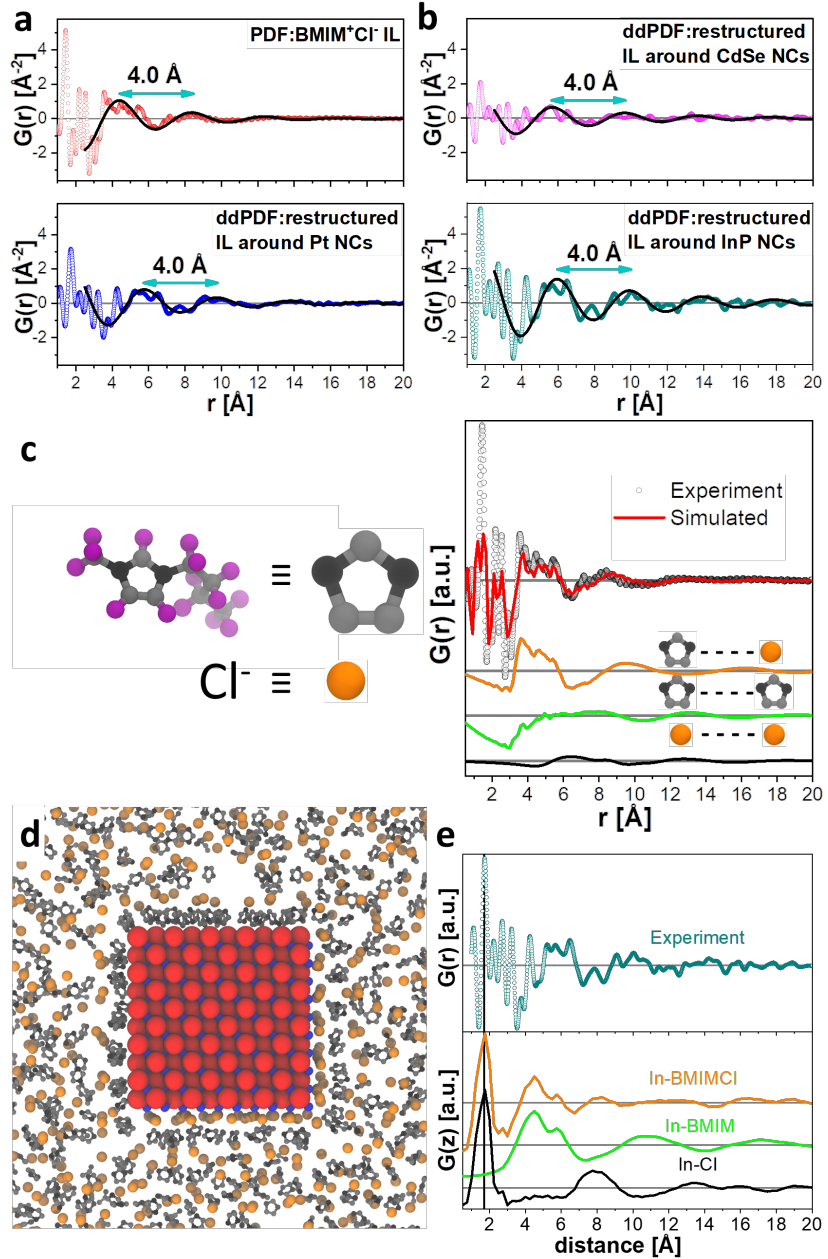


Figure 5.2: (a,b) Comparison of the dd-PDFs corresponding to the restructured BMIM^+Cl^- melt around Pt, CdSe, and InP NCs with PDF of bulk BMIM^+Cl^- (black curves represent the fits). (c) Comparison of the experimental PDFs with the simulated radial PDF of the bulk BMIM^+Cl^- IL, and contributions from the inter-ion structures of $\text{BMIM}^+-\text{Cl}^-$, $\text{BMIM}^+-\text{BMIM}^+$, and Cl^--Cl^- . (d) MD snapshot (zoomed in view) of BMIM^+Cl^- in the vicinity of the cubic zinc blende InP NC (In atoms are blue circles; P atoms are red circles). (e) Comparison of the experimental PDFs with the simulated linear PDFs in the direction of the In-rich NC surface normal, and contributions from surface-ion correlations of In- BMIM^+ , In- Cl^- .

KSCN molten salts which precluded modeling of that solvent system.

We studied a system consisting of bulk BMIM⁺Cl⁻ as well as systems including NCs (model details are provided below in Section 5.4.1). Fig. 5.2c shows the simulated PDF of the bulk BMIM⁺Cl⁻ which is well matched to the experimental data obtained from the total X-ray scattering from pure BMIM⁺Cl⁻, which lends us confidence that the model might be extended to capture colloid-IL interactions. The simulation partial PDFs suggest that the intermolecular intermediate range order is dominated by BMIM⁺-Cl⁻ correlations (orange curve).

We added cubic CdSe and InP nanocrystals to BMIM⁺Cl⁻ solvent to gain molecular-scale insight into the solute-solvent correlations. The solvent structure in the local region near the InP NC was significantly restructured, see snapshot in Fig. 5.2d, but the structuring decayed after a few molecular layers (CdSe NCs induced similar restructuring). We extracted the density profiles of BMIM⁺Cl⁻ normal to the In-terminated (001) surface of a cubic zinc-blende InP NC. We plot these profiles, which vary with distance (z) from the NC surface along with experimental dd-PDF, which varies with the radial distance (r) (Fig. 5.2e).

Interestingly, these measurements show a good match, in particular, between the small-distance large peak (at ~ 1.7 Å), identified from the simulations as the Cl⁻ ion adhered to the In surface, and the second broad peak ($\sim 4\text{--}6$ Å) identified as a layer of BMIM⁺ ions immediately following the first Cl⁻ layer. A snapshot of the simulation (Fig. 5.2d) clearly suggests that Cl⁻ ions form a dense layer on the In-terminated surface followed by a dense layer of BMIM⁺ ions before the density correlations slowly decay to become bulk-like. Recent elemental analysis of InP NCs with Rutherford backscattering spectroscopy and XPS suggest that InP NCs are almost 100% In terminated [118]. Hence, there should be little contribution from the correlations between negatively-charged (P terminated) facets and BMIM⁺ ions to the total pair distribution function. And with the surprising extent to which the In-IL normal-direction solvent profile correlates with the experimental dd-PDF,

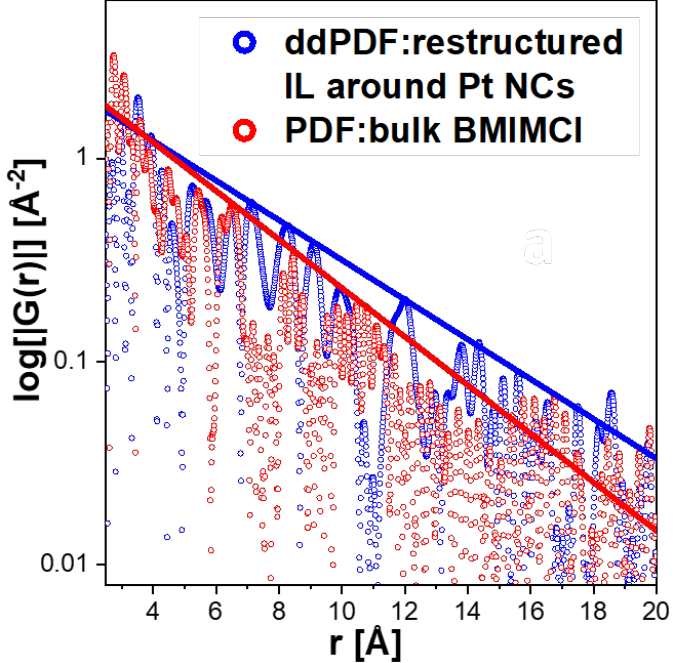


Figure 5.3: Log plot comparing the decay of correlations in BMIM^+Cl^- bulk solvent and BMIM^+Cl^- with Pt NCs. As in the SCN^- salt system, the restructured decay length is larger than bulk, but the increase is smaller here, compare with Fig. 5.1c.

it appears that the MD results are in agreement.

The features of this surface-induced density profile do not change significantly for the different surfaces presented by InP and CdSe NCs in simulation, nor Pt NCs in experiment (Fig. 5.2a). Thus, the restructuring of the BMIM^+Cl^- solvent by a metal rich surface is robust to changes in the specific composition of the surface. Further, the restructuring observed in the experiment appears to consist largely of the order induced normal to the NC surface. However, the MD simulations were not able to reproduce the experimental observation of an increase in decay length due to the NC templated order. Thus, while the experimental results seem to violate the predictions of linear response theory, the MD results do not.

5.3 Conclusions

In conclusion, X-ray PDF analysis and MD simulations provide evidence for the formation of a layered ionic solvation shell around NCs dispersed in molten inorganic salts and organic ionic liquids. The solvation shell has enhanced ion-ion correlations compared to the bulk liquid and extends far beyond the Debye screening length. The solvent restructuring happens only for those molten salts where ions are able to function as surface-bound ligands for dispersed NCs. Surprisingly, the decay length of ionic correlations is observed to increase when measured for the NC-induced restructuring relative to unperturbed bulk structure. This effect appears to be solvent dependent. The charge density wave consisting of the restructured ions generates an oscillatory potential between NCs and hence constitutes a fundamentally different mechanism of colloidal stabilization in addition to the standard electrostatic and steric mechanisms. We believe that detailed understanding of the NC solvation in highly ionized media of inorganic melts and ionic liquids is necessary for the rational design of the colloidal systems in these unconventional media. The improved design of the colloidal state in the high temperature inorganic molten salts can assist development of a variety of hard-to-crystallize colloidal nanomaterials.

5.4 Methods

5.4.1 Molecular dynamics model

The BMIM⁺Cl⁻ IL system was studied using the CLDP forcefield for ionic liquids, a timestep of 0.5 fs and a short-ranged pairwise cutoff distance of 12 Å [117]. We ran molecular dynamics simulations using the LAMMPS software package, [109] and visualized trajectories using the VMD package [88]. The long-range part of the Coulomb interaction was implemented using the particle-particle particle-mesh scheme, with relative error of 10⁻⁴.

Nanoparticles of CdSe, InP, and chemically inert types were implemented by setting short-

range interactions equivalent to those of C2 carbons in the CLDP force field and including appropriate partial charges [115, 119]. Mixing the partial charges from a crystal model with the CLDP force field is necessarily approximate, but we expect it to be a reasonable approximation and agreement between the simulation and experimental results bears out that expectation. The interatomic distances in the nanoparticle solutes were rigidly fixed. Our choice to model the short-range interaction in such an approximate way was informed by simulation work on ionic liquid interactions with Au electrodes where the Au short-range interactions were set as graphite carbons [120]. The most important factor by far appears to be the charge of the surface, with the short-range interactions providing only a perturbation. Since most of the ion specific interactions between the NC and the solvent is due to the Coulomb interaction, setting the charge of the NC to zero is effectively the same as making it chemically inert. And indeed, we observed that the structuring of the IL did not occur when the Coulomb interaction between nanoparticle and solvent was set to zero. Though not meant to be physically meaningful, this test confirms that the short-range interactions and exclusion volume due to the nanoparticle is not responsible for the restructuring of the IL.

Simulations were run at constant temperature and pressure with a temperature of 400 K using the Nose-Hoover thermostat and a pressure of 1 bar using the Nose-Hoover barostat with coupling parameters of 500 fs and 1000 fs respectively. In runs with nanoparticles, the nanoparticles were allowed to rotate freely and were subject to a Langevin thermostating at 400 K. Bulk simulations consisted of 480 BMIM⁺ and 480 Cl⁻ ions. Simulations with nanoparticles consisted of two sets. In the first set, nanoparticles were cubic with sides approximately 3 nm in length. The nanoparticles were cut such that for CdSe (InP) there were three Cd (In) coated facets and three Se (P) coated facets. All facets were (100). For these simulations, 3630 BMIM⁺ and 3630 Cl⁻ ions were used, leading to a cubic periodic box of roughly 10.5 nm in length. Larger simulations with 3 nm nanoparticles and box sizes

up to 20 nm in length were used to confirm finite size effects were not an issue for the 10.5 nm box size.

Bulk simulations consisted of 480 BMIM⁺ and 480 Cl⁻ ions. Simulations with nanoparticles consisted of two sets. In the first set, nanoparticles were cubic with sides approximately 3 nm in length. The nanoparticles were cut such that for CdSe (InP) there were three Cd (In) coated facets and three Se (P) coated facets. All facets were (100). For these simulations, 3630 BMIM⁺ and 3630 Cl⁻ ions were used, leading to a cubic periodic box of roughly 10.5 nm in length. Larger simulations with 3 nm nanoparticles and box sizes up to 20 nm in length were used to confirm finite size effects were not an issue for the 10.5 nm box size.

5.4.2 Molecular dynamics analysis

Radial distribution functions for all ion pairs were extracted from simulation trajectories. These were convoluted with appropriate atomic form factors for comparison with experiment [121, 122, 123]. Atomic form factors were approximated using sums of four Gaussians, which is a good approximation for small q [124]. The surface-induced correlations were also measured by computing the probability of observing the various fluid atom types in front of each surface of the nanoparticle as a function of the distance along surface normal. Similar post-processing with atomic form factors was required for comparison with experiment.

For comparison with experimental restructured reduced structure factors, the radial distribution functions of ion pairs were also extracted from solvent systems including nanoparticles. In these RSFs, crystal-crystal (Cd-Cd, Cd-Se, etc.) correlations were excluded from sums over all particle pairs, as otherwise, the crystal-crystal contributions dominate the less-ordered liquid-liquid and crystal-liquid contributions.

5.4.3 Estimating the interaction free energy between two small nanoparticles

For small particles (ie. when the separation between particles is comparable to the size, $D \sim R$) the Derjaguin approximation, as applied in Section 4.3, is no longer applicable. To attempt to remedy this defect, in this section, we will derive the solvent-induced free energy of interaction between two NCs as a linear combination of tilted facets. Since the majority of NCs are faceted, it is reasonable to approximate shape of Pt NCs by a spheroidal shape. Here, we represent Pt NCs as a truncated icosidodecahedron [125]. The total interaction free energy is then a linear combination of the interaction free energies between one pair of parallel facets (decagons) and five pairs of tilted facets (squares and hexagons):

$$F_{icos}(D) = A_{10}F_p(D) + \frac{5a}{2\sin(\theta_4)} \int_D^{D+\Delta_4} dz [F_p(z) + F_t(z, 2\theta_4)] \\ + \frac{5a}{2\sin(\theta_6)} \int_D^{D+\Delta_6} dz [F_p(z) + F_t(z, 2\theta_6)] \frac{w(z-D)}{a}, \quad (5.1)$$

with $F_p(z)$ defined in Eq. 4.10 and $F_t(z, \theta)$ defined in Eq. 4.13, $A_{10} \equiv 5a^2 \cot(\pi/10)/2$ the area of the decagon, a , defined by $a^3 \equiv \frac{4}{3}\pi R^3 \frac{6}{45+17\sqrt{5}}$ corresponds to the edge length of a truncated icosidodecahedron, $\Delta_4 \equiv 2a \sin(\theta_4)$ the additional separation between two squares at the angle $\theta_4 \equiv \pi - \arccos(-\sqrt{10(5+\sqrt{5})}/10)$ away from parallel, $\Delta_6 \equiv 4a \cos(\pi/6) \sin(\theta_6)$ the additional separation between two hexagons at the angle $\theta_6 \equiv \pi - \arccos(-\sqrt{15(5+2\sqrt{5})}/15)$ away from parallel [125], and

$$w(z) = \begin{cases} a + z \frac{\tan(\pi/6)}{\sin(\theta_6)} & z \leq \Delta_6/2 \\ a + (\Delta_6 - z) \frac{\tan(\pi/6)}{\sin(\theta_6)} & z > \Delta_6/2. \end{cases} \quad (5.2)$$

CHAPTER 6

EXTENDING THE CHARGE-FRUSTRATED ISING MODEL

The charge-frustrated Ising model that was the subject of Chapter 3 provides a concrete basis for the study of coarse-grained ionic fluids in high and low temperature regimes. As discussed, a continuum theory, equivalent in form to a theory accounting for the finite size of charged hard spheres [57] truncated at k^4 , can be derived starting from a mean field theory of the FI lattice model. However, a major limitation of the work presented in Chapter 3 was that we only studied a highly symmetrical pure fluid without defects or the inclusion of colloids of any kind. In particular, in our study we were unable to reproduce the experimentally observed scaling of the screening constant, $\kappa_s \sigma \sim (\kappa_D \sigma)^{-2}$ [1], and we hypothesized that some of the limitations just mentioned might be causing the mismatch between our results and experiment. To remedy some of these limitations, we will discuss some unpublished results from a follow up study in this chapter.

The results presented are along two different lines, as we were interested in generalizing two different parts of the model. First, we discuss the inclusion of solutes within the FI model, and show that the bulk screening length and solute-induced screening lengths are equivalent, as predicted by linear response. Next, we discuss generalizations of a pure fluid without solutes. The work discussed in Chapter 3 focuses on lattice sites with symmetric charge and size, and also lacked defects. However, defects have been suggested to be important for the realization of the experimental screening length scaling [1]. In the present chapter, we discuss the breaking of the charge valence symmetry and the inclusion of defects within the lattice. A simple extension of the mean field theory derived in Section 3.6 appears to capture some important features of the scaling of the screening length within these systems, though it runs into the same breakdown for large $\rho Q/J$ ratios as discussed in Chapter 3. We are also interested in breaking the charge size symmetry, and this work is ongoing. In the future, we also plan to measure the free energy of interaction between solute plates as a

function of separation to confirm that linear response governs this length scale as well.

6.1 Solutes

We model solutes within the FI model as a set of sites, each with a defined valence and position relative to a center of mass. We may optionally choose to allow the center of mass to translate and rotate, which define new Monte Carlo moves in addition to the swap or cluster move that advances the solvent through time. The details of such moves are discussed in Section 6.4. Importantly, charge neutrality is always carefully preserved. In the results that follow, the parameters are set to $J = 1$, $Q = 0.5$ and $\sigma = 1$, using the notation from Chapter 3, and the Hamiltonian of the system can be found in Eq. 3.1. A set of snapshots from simulations are shown in Fig. 6.1.

6.1.1 Charge density profiles

A charged, plate-like solute ($20\sigma \times 20\sigma \times 4\sigma$) is placed in long, rectangular simulation box ($50\sigma \times 50\sigma \times 54\sigma$) and allowed to translate, but not rotate. The solute is composed of lattice sites which are all charges/spins of valence +1. The system is enforced to be overall neutral, so the solvent has a slight excess of -1 charges. We have also compared screening length results from this system setup to one in which a counter-plate made of -1 charges is held as far from the positive plate as possible to determine if the presence of extra negative charges in the solvent has an effect on the results, but no difference is observed.

The charge density profiles are extracted from simulation and displayed in Fig. 6.2 and 6.3 for a variety of temperatures, corresponding to a variety of different $\kappa_D\sigma$ values. Qualitatively, the profiles appear as expected, with low $\kappa_D\sigma$ profiles decaying exponentially and high $\kappa_D\sigma$ profiles decaying with damped oscillations. Further, the trend of the screening length with the Debye constant is qualitatively similar to that reported in Chapter 3, where the screening length increases with temperature in the high T , low $\kappa_D\sigma$ regime, while decreasing

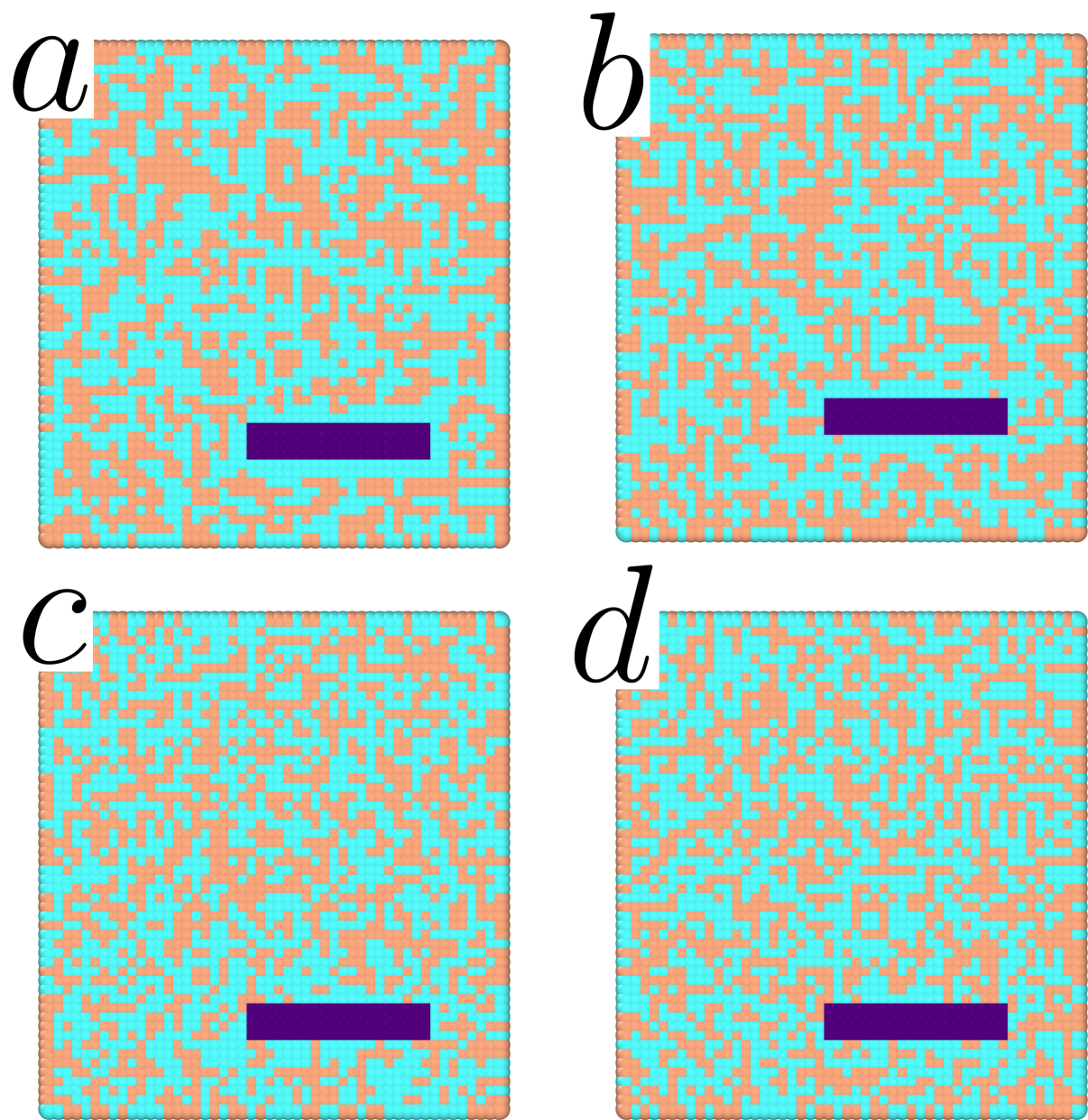


Figure 6.1: Snapshots from simulation for different temperatures with $\rho Q/J = 0.5/\sigma^2$. Plus charges are brown, minus charges are blue. Simulations are visualized using Ovito [2]. **a**, T=3. **b**, T=5. **c**, T=20. **d**, T=100.

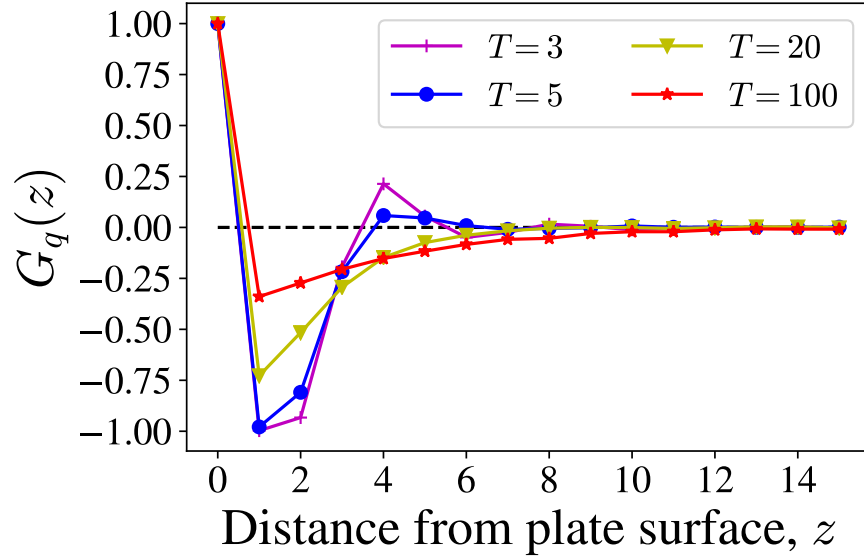


Figure 6.2: Charge density profiles for plate of size $20\sigma \times 20\sigma \times 4\sigma$ in simulation box of size $50\sigma \times 50\sigma \times 54\sigma$, linear scale. The value of $G_q(z)$ at 0 is the positive surface charge of the plate. The regime change can be seen qualitatively as the oscillations in $T = 3$ become less pronounced in $T = 5$ before disappearing entirely by $T = 20$, which exhibits pure exponential decay.

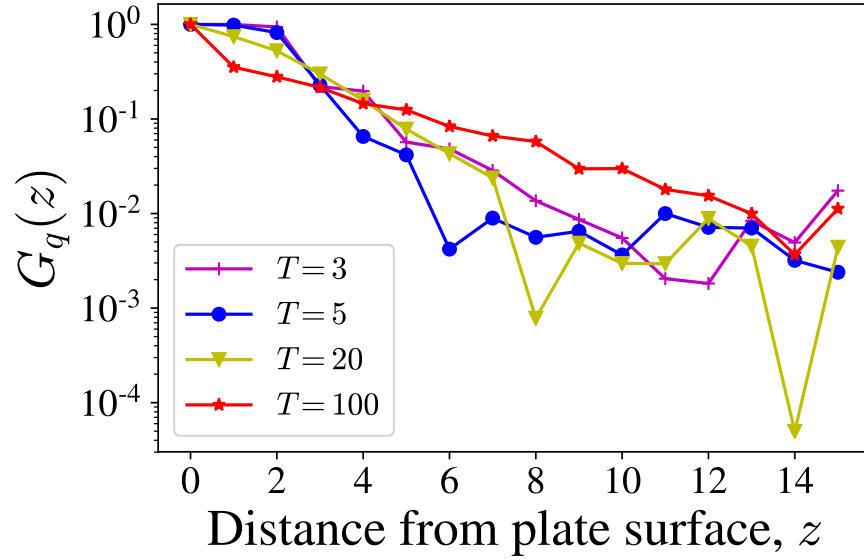


Figure 6.3: Charge density profiles for plate of size $20\sigma \times 20\sigma \times 4\sigma$ in simulation box of size $50\sigma \times 50\sigma \times 54\sigma$, log scale. The value of $G_q(z)$ at 0 is the positive surface charge of the plate. Here, the qualitative change in the behavior of the correlation length

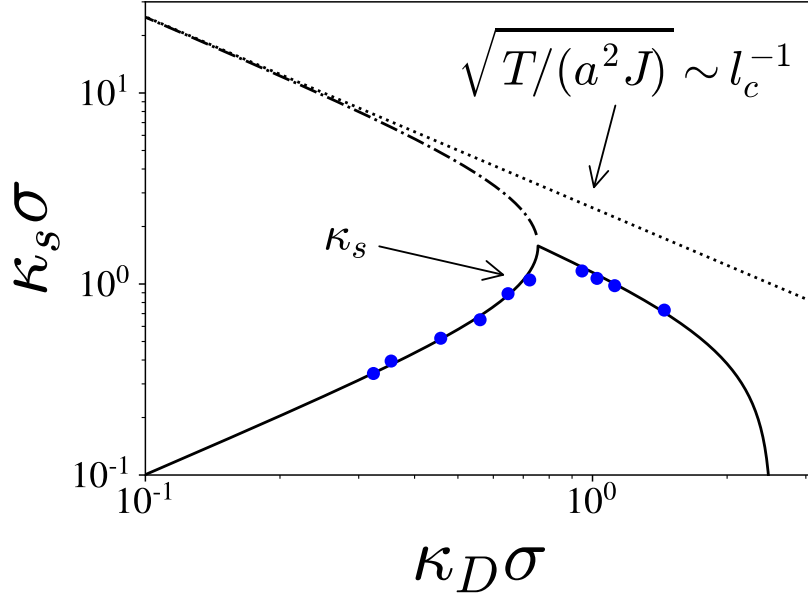


Figure 6.4: Screening constant measured from the single-plate charge density profiles as a function of the Debye screening length.

with temperature in the low T , high $\kappa_D\sigma$ regime.

It is simple to extract the decay length of the charge density profile, using methods discussed in Chapter 3, and these inverse decay lengths are plotted against $\kappa_D\sigma$ in Fig 6.4. For comparison, the theory prediction for the bulk inverse screening length is also shown on the same plot. As expected from linear response arguments, the charge density profile induced by the solute decays with the same length scale as do bulk charge-charge correlations.

6.1.2 Potential of mean force between two solutes

The next step in the study of colloidal plates in the FI model is to measure the free energy of interaction, or potential of mean force, between two plates, analogous to the measurements performed for molecular dynamics in Chapter 4. However, for technical reasons, which we now briefly discuss, this measurement is somewhat more complicated in a lattice model than in a continuous space model such as MD.

To accurately measure the PMF between two plates, both high and low free energy portions of the PMF must be sampled. Harmonic constraints, or “umbrellas”, are frequently used to bias the plate separation towards a specific value, and statistical methods are used to de-bias a set of such constrained measurements after the simulations are completed [112]. For the solute model on a lattice introduced above, the smallest move that can be made in a given direction is σ , which puts a practical upper limit on the spring constant that can be used for harmonic constraints, since too large a spring constant will prohibit moves of σ on reasonable simulation timescales. Contrast the lattice case with a simulation in continuous space, like molecular dynamics, where arbitrarily small (within computer precision) variations in separation can occur, allowing for sampling over a range. An additional confounding issue for large $\kappa_D\sigma$ simulations is that a solute move will disrupt the local ordering of the fluid. For moves that are constrained to be within a few σ , the smaller the distance of the move, the larger the disruption (since the local ordering decays with distance). Thus, when umbrella sampling is performed in the large $\kappa_D\sigma$ regime, small moves are penalized by local solvent ordering, while large moves are penalized by harmonic constraints, leading to a situation where any solute moves become exceedingly unlikely. To make matters worse, solute moves are already unlikely for plates which have area $(20\sigma)^2$, since the disruption to the fluid ordering scales with the area of the plate. It might be desirable to use plates with smaller area, then, except that plates which are too small do not sufficiently perturb the solvent.

6.2 Asymmetric Solvent and Defects

6.2.1 Asymmetric charge and spin

In our previous work, discussed in Chapter 3, we considered the FI lattice with symmetric charges for various $\rho Q/J$ ratios. Here, we generalize that work by varying the valence of the

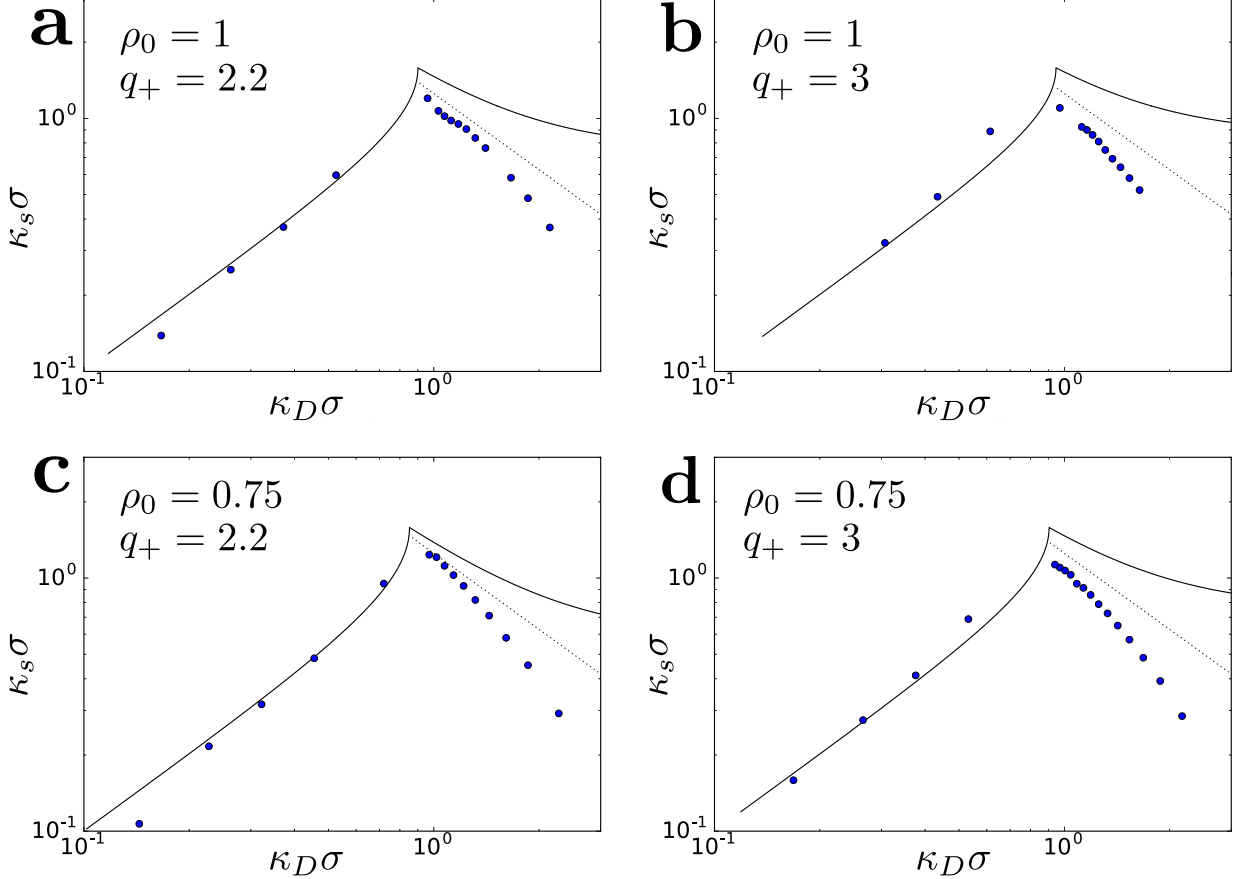


Figure 6.5: Scaling of inverse screening length for different asymmetric charge systems. Each system has $\rho Q/J = 0.5/\sigma^2$. (a),(b) $\rho_0 = 1$, and the asymmetric plus charge has valence $q_+ = 2.2$ and $q_+ = 3$, respectively. (c),(d) $\rho_0 = 0.75$, and the asymmetric plus charge has valence $q_+ = 2.2$ and $q_+ = 3$, respectively. In all four cases, the simple modification to the mean field theory does a good job capturing the DH regime and gives a reasonable prediction of the regime change point, κ_D^* . For large $\kappa_D\sigma$, the scaling $\kappa_s \sim 1/l_c$ shown as the dotted line captures the scaling close to the regime change, but does poorly as κ_D continues to be increased. As discussed in Chapter 3, the critical temperature becomes unphysically negative when $\rho Q/J$ becomes too large, and that may explain the divergence between the theory predictions and simulation results in the large $\kappa_D\sigma$ regime.

positive charge type while keeping $\rho Q/J = 0.5/\sigma^2$ fixed. Specifically, we set the negative charge and spin values to -1 , and the positive charge and spin values to $+2.2$ or $+3$ (these specific valences were chosen so that the lattice with $L = 32\sigma$ could be neutral with proper ratio of $+$ and $-$ charges). Physically, varying the valence of oppositely charged spins allows us to account for the fact that real ions vary in their valence.

A simple modification of the mean field theory presented in Section 3.6 leads to a qualitative prediction of the simulation results, specifically capturing the low $\kappa_D\sigma$ regime and the point at which regimes change, $\kappa_D^*\sigma$. The modification to the theory presented in past work can be expressed simply as

$$Q' \rightarrow Q |q_+ q_-|, \quad (6.1)$$

and

$$J' \rightarrow J |s_+ s_-| \quad (6.2)$$

with Q , J the effective strengths of the Coulomb and Ising interactions, respectively, q_+ , q_- the charge valences, and s_+ , s_- the spin valences. The scaling of the inverse screening length for $q_+ = s_+ = 2.2$ and $q_+ = s_+ = 3$ is shown in Fig. 6.5a,b, respectively. The simple mean field theory does a good job predicting the DH regime, and does reasonably as predicting the regime change. However, in the large $\kappa_D\sigma$ regime for the parameters chosen here, the predictions of the theory and the observations from simulation disagree. One possible explanation for this disagreement is that the breakdown of the continuum mean field theory for large $\rho Q/J$ discussed in Chapter 3 persists here, leading to a negative critical temperature and to poor predictions in the large $\kappa_D\sigma$ regime as a result.

6.2.2 With defects

We generalize the model to consider defects as well, ie. sites which are unoccupied by a charge or, equivalently, which are charge 0. In previous work on the FI model, the number

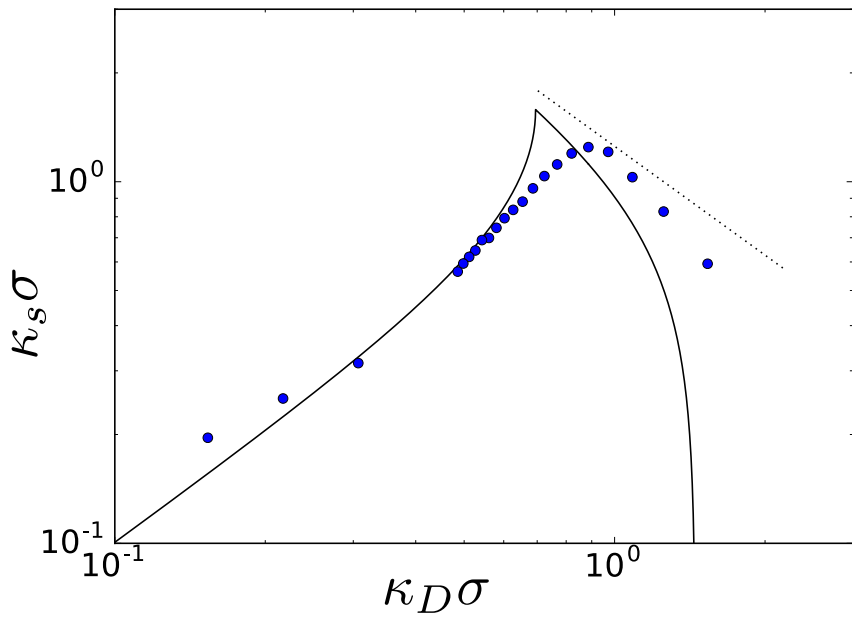


Figure 6.6: Scaling of inverse screening length for $\rho Q/J = 0.5/\sigma^2$ and $\rho_0 = 0.75$. The simple modification to the mean field theory captures the DH regime and does a reasonable job predicting the regime change point, κ_D^* , but predicts larger length scale decay than observed in theory in the large $\kappa_D\sigma$ regime.

of defects has been tuned to control the density of charges, and hence, $\kappa_D\sigma$ [66]. Here, we select a few charge densities, and tune the temperature as before.

First, we consider the case that the charges are symmetric, but have a density less than 1 on the lattice. In this case, considering for generality the valence of charges, we find

$$Q' \rightarrow Q\rho_0 |q_{+}q_{-}|, \quad (6.3)$$

and

$$J' \rightarrow J\rho_0 |s_{+}s_{-}| \quad (6.4)$$

where ρ_0 is the dimensionless number density of occupied sites on the lattice. The cases of $\rho_0 = 0.75$ for $q_{+} = s_{+} = 2.2$ and $q_{+} = s_{+} = 3$ are shown in Fig. 6.5c,d, respectively. As in the case just discussed, although the DH and regime change are well-predicted by this simple mean field theory, the large $\kappa_D\sigma$ regime is not well captured.

When $\rho\rho_0Q/J$ is small enough to avoid the continuum mean field breakdown, the simple proposed modification to the theory gives qualitatively accurate predictions. Fig. 6.6 shows the scaling of the inverse screening length when $\rho_0 = 0.75$ and $\rho Q/J = 0.5/\sigma^2$ with symmetric charges.

6.2.3 Asymmetric size

Another generalization of the solvent we plan to study is a solvent with asymmetrically-sized ions. In the real world, ions are always asymmetrically sized, and considering the importance of short-range length scales in the physics of the large $\kappa_D\sigma$ regime (see discussion in Chapters 2 and 3), size asymmetry may have non-trivial effects. One simple way to achieve size-asymmetric ions in the FI framework in three dimensions is to make all of one type of charge carrier, say the $-$, into a $2\sigma \times 2\sigma \times 2\sigma$ cube where each site has a valence of $-1/8$. Gauss's law ensures that other sites on the lattice will see this "large ion" as having a charge

of -1 concentrated at its center of mass. A simulation study of size-asymmetric ions is underway.

6.3 Future work

The work presented in this Chapter only represents the first step towards generalizing the FI model introduced in Chapter 3. The charge correlations induced by a solute are shown to decay with the same length scale as bulk charge correlations, as expected from linear response. We would like to study the interactions between solutes, but doing so requires surmounting some technical obstacles. One of the strengths of the FI model is that its simplicity allows it to be scaled to larger systems more easily than more complicated models. We are interested in probing the possibility of many-solute “trapped” superlattice states, as hinted at in Chapter 4. The oscillatory nature of the repulsive potential between solutes may lead to local free energy minima and to such superlattice states.

We are also very interested in furthering our study of asymmetric solvents (and perhaps how these interact with solutes). A generalization of the mean field model derived in Chapter 3 seems to be sufficient to explain the DH regime and the regime changeover for the current results, but questions remain regarding the large $\kappa_D\sigma$ regime. At a minimum, the theory must be improved so that the critical temperature does not become negative. Grousson and Viot [42] develop a theory that avoids a negative critical temperature by a more careful accounting for the lattice nature of the problem, and such an approach might be of use here. Another related possibility is the explicit inclusion of the finite size of “particles” or cells, as in the work of Adar and coworkers [57], discussed in Section 2.6. Size- or shape-asymmetric solvent is also of interest because of our intuition that the short-range features of ionic fluids play such an important role in bringing about the large $\kappa_D\sigma$ regime. The interactions between size- or shape-asymmetry and the confinement by interacting solutes could lead to some interesting physics.

6.4 Appendix: Allowing solutes to translate and rotate

Solutes are represented as a center of mass and a set of positions relative to the center of mass that specify the sites which are contained in the solute. The sites contained in the solute have an identity that is fixed at the start of the simulation. Here, all sites have a value of +1. For each step of the simulation, a random site is selected. If that site is not contained within a solute, a swap or cluster move is attempted. When that site is contained within a solute, the containing solute is the subject of a move attempt. d numbers, with d the dimension, are generated uniformly up to some user specified maximum. These d numbers constitute the proposed center of mass translation. The solute, and, optionally, a shell of solvent around the solute (to attempt to reduce the energy cost of the proposed move), is moved, and the solvent displaced by the solute's new proposed position is randomly placed within the vacated sites. The energy of the new configuration is computed and the standard Metropolis rule is used to determine if the move is accepted. Solutes may also have rotational freedom. For solutes with rotations enabled, an additional step occurs during the proposal of the move. Rotation matrices about each axis are chosen in a random order, and with a random magnitude, from $[0, 3\pi/2]$ in increments of $\pi/2$.

6.4.1 Increasing the probability of solute moves by relaxing local solvent

For large $\kappa_D\sigma$, or low temperature, the solvent forms layers of charge in response to the solute. When the solute is relatively large, any proposed solute move will cause a significant disruption of the solvent layering, leading to a prohibitively high energy cost and a vanishingly small probability to accept the move. One method to increase the probability of moves is to move not just the solute, but also the local solvent shell around the solute, which can reduce disruption in the local region around the solute. Another method is to relax the solvent in a local region around the solute as a part of the solute move. To satisfy detailed balance, the local region around the solute and its proposed location must be relaxed before

and after the move. The result of the analysis is that when these local regions are relaxed with an effective temperature $T_{eff} > T$, it is possible for the overall proposed move to be more likely to be accepted than a simple, no-relaxation solute move. This method is detailed now.

Consider a Monte Carlo move attempt which consists of the following stages on a trial lattice initialized to the same starting configuration as the current lattice: (1) randomly selecting a translation of the solute center of mass, but not yet moving the solute; (2) within a local solvent region surrounding both the current solute position and proposed solute position, make N_{local} swap move attempts at effective temperature T_{eff} which may not be equal to T ; these are accepted or rejected according to the standard Metropolis method; (3) move the solute to its proposed position; (4) make another N_{local} swap move attempts at temperature T_{eff} within the same region as part (2). This whole set of operations is then accepted or rejected according to the Metropolis prescription. The pre-solute move N_{local} swap moves are required in order to make the entire move symmetric to satisfy detailed balance.

I'm going to write down the detailed balance condition, and then find an expression for the acceptance probability ratio of the move just described. Comparing this expression to that of the solute move alone without any solvent relaxation will provide the conditions under which it is favorable to relax the local solvent.

$$p_i \ p_{prop}^{i \rightarrow f} \ p_{acc}^{i \rightarrow f} = p_f \ p_{prop}^{f \rightarrow i} \ p_{acc}^{f \rightarrow i}, \quad (6.5)$$

with p_i and p_f the probability of observing the initial or final state, respectively, p_{prop} the probability of proposing a particular move, and p_{acc} the probability of accepting a particular move. It can be manipulated to

$$\frac{p_{acc}^{i \rightarrow f}}{p_{acc}^{f \rightarrow i}} = \frac{p_f}{p_i} \frac{p_{prop}^{f \rightarrow i}}{p_{prop}^{i \rightarrow f}}. \quad (6.6)$$

Next, we write down each of these fractions on the right hand side in order to compute the acceptance probability. The change in energy due to the proposed move described above can be written

$$E_f - E_i = \Delta E_{swap}^{su:i} + \Delta E_{su} + \Delta E_{swap}^{su:f}, \quad (6.7)$$

with $\Delta E_{swap}^{su:i}$ the change in energy due to the first set of swaps which are accepted while the solute (abbreviated “su”) is at position i , ΔE_{su} the change in the energy when the solute is moved after the first set of swaps and before the second, and $\Delta E_{swap}^{su:f}$ the change in energy for the final set of swap moves after the solute has been moved on the trial lattice. Then the first fraction on the right hand side of Eq. 6.6 can be written

$$\frac{p_f}{p_i} = \exp \left[-\beta \left(\Delta E_{swap}^{su:i} + \Delta E_{su} + \Delta E_{swap}^{su:f} \right) \right], \quad (6.8)$$

with β the inverse of the thermal energy.

Now consider the second fraction, which takes the form

$$\frac{\frac{p_{prop}^{f \rightarrow i}}{p_{prop}^{i \rightarrow f}}}{\frac{p_{prop}^{f \rightarrow i}}{p_{prop}^{i \rightarrow f}}} = \frac{\left[\prod_j^{N_{local}} p_{swap,j}^{su:f} \right]^{f \rightarrow i} \times \left[p_{prop}^{su:f \rightarrow i} \right]}{\left[\prod_j^{N_{local}} p_{swap,j}^{su:i} \right]^{i \rightarrow f} \times \left[p_{prop}^{su:i \rightarrow f} \right]} \times \frac{\left[\prod_j^{N_{local}} p_{swap,j}^{su:i} \right]^{f \rightarrow i}}{\left[\prod_j^{N_{local}} p_{swap,j}^{su:f} \right]^{i \rightarrow f}}, \quad (6.9)$$

where the probability to propose a solute move from $i \rightarrow f$ is

$$\frac{p_{prop}^{su:f \rightarrow i}}{p_{prop}^{su:i \rightarrow f}} = \frac{\frac{V_{su}}{V} \times \frac{1}{V_{local}}}{\frac{V_{su}}{V} \times \frac{1}{V_{local}}} = 1, \quad (6.10)$$

with V_{su}/V the probability to uniformly select the solute from amongst all lattice sites and $1/V_{local}$ the probability to propose a specific new center of mass amongst V_{local} options. The $p_{swap,j}^{su:state}$ terms are different from other p_{prop} terms which are usually uniform because each

swap move is a self-contained Metropolis move which can either be accepted or rejected

$$p_{swap.j}^{su:state} = \min \left[1, \exp \left(-\beta_{eff} \Delta E_{swap.j}^{su:state} \right) \right]. \quad (6.11)$$

Consider solute state i . There is a sequence of N_{local} swap moves starting from the initial configuration and ending with the configuration from which the solute is moved. In the hypothetical reverse move, starting from f , swap moves occur, the solute is moved, and then the set of N_{local} swap moves is traversed in the opposite direction, ie. if we number the swap move states $0, 1, \dots, N_{local} - 2, N_{local} - 1$, then in the reverse move they are traversed $N_{local} - 1, N_{local} - 2, \dots, 1, 0$. Then

$$\begin{aligned} \frac{\left[\prod_j^{N_{local}} p_{swap.j}^{su:i} \right]^{f \rightarrow i}}{\left[\prod_j^{N_{local}} p_{swap.j}^{su:i} \right]^{i \rightarrow f}} &= \frac{\prod_j \min \left[1, \exp \left(\beta_{eff} \Delta E_{swap.j}^{su:i} \right) \right]}{\prod_j \min \left[1, \exp \left(-\beta_{eff} \Delta E_{swap.j}^{su:i} \right) \right]} \\ &= \prod_j \exp \left(\beta_{eff} \Delta E_{swap.j}^{su:i} \right), \end{aligned} \quad (6.12)$$

where the sign differs in the numerator and denominator because the steps happen in opposite directions. Similarly,

$$\frac{\left[\prod_j^{N_{local}} p_{swap.j}^{su:f} \right]^{f \rightarrow i}}{\left[\prod_j^{N_{local}} p_{swap.j}^{su:f} \right]^{i \rightarrow f}} = \prod_j \exp \left(\beta_{eff} \Delta E_{swap.j}^{su:f} \right). \quad (6.13)$$

Then using

$$\Delta E_{swap}^{su:state} = \sum_j \Delta E_{swap.j}^{su:state}, \quad (6.14)$$

the ratio of proposal probabilities, Eq. 6.9 can be rewritten,

$$\begin{aligned} \frac{p_{prop}^{f \rightarrow i}}{p_{prop}^{i \rightarrow f}} &= \prod_j \exp \left(\beta_{eff} \Delta E_{swap,j}^{su:i} \right) \times \prod_j \exp \left(\beta_{eff} \Delta E_{swap,j}^{su:f} \right) \\ &= \exp \left(\beta_{eff} \left[\Delta E_{swap}^{su:i} + \Delta E_{swap}^{su:f} \right] \right). \end{aligned} \quad (6.15)$$

Thus, substituting the expressions for the Boltzmann probability ratio, Eq. 6.8, and the move proposal probability ratio, Eq. 6.15, into the detailed balance Eq. 6.6,

$$\frac{p_{acc}^{i \rightarrow f}}{p_{acc}^{f \rightarrow i}} = \exp \left[-\beta \Delta E_{su} - (\beta - \beta_{eff}) \left(\Delta E_{swap}^{su:i} + \Delta E_{swap}^{su:f} \right) \right]. \quad (6.16)$$

Then, neglecting energy fluctuations and letting $T_{eff} \rightarrow T$ from above, which allows $\beta \Delta E_{su}$ to remain unchanged relative to the solute move without local solvent relaxation, if

$$-(\beta - \beta_{eff}) \left(\Delta E_{swap}^{su:i} + \Delta E_{swap}^{su:f} \right) > 0, \quad (6.17)$$

then allowing solvent relaxation moves increases the move acceptance probability relative to no solvent relaxation moves.

CHAPTER 7

SHAPE AND NUCLEATION DYNAMICS OF NEMATIC TACTOIDS IN CONTACT WITH WETTABLE COLLOIDS

This chapter reproduces material from a draft of a manuscript being prepared for submission. That work was in collaboration with Kimberly Weirich, Eli Alster, Thomas A. Witten, Margaret L. Gardel, Kinjal Dasbiswas, and Suriyanarayanan Vaikuntanathan. I am the first author of the paper, and contributed to both simulation and theory portions of the work.

Recent experiments have shown how nematically-ordered tactoid shaped actin droplets can be reorganized and divided by the action of myosin molecular motors. In this paper, we consider how similar morphological changes can potentially be achieved under equilibrium conditions. Using simulations, both atomistic and continuum, and a phenomenological model, we explore how the nucleation dynamics, shape changes, and the final steady state of a nematic tactoid droplet can be modified by interactions with model adhesive colloids that mimic a myosin motor cluster. Our results provide a prescription for the minimal conditions required to stabilize tactoid reorganization and division in an equilibrium colloidal-nematic setting.

7.1 Introduction

Nematic liquid crystals comprise rod-like particles that mutually align along a preferred direction (known as the “director”) to create a fluid phase with long-range orientational order. The elastic energy cost of deviating from such preferred directions of alignment can be leveraged to sculpt complex free energy landscapes that direct the self-assembly of colloids and nanoparticles [126]. There is renewed interest in liquid crystals because biological matter, including collections of elongated cells [127, 128], and the structural components of their cytoskeleton – biopolymer filaments such as actin and microtubules [129, 130] –

exhibit nematic order including active matter phases with large-scale flows [131]. Recently, collections of short, rod-like actin filaments have been shown to form nematic droplets with a characteristic elongated tactoid shape [132], that can incorporate the molecular motor myosin to undergo self-organization and shape transformation [5]. In particular, these nematic droplets of actin can be divided into two equal-sized droplets by clusters of myosin motors that robustly self-organize to the droplet midplane [5]. The authors suggest that the droplet deformation can be understood to arise from local realignments of actin filaments by motor activity that cluster the motors and the surrounding actin into an “aster”-like arrangement [133] with actin filaments radiating outwards from the central myosin cluster. Specifically, they model the cluster of motors as an adhesive (“wettable”), spherical colloidal particle that imposes a perpendicular alignment (“anchoring”) on the actin nematic at its surface [134]. In this work, we investigate with equilibrium computer simulations the probable intermediate and final minimal energy configurations of such a nematic droplet wetting a colloidal surface, illuminating the assumptions implicit in, and placing strong constraints on, the model presented in Ref. [5].

We construct a minimal model colloid that mimics the geometric constraints imposed by and interactions due to the aster-like object created by the action of the molecular motors. We are interested in probing how our model colloids affect the shapes of nematic droplets within simple equilibrium simulation models that capture the general properties of nematic order without focusing on the detailed molecular features of the actomyosin system, including myosin motor activity. Our choice to neglect motor activity is consistent with the observed suppression of active mechanical forces as individual myosin filaments cluster [130]. We apply two frameworks – the Gay-Berne (or GB) molecular dynamics model [135] as well as a coarse-grained continuum phase field model – to gain insight into the nucleation and shape changes of tactoids in contact with colloids.

Here, we report the observation of long-lived dynamic states in which multiple tactoids

associate with our model aster-like colloid. Ultimately, these states are found to be unstable within the simple, equilibrium models we explore. The ground state is a single tactoid associated at its pole with a colloid, resembling prior experimental observations in molecular liquid crystal droplets [136, 137, 138, 139]. We identify the feature – the formation of a molecularly-thin layer of nematic fluid on the colloid surface – that undermines the long-term stability of the two-tactoid state explored in Weirich et al. [5]. We then generalize the phenomenological model from that work to identify possible conditions under which a two-tactoid state may be stable in the absence of active forces. Together, our results provide constraints on the class of detailed equilibrium molecular models that can be used to obtain the stable two-tactoid states that resemble those observed in Ref. [5].

The rest of the paper is organized as follows. We first describe the results of our GB molecular dynamics simulations in Section 7.2. In Section 7.3 we report the results of our continuum phase field simulations, which both complement and extend beyond our MD results. Finally, we outline a phenomenological model that captures some of our simulation observations in Section 7.4, discuss the implications of our work, and predict the set of additional features a model would need to allow for stable, divided tactoids.

7.2 Colloid-tactoid interactions in a molecular dynamics model

7.2.1 *Nematic tactoids associate with aster-like colloids*

Inspired by experimental and theoretical studies on actomyosin clusters [5, 140], in which myosin motors are thought to organize actin filaments into an “aster”-like (or radial) cluster, we study how an aster-like colloid interacts with tactoid droplets. To simulate rod-like particles in molecular dynamics, we use the GB model [135], implemented in the LAMMPS software package [109, 141]. GB particles are elongated ellipsoids with an aspect ratio κ and with aspherical well depths which are described by a parameter κ' of similar form to

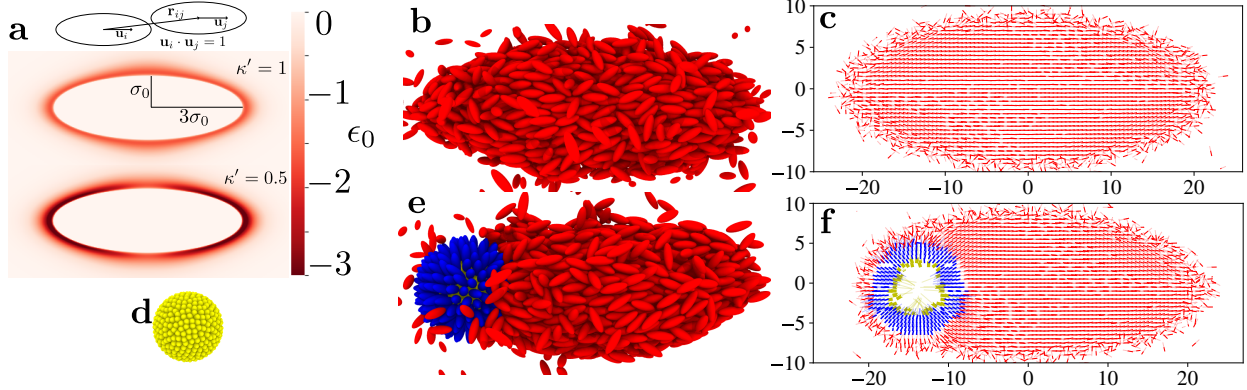


Figure 7.1: Tactoids form from GB rods in molecular dynamics simulations with $T = 0.55$, $N = 2000$, $L = 75\sigma_0$, and can interact favorably with colloids. **(a)** Schematic for the Gay-Berne model potential for our choices of parameters when rods are parallel. Rods interact based on their distance and orientation, and depend on two aspherical parameters: κ , the aspect ratio, here set to $\kappa = 3$, and κ' , the ratio of aspherical well depths (see Appendix 7.5.1 for more details). The attractive part of the potentials for two rods with the same orientation and $\kappa' = 1$ and $\kappa' = 0.5$ are plotted in the second and third portion of this subfigure. The end-end well depth is deeper by a factor of two for $\kappa' = 0.5$. Tactoids formed from rods with $\kappa' = 1$ are the subject of Section 7.2.1, while Section 7.2.2 studies $\kappa' = 0.5$. **(b)** A snapshot from a molecular dynamics trajectory of a tactoid with $\kappa' = 1$ from a simulation without a colloid. **(c)** The director field of the cross-section at the midplane of a tactoid extracted from a molecular dynamics trajectory of a tactoid with $\kappa' = 1$ from a simulation without a colloid. **(d)** A snapshot of the homeotropic colloid used in molecular dynamics simulation. This colloid is composed of 421 fixed rods with their centers placed on the surface of a sphere with radius $3.5\sigma_0$ and is the colloid we will use in the MD portion of this work. **(e)** A snapshot from molecular dynamics simulation of a Gay-Berne tactoid with $\kappa' = 1$ associated with a homeotropic colloid. In this snapshot, the immobilized colloid is colored yellow, the molecularly-thin splayed nematic layer adsorbed to the colloid is colored blue, and all other rods are colored red. **(f)** The director field extracted from a molecular dynamics trajectory of a tactoid with $\kappa' = 1$ associated with a homeotropic colloid. Same color scheme as (e). All MD snapshots are visualized using Ovito [2].

the aspect ratio; a schematic of the GB potential for parallel rods is shown in Fig. 7.1(a). $\kappa' < 1$ represents stronger end-to-end interactions between the rod-like particles. Our choice to use the GB model was informed by its demonstrated ability to form tactoid droplets with appropriate choice of parameters [142, 143, 4] and its simplicity, which makes it a good minimal model. We provide details on our choice of two parameterizations and simulation protocol in the Appendix Section 7.5.1 but briefly, we use an aspect ratio $\kappa = 3$, and ratio of aspherical well-depths $\kappa' = 1$, which have been well studied in the literature and which ensures that nematic-vapor coexistence occupies a significant region of phase space [142]. Later, in Section 7.2.2 we vary κ' . Our basic simulation protocol is to start with a vapor of GB rods and to progressively quench the temperature until the system is well within the nematic-vapor coexistence region where tactoids do indeed form, see Fig. 7.1(b,c). There, we show a snapshot from simulation and the director field of the cross-section at the midplane of a tactoid averaged over a trajectory, respectively. Tactoids formed with the parameters discussed now have internal dynamics similar to a liquid.

Our model for a colloid, discussed in more detail in Appendix Section 7.5.2, is a set of GB particles whose centers of mass are fixed upon the surface of a sphere and are oriented radially, see Fig. 7.1(d). These particles are not allowed to move or rotate during the simulation. This model colloid was constructed to mimic the aster-like arrangement of actin filaments caused by molecular motor action. Throughout this work we report results for a colloid composed of $N_c = 421$ fixed particles that share the fluid pair potential and whose centers of mass are located on a sphere of radius $R_c = 3.5\sigma_0$ (with σ_0 the short-axis particle diameter). We tested other colloid sizes and surface densities as well, choosing this size to limit the scale of simulations.

When a vapor of $N = 2000$ rods is quenched in the presence of the colloid described above, first a single-molecule-thick layer of radially-oriented rods forms upon the surface of the colloid. In Fig. 7.1(d,e), the rods making up the colloid are colored yellow and those

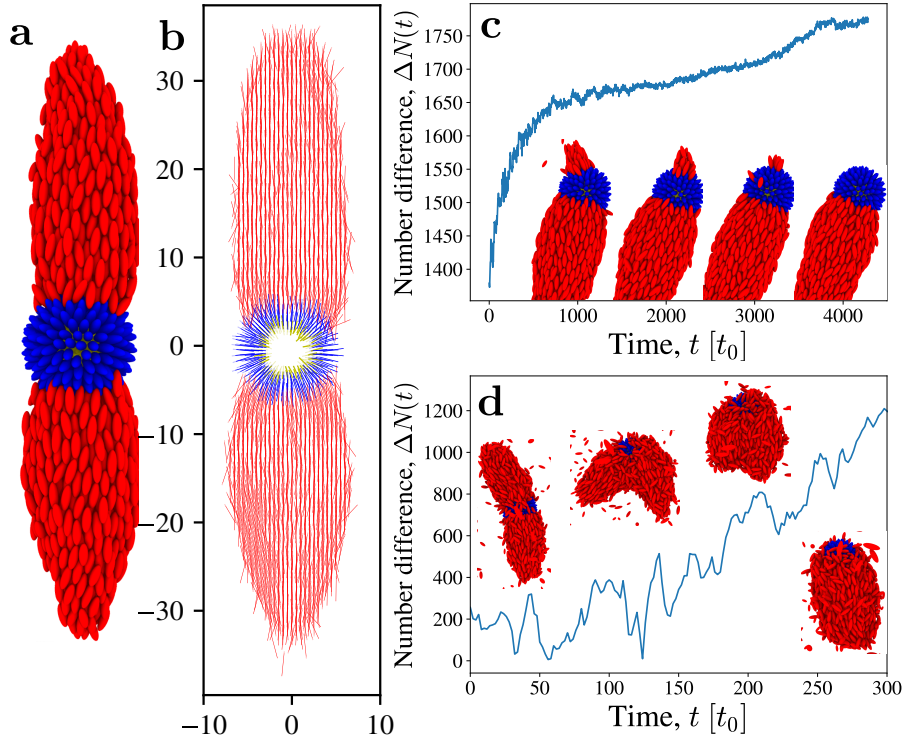


Figure 7.2: In MD, two tactoids may nucleate on the surface of a homeotropic colloid with appropriate choice of parameters, but they are an unstable configuration that gradually evolves into a more stable one.. Here, $N = 2000$, $L = 96\sigma_0$. **(a)** A snapshot from a molecular dynamics trajectory of two roughly equal-sized tactoids with $\kappa' = 0.5$ associated with a homeotropic colloid. In this snapshot, the immobilized colloid is colored yellow, the thin, splayed nematic monolayer adsorbed to the colloid is colored blue, and all other rods are colored red. **(b)** The director field of the cross-section at the midplane of two tactoids extracted from a molecular dynamics trajectory of two roughly equal-sized tactoids with $\kappa' = 0.5$ associated with a homeotropic colloid. Same color scheme as (a). **(c)** Time series data showing the difference in particle number between two tactoids for $\kappa' = 0.5$. This particular nucleation event resulted in two unequally-sized tactoids at around $t \sim 1000t_0$. The smaller tactoid slowly loses particles, which are incorporated into the larger tactoid, until it disappears, leaving only the larger tactoid. Snapshots are representative of the decay of smaller tactoid. Same color scheme as (a). **(d)** Time series data showing the difference in particle number between two tactoids, demonstrating the instability of two tactoids for $\kappa' = 1$. The configuration shown in (a) was used as the initial condition, and κ' was changed to 1 at $t = 0$. The tactoids equilibrate to their new interaction potential, and then begin to translate on the colloid surface, before combining after around $300t_0$. Snapshots show a selection of the configurations as the two tactoids combine. Note the rapid timescale relative to (c). Same color scheme as (a). All MD snapshots are visualized using Ovito [2].

comprising the splayed nematic layer are blue. After the association of the thin splayed nematic layer, a tactoid nucleates upon its surface, leading to a state like shown in Fig. 7.1(e,f), showing a snapshot and the ensemble average director field, respectively. Here, the tactoid has some freedom to translate on the colloid-nematic layer surface, but the rough nature of the surface does not allow unimpeded translation (by “translation” we refer to a movement of the interface between the tactoid and the colloid and a corresponding reorientation of the entire tactoid to remain pointing radially outward from the colloid). As has been observed in past studies [136, 137, 138, 139], the tactoid wets the colloid at one end. For an aster-like colloid, such a configuration minimizes the perturbation to the tactoid director field at the cost of reducing the area of the colloid that is wet by the droplet. As suggested by Weirich et al. [5], the area that is wet can be increased by dividing the tactoid droplet into two, at the cost of increasing the surface and elastic energies. In our simple GB model, with $\kappa' = 1$, for tactoid droplets with liquid-like internal dynamics, the adhesive wetting interaction between the colloid and the tactoid is too small to induce such states – and our ability to increase the wetting interaction strength is limited by the emergence of a molecularly-thin layer. Next, by reducing κ' , we increase the strength of the attractive interaction between the ends of all GB rods, both fluid and colloid, at constant temperature, in order to: (i), increase the wetting interaction even between the nematic layer and the tactoids, and (ii), slow down the internal dynamics of the tactoid droplets to better examine intermediate, unstable nucleation states.

7.2.2 Strong interactions and slow dynamics can lead to transient nucleation of multiple tactoids on a single colloid

To examine intermediate states in the nucleation of tactoids on colloids, and to increase the wetting adhesion strength even in the presence of a molecularly-thin splayed nematic layer, we increase the well depth of the end-end interaction of rods by a factor of two (ie. set $\kappa' = 0.5$) while leaving temperature constant (see Appendix 7.5.1 for details and Fig. 7.1(a)

for heatmap plot of potential between parallel rods). Tactoids nucleate similarly to the previous parameter set where $\kappa' = 1$, but these have a longer aspect ratio and much slower, more rigid internal dynamics. The tactoids diffuse much more slowly on the surface of the colloid as well. For these parameters, as the initial tactoid grows on the colloid surface, a second tactoid may nucleate as well. This is observed to occur the large majority of the time with $N = 2000$ fluid rods in a cubic simulation box with sides $L = 96\sigma_0$ and can occasionally lead to two highly symmetric tactoids, see Fig. 7.2(a,b) for snapshot and director field.

Two tactoid states, here, are able to exist on a single colloid not due to a lower free energy, but instead due to the slow internal dynamics and colloid surface translation, relative to the tactoid nucleation and growth timescales. On rare occasions, two fully formed tactoids with $\kappa' = 0.5$ were observed to combine by translation on the surface of the colloid. Further, when the tactoids greatly differ in size, the smaller one can be seen to be slowly losing particles until eventually only a single tactoid remains, see Fig. 7.2(c) for a particular trajectory particle number time series and snapshots over time. These observations taken together lead us to hypothesize that the ground state for the system in both parameter sets is a single tactoid, and that the two tactoid state is either metastable or is unstable, but with a slow decay to the ground state due to the slow relaxation dynamics of the droplets.

The instability of the divided drop configuration is more apparent for simulations done with the $\kappa' = 1$ parameter set. In Fig. 7.2(e), we describe simulations in which we take the divided configuration shown in Fig. 7.2(a), generated with the “slow-dynamics” $\kappa' = 0.5$, and change to the “faster” $\kappa' = 1$ parameter set. As shown in the time series in Fig. 7.2(d), the two tactoids rapidly translate on the surface and combine into one (compare timescales with Fig. 7.2(c)). It is clear, then, that for the “fast” $\kappa' = 1$ parameters, one tactoid is a lower free energy state than two tactoids.

We note that in order to accurately characterize the stability or metastability of various configurations, it is necessary to compute the free energy of the tactoid-colloid system as

a function of order parameters such as the interdroplet angle or the sizes of the various nucleating tactoids. Such free energy calculations are beyond the scope of this work. Rather, in Section. 7.3, we explore using continuum simulations the various potential intermediate and ground states of the tactoid-colloid systems. While the continuum simulations will fail to resolve fine molecular details, they allow us to probe phenomena on longer time and length scales.

7.3 Tactoids and homeotropic colloids in a continuum phase field simulation

The long length and time scale behavior of the nematic phase, particularly its elastic distortions and defect structures, is traditionally described by the Landau-de Gennes theory [134] which is also used to model nematic-colloid interactions [144]. In contrast with the bulk, nematic droplets resulting from aggregation of rod-like particles have free interfaces that separate the high density nematic from the lower density isotropic or vapor phases. In fact, the alignment of the rods at the droplet interface is a key feature that determines the characteristic tactoid shape [145]. Thus, a continuum description of the nucleation of tactoids and their shape dynamics should include a density in addition to the nematic order parameter. Here, we adapt a phase field model developed for lyotropic liquid crystals [146, 147] to study the interaction between a nematic tactoid droplet and an adhesive colloid. To mimic the binding and arrangement of actin filaments into an aster geometry by a myosin cluster, the model colloid must perform two roles, namely it must interact favorably with the nematic fluid and it must also provide a tendency for the nematic field at its surface to orient radially, also referred to as homeotropic anchoring [126]. We now describe how to construct such a tactoid-colloid model.

Since a nematic tactoid involves bend and splay but not necessarily twist of the director field, we use a 2D description, that is equivalent to looking at a planar section of the full

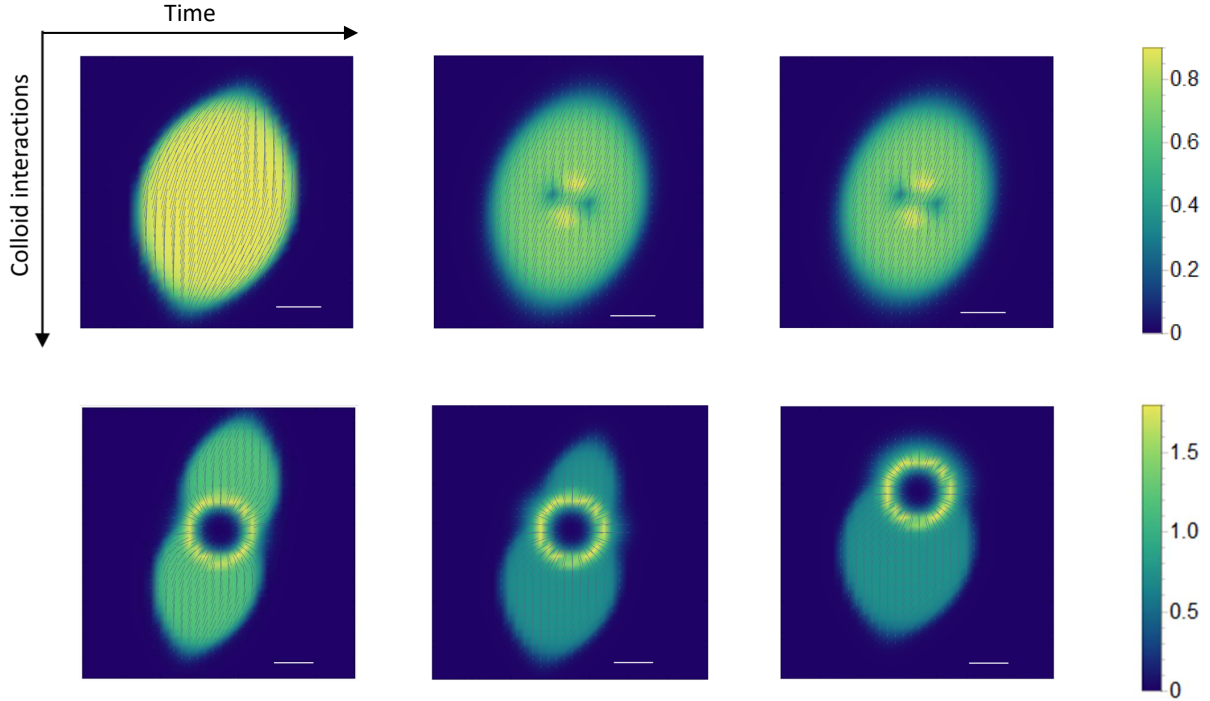


Figure 7.3: Each image shows the nematic density field, \mathbf{Q} from continuum simulation for the same tactoid droplet, in contact with a colloid that imposes homeotropic (radial) anchoring, at different times during the relaxation of the droplet shape. The tactoid is initialized with the colloid at its center. Colors show the magnitude, S , and lines show the director, \mathbf{n} , of the nematic field. The scale bars in each case correspond to 10 grid points. The simulation box is 120×120 , only part of which is shown here. The top panel shows the situation for a smaller colloid (radius, $r_0 = 4$) which has weaker interactions with the nematic. Here, topological defects, seen as regions of depleted nematic order on either side of the colloid, are induced but the overall tactoid shape is undeformed. This resembles the well-known situation for colloids in bulk nematic. The bottom panel shows the situation for the larger colloid size (radius, $r_0 = 8$) with stronger interactions with the nematic. Here, the tactoid shape can be significantly deformed, resulting in an intermediate divided state. The two divided droplets ultimately coalesce forming a single tactoid with the colloid at its pole. The colloid is not shown directly but corresponds to the region of depleted nematic density at the center of the tactoid where the colloid displaces the fluid.

3D tactoid. The 2D nematic tensor, defined as $Q_{ij} = S(n_i n_j - \frac{1}{2}\delta_{ij})$, contains the scalar magnitude, $S = \frac{1}{2}\text{Tr } \mathbf{Q}^2$, and the director, \mathbf{n} , or direction of the local nematic order. The model free energy coupling the 2D, nondimensionalized density, $\psi(\mathbf{x})$, and nematic, $Q_{ij}(\mathbf{x})$, order parameter fields is written as [147],

$$\begin{aligned} F = \int d^2x & \left[-\frac{v_2}{2}\psi^2 - \frac{v_3}{3}\psi^3 + \frac{v_4}{4}\psi^4 + \frac{B}{2}(\nabla\psi)^2 \right. \\ & + \frac{1}{4}Q_{ij}^2(C\psi(\psi - 1) + D_1) + \frac{S_1}{16}Q_{ij}^2Q_{kl}^2 \\ & \left. + \frac{D_2}{2}(\partial_k Q_{ik})^2 + B_3\partial_k\psi\partial_i Q_{ik} \right] \end{aligned} \quad (7.1)$$

which includes the usual Landau free energy terms describing a first order transition in ψ , the usual Landau-de Gennes terms describing a nematic transition in \mathbf{Q} , and two terms coupling ψ and \mathbf{Q} . The first of these represents the transition to nematic order at the high density phase. The second with the coefficient B_3 describes a “soft” anchoring or alignment of the nematic director with the external droplet boundary. We work in the “equal constant” approximation, where the energy cost of bend and splay are both included in the term with prefactor D_2 . Note that while this free energy is for a phenomenological phase field model that describes the nematic-isotropic (or nematic-vapor) interface and can nucleate tactoids for suitable parameters, it can also be derived by coarse-graining molecular interactions [146, 147].

The relaxation dynamics of the tactoids are specified by the standard dynamics for the conserved scalar density field (Model B),

$$\partial_t\psi(\mathbf{x}, t) = \tau_Q\nabla^2\frac{\delta F}{\delta\psi(\mathbf{x}, t)}, \quad (7.2)$$

and the nematic order parameter field (Model A),

$$\partial_t Q_{ij}(\mathbf{x}, t) = -\tau_\psi\frac{\delta F}{\delta Q_{ij}(\mathbf{x}, t)}. \quad (7.3)$$

where τ_Q and τ_ψ are characteristic time scales of the phase dynamics of the nematic and density fields. These dynamical equations in suitably nondimensionalized form are solved on a grid with periodic boundary conditions using a pseudospectral scheme with the XMDS software package [148]. For appropriate choice of parameter values, we see tactoids nucleate from a random initial configuration. See Appendix Section 7.5.8 for details of implementation and table of parameter values used to form tactoids.

To study the effect of a colloid on the droplet structure, we model the spherical colloid by an additional static field, $\phi(x, y) = \frac{1}{2} \left[1 + \tanh\left(r_0 - \sqrt{(x - x_0)^2 + (y - y_0)^2}\right)/t_0 \right]$, where (x_0, y_0) and r_0 specify the center and radius or size of the colloid respectively, and t_0 is the thickness of the diffuse interface of the colloid as is usual in a phase field model. We incorporate the colloid surface-droplet interaction, anchoring and adhesion, in the free energy. The perpendicular or radial anchoring of the droplet nematic director at the colloid surface can be included in the free energy as the energy cost of deviating away from a preferred value of the nematic tensor at the colloid [149, 150], which is proportional to $(Q_{ij} - Q_{ij}^0)^2$. This preferred value of $Q_{ij}^0 \propto \partial_i \phi \partial_j \phi$ is normal to the colloid in direction (given by $\partial_i \phi$). The corresponding free energy term is then defined as $\frac{1}{2} B_4 \partial_i \phi Q_{ij} \partial_j \phi$. This term is also an effective surface adhesion since the nematic order, \mathbf{Q} , and correspondingly, the density, ψ , are enhanced at the colloid surface because of it. An additional term, $W\phi\psi$, leads to exclusion of nematic fluid from the bulk of the colloid, and helps speed up the simulation dynamics.

We initialize the colloid at the center of a tactoid generated in our continuum model, analogous to the situation for actomyosin tactoids reported in Ref. [5], and let the droplet-colloid relax towards its minimal energy state. Fig. 7.3 shows the tactoid nematic order parameter at different instants during the course of the simulation for two different sizes of colloid in contact with the same initial tactoid droplet. We find that the relaxation pathway depends significantly upon the relative sizes of the tactoid droplet and the colloid,

with a larger perturbation of the droplet shape seen for larger colloids as expected. In fact for larger colloids, the droplet is initially divided into a two-tactoid state as seen in our MD results, Fig. 7.2, and as predicted by the model presented in Ref. [5]. For a smaller colloid, the tactoid surface is unperturbed, but a quadrupolar topological defect forms near the colloid surface, see Fig. 7.3, upper panel. This resembles the expected situation for a disk colloid in a 2D bulk nematic [151]. For a fixed tactoid size, increasing the size of the colloid placed into the droplet pushes the defects closer to the nematic-vapor interface, until that interface bows inward toward the defects. The defects can thereby be expelled from the droplet, leading to a state with two tactoid droplets associated with opposite sides of the colloid, see Fig. 7.3, lower panel. Defect-induced division of a different model nematic droplet was also predicted theoretically in Ref. [152]. At longer times however, the two divided droplets coalesce by diffusing around the colloid and form a single tactoid with the colloid at its pole. This equilibrium state of the system is thus consistent with what is seen in the MD simulations, and is expected for a single tactoid associated with a colloid with strong homeotropic anchoring at its surface. These observations connect traditional studies of colloid-induced defects in bulk nematics and the deformation and division of tactoid droplets by colloids.

7.4 Discussion

In Ref. [5], it was proposed that the observed division of actin tactoidal droplets by clusters of myosin motors could be explained by modeling the myosin cluster as a spherical colloid that aligns the actin nematic around it. Specifically, we used the bipolar model for tactoid structure in conjunction with anchoring and adhesion of the actin fluid phase at the myosin cluster interface, to show that a divided droplet state may be energetically favored over a single whole droplet, because it can then increase its area of contact with the colloid. In this paper, we have demonstrated that colloidal interactions may indeed deform nematic droplets,

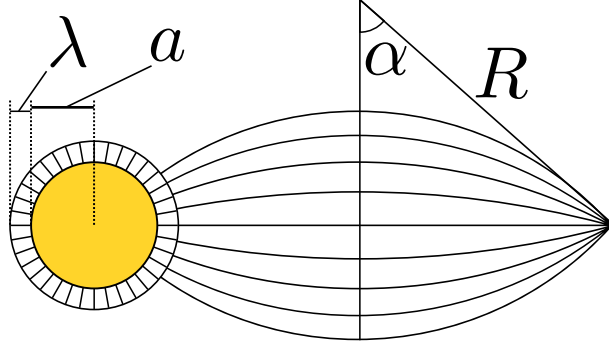


Figure 7.4: A schematic of a tactoid with size and shape parameters: the radius, R , and the tip angle α , as defined in Ref. [3]. This tactoid is associated at its pole with a colloid of radius a that imposes homeotropic (radial) alignment on the fluid it is in contact with. The colloid surface may be covered by a thin splayed nematic layer of thickness λ of the order of the rod length.

and that even if droplet division is not stable, the ultimate coalescence of two droplets may be slowed down through attractive and radially aligning interactions with a colloid. Specifically, we have reported the observation, within a molecular dynamics and a continuum simulation framework, of dynamic states in which multiple tactoids can be associated with a single colloid. We have shown that these multi-droplet states are unstable within both these models. We find instead that the ground state is a single, whole tactoid associated at its pole with a colloid. In the present section, we generalize the phenomenological model of Weirich et al. [5] to explain our results. We then discuss our results in a broader context, and describe a set of minimal extensions beyond the simulation models used here that may allow for the realization of stably divided tactoids. We note, as in Ref. [5], that in the limit that the tactoids are much large than the colloids, the driving forces for tactoid recombination overwhelm any driving forces for tactoid division, since the latter simply depends on colloid size. Hence, in the limit of thermodynamically large tactoid drops, we anticipate that the stable ground state is simply corresponds to single undivided droplet.

A feature not included in the model droplet-colloid free energy in Weirich et al. [5] was the possible formation of a molecularly-thin splayed nematic layer on the surface of the colloid, which was a recurring feature observed in our GB and continuum simulations. Instead, it

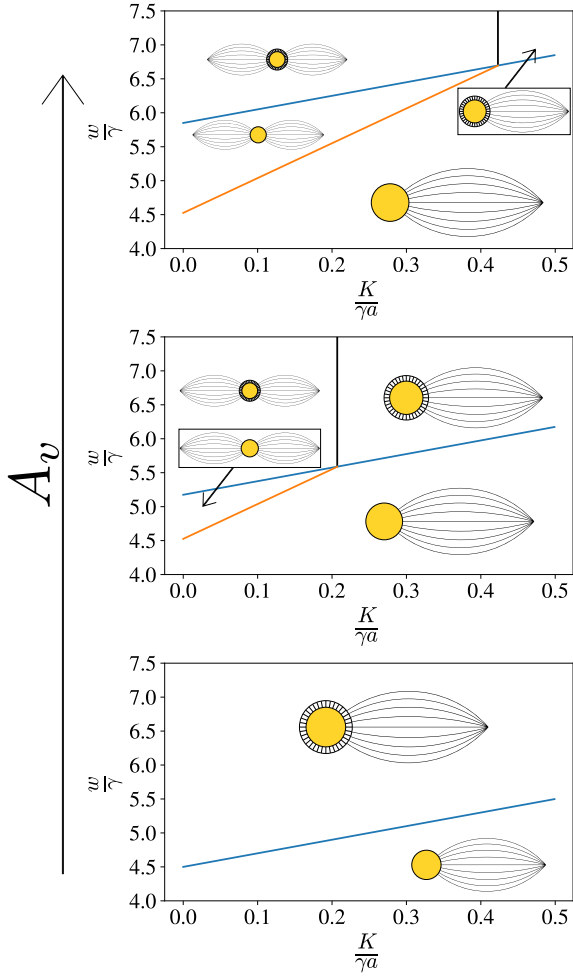


Figure 7.5: Set of phase diagrams for fixed $\lambda = 0.5a$ and total tactoid volume $V_t = 2 \times 4\pi a^3/3$ with increasing $A_v = 1.0, 1.3, 1.6$. The blue line in each plot divides the region where a molecularly-thin layer forms (above the blue line, where $F_l < 0$ or $w > \epsilon$) from the region where no molecularly-thin layer forms (below, where $F_l > 0$ or $w < \epsilon$). Above the blue line, the formation of the molecularly-thin layer replaces the wetting parameter, w , with a weaker “effective wetting” of ϵ , since, upon tactoid association, the area fraction covered by the tactoid, f_t is subtracted from the total area fraction, f_l of the molecularly-thin layer in the energy penalty term, ie. $f_l \rightarrow f_l - f_t$, see discussion in main text or Appendix Section 7.5.9. Thus, the possible existence of the thin nematic layer provides an upper bound on w . For a colloid to support (meta)stable divided tactoids, the nematic-vapor interfacial anchoring energy parameter, A_v , must be above a certain value. Here, multiple tactoids are a local free energy minimum between the orange and blue lines, for which there is no wetting layer, or above the blue line and to the left of the black line, for which multiple tactoids associate with the wetting layer. However, when A_v is small enough, there is no “divided” region, as seen in the phase diagram for $A_v = 1.0$.

was assumed there the orientation of the director field was strongly anchored parallel to the droplet nematic-vapor interface, ie. strictly planar anchoring as in the bipolar tactoid model [145, 3]. However, such a nematic layer is incompatible with the simultaneous strong planar anchoring at the droplet-vapor interface and strong homeotropic anchoring at the droplet-colloid interface. Relaxing the strong nematic-vapor anchoring constraint allows us to constrain the conditions under which two or more droplets can stably associate with the colloid without coalescing. Thus, motivated to more closely describe the conditions of our present simulation models, we relax this strong nematic-vapor anchoring constraint, by adding an anchoring energy cost, per unit area, at the nematic-vapor interface to the overall free energy $\sim \gamma A_v (\mathbf{v} \cdot \mathbf{n})^2$, with γ the surface tension, A_v the dimensionless nematic-vapor anchoring coefficient, \mathbf{v} the interface normal and \mathbf{n} the director [149, 145]. We can then write down the free energy cost of a molecularly-thin splayed nematic layer adhered to the surface of the colloid. Specifically, we consider a layer of radially-directed nematic of thickness λ covering a dimensionless fraction f_l of the surface area of a colloid of radius a , see schematic in Fig. 7.4. The free energy can be written as

$$F_l = \left[-w + \frac{4K}{a} \frac{\lambda}{a} + \gamma (1 + A_v) \left(1 + \frac{\lambda}{a} \right)^2 \right] f_l 4\pi a^2 \\ = [-w + \epsilon] f_l 4\pi a^2, \quad (7.4)$$

with w the strength of the adhesive colloid-nematic wetting interaction, and K the Frank elastic constant in the one-constant approximation (see Appendix 7.5.9 for derivation). In the second line, we have grouped the energy penalties associated with the splayed nematic layer into a single term, explicitly, $\epsilon \equiv \frac{4K}{a} \frac{\lambda}{a} + \gamma (1 + A_v) \left(1 + \frac{\lambda}{a} \right)^2$. Thus, a thin splayed nematic layer is favored to form when the adhesive wetting interaction strength between the colloid and the nematic becomes larger than the penalties associated with the stressed nematic state (ie. splay elastic energy, surface energy, and anchoring energy): $w > \epsilon$.

It follows that there are two possibilities we need to consider: the association of one or

more tactoids with the colloid in the absence ($F_l > 0$), or the presence ($F_l < 0$) of a thin splayed nematic layer. The phase diagrams plotted in Fig. 7.5, show how the anchoring parameter A_v can be used to change the boundary between these two possible regimes. The first case resembles the model described in Ref. [5], but with an upper bound, $w < \epsilon$, and corresponds to the region below the blue line in each phase diagram. In that model, multi-tactoid states, which increase the colloid-nematic wetting area, can be stabilized when w is larger than a critical value dependent on the elastic and surface energy penalties, $w > w^*$; this regime appears as the region above the orange line in the top two phase diagrams. However, the addition of the upper bound $w < \epsilon$ restricts the size of the stable two-tactoid region. When $w^* > \epsilon$, as is the case for the bottom phase diagram in Fig. 7.5, there is no stably-divided region, which may explain why (meta)stable two-tactoid states are not realized in the present simulations. In the second case, when $w > \epsilon$ (above the blue line), a thin nematic layer will form, and tactoid(s) will associate with that layer on the surface of the colloid. There is a free energetic benefit for such an association, but it is not determined by w . Instead, the dimensionless area fraction of the thin nematic layer covered by the tactoid, f_t , is subtracted from the total nematic layer area fraction in the energy penalty term, leading to a net energy benefit of $-\epsilon f_t 4\pi a^2$ upon association. Thus, the possibility of a thin splayed nematic layer sets an upper bound on the “effective adhesive wetting” felt by the colloid, potentially eliminating the two-tactoid stable state. Though the nematic layer appears to be a limiting factor in the minimal GB model we study here, we predict that a model which affords control over A_v will allow elimination of the thin nematic layer and access to the stably divided regime. One simple modification to the present GB model is the addition of another particle type that penalizes nematic-vapor interfaces with rods oriented normal to the interface. Such a model could be adapted from work by Moreno-Razo et al. [153].

In summary, the work in this paper shows how colloidal interactions can be used to modify

the shape and dynamics of associating liquid crystal tactoid droplets. Our motivation for these studies was the experimentally observed reorganization of actin tactoidal droplets by clusters of myosin motors in Ref. [5]. Our work identifies possible (effectively) equilibrium mechanisms for this observed reorganization and places strong molecular constraints on the model presented in Ref. [5]. While active forces resulting from myosin sliding actin filaments may be crucial for the observations in Ref. [5], our studies suggest that engineering suitable liquid crystal-colloidal interactions may also result in nematic droplet deformation.

Both biopolymeric and molecular liquid crystals are candidate materials for future experimental investigations of the deformation of nematic droplets by colloids. Passive beads, as opposed to clusters of motors, can be functionalized to bind actin filaments in aligned orientation [154], which under suitable conditions can nucleate tactoids [132]. Incorporating strongly homeotropic colloids into molecular liquid crystal droplets may also show the formation of nematic defects in the droplets, and their ultimate expulsion leading to deformation of the droplet interface. However such colloidal inclusions need to have strong affinity for the host liquid crystal in order to be incorporated into the bulk of the droplet, while simultaneously ensuring that the interfacial tension of such liquid crystals is low enough to allow for such deformation. While using the elastic distortion of liquid crystal solvents is a standard route to colloidal self-assembly [155], we point out here the possibility of changing droplet shape and nucleation dynamics using colloids. The resulting tunability of droplet morphology may have possible applications in interfacial materials[156].

7.5 Appendix

7.5.1 *Gay-Berne parameterization and simulation protocol*

We study tactoids using molecular dynamics for two parameter sets. Readers are referred to the literature for an introduction of the details of the Gay-Berne model [141]. In both

parameter sets, we study uniaxial rods of aspect ratio $\kappa = \sigma_{ee}/\sigma_{ss} = 3$, with σ_{ee} the particle length and σ_{ss} the width, in units of the fundamental length scale σ_0 . The exponent parameters are set to the original parameterization used by Gay and Berne [135], $\mu = 2$ and $\nu = 1$, which remains a common choice in the literature. The other anisotropic parameter in the uniaxial GB model is the ratio of anisotropic well depths $\kappa' = \epsilon_{ss}/\epsilon_{ee}$, with ϵ_{ss} the well depth for rods interacting side-to-side and ϵ_{ee} the well depth for rods interacting end-to-end. We choose $\kappa' = 1$ and $\kappa' = 0.5$ (for which $\epsilon_{ee} = 2\epsilon_0$ with ϵ_0 the fundamental energy scale) due to the easier access afforded to the nematic-vapor coexistence portion of the phase diagram for $\kappa' \leq 1$ [143]. See Fig. 7.1(a) for a visualization of the GB potential for parallel rods with our choices of parameters. The simulation time step was set to $0.002t_0$, with t_0 the natural time scale.

Using the parameters mentioned above with $\kappa' = 1$, and simulation periodic cube with sides of length $L = 75\sigma_0$, a single tactoid quickly forms from a vapor quenched to $T = 0.55$, see Fig. 7.1(b). Specifically, the initial condition is an optional colloid and a simple cubic lattice of fluid rods which are vaporized to temperature $T = 2.55$ for 10^5 to 5×10^5 time steps and then quenched in steps of $\Delta T = -0.2$ every 10^5 timesteps until reaching $T = 0.55$, see Fig. 7.6. The director field, which measures the average local orientation of rods in the droplet is extracted, as detailed in the Appendix, and is plotted in Fig. 7.1(c). The tactoid displays liquid ordering, with particles diffusing throughout the droplet. In contrast, the parameter set with $\kappa' = 0.5$ leads to tactoids which are much more rigidly ordered and have significantly slower diffusion of particles throughout the droplets, as well as much lower vapor pressure.

7.5.2 Implementing a homeotropic colloid in molecular dynamics

We are interested in how a colloid with homeotropic boundary conditions interacts with tactoid droplets. The colloid must perform two roles, namely inducing wetting, and maintaining

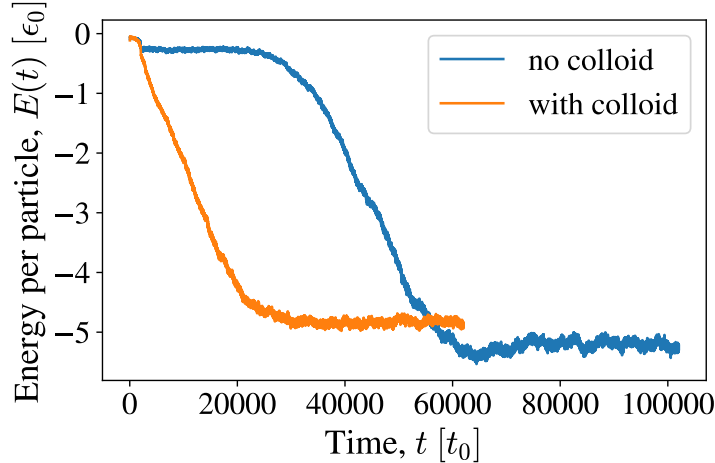


Figure 7.6: Energy time series for $\kappa' = 1$, $N = 2000$, $L = 75\sigma_0$ trajectories without (blue) and with (orange) a colloid demonstrate that equilibrium is reached within a reasonable simulation time. Initial condition is a simple cubic lattice of rods that is vaporized to a gas at $T = 2.55$. The temperature is then slowly quenched over time (over the first $1000t_0$) until reaching its final value of $T = 0.55$.

the boundary condition, or anchoring. We initially used a sphere with a strong wetting interaction with the fluid rods. This approach has met with success in a past study when applied in a bulk nematic, as rod packing led to homeotropic anchoring [157]. We found that a spherical colloid indeed interacted with a tactoid, but with very weak anchoring regardless of the wetting strength. Further, it was clear that multiple tactoids would not be able to nucleate on the surface of the colloid, as the first tactoid to nucleate was free to translate on the colloid surface and absorb any other nuclei that might form. To improve the strength of the anchoring as well as to add a barrier to translation on the surface, we turned to another model for the colloid. In this model, we place a fixed set of GB particles upon the surface of a sphere and orient them so that they point radially outward, see Fig. 7.1(d). We outline the details of the procedure to create the colloid below in Appendix Section 7.5.3. Throughout this work we use a colloid composed of 421 fixed particles whose centers of mass are located on a sphere of radius $3.5\sigma_0$ unless otherwise noted.

7.5.3 Finding the near-optimal spacing of points on a sphere

We implement a homeotropic colloid by constructing a fixed set of GB rods with center of masses upon the surface of a sphere and which are oriented radially, see Fig. 7.1(c). We first find the positions of a set of such rods by imagining them as points which we would like to place – separated from each other as much as possible – on the surface of a sphere. We initialize a given number of points forming the colloid, N_s , randomly placed upon the surface of a sphere of radius R_s . We estimate the optimal spacing of particles on the surface of the sphere using a well-known iterative approach where we imagine each particle to be an ion interacting with each other “ion” according to a repulsive Coulomb $1/r$ interaction. We take Monte Carlo steps, iteratively selecting a particle at random as well as a random move on the surface of the sphere, and then evaluating the probability of accepting the move using the standard Metropolis rule:

$$p_{acc}(\Delta E) = \min [1, \exp(-\beta \Delta E)], \quad (7.5)$$

with β the effective inverse thermal energy, a parameter that increases through the iterative procedure, and ΔE is the change in energy due to the proposed move, explicitly, for a move of particle i ,

$$\Delta E = \sum_{j \neq i}^{N_s} 1/r_{ij}^{(proposed)} - 1/r_{ij}^{(old)}, \quad (7.6)$$

with $r_{ij} = |\mathbf{r}_j - \mathbf{r}_i|$. After a sufficient number of Monte Carlo steps, we are left with a good estimate of the configuration of particles that maximizes the space between each particle. We take this set of positions as the positions of the rods which make up the colloid, and for each particle, orient it such that it points radially outward. The result of this procedure for a choice of $N_s = 421$ and $R_s = 3.5$ is shown in Fig. 7.1(d). To maintain its rigid form throughout the simulation, we simply neglect to time integrate the rods which make up the colloid. Particles in the fluid will interact with the colloid, but the colloid will not translate

or change shape as a result.

7.5.4 Aspect ratio of GB tactoids

As shown by Ref. [145], the aspect ratio of an elongated, bipolar tactoid is expected to decrease with the volume of the tactoid (or particle number). This is shown on dimensional arguments and confirmed using more detailed theory [145, 158], as well as in numerous experiments [159, 160, 161, 162, 163, 164, 165]. The intuition is that the surface energy increases with the surface area of the tactoid, $\sim R_i^2$, while the elastic energy increases as the volume of the tactoid times the squared curvature, ie. as $\sim R_i$. Thus, for large tactoids, the surface energy dominates, leading to a more spherical – smaller aspect ratio – tactoid. To our knowledge, only one study shows tactoid aspect ratio increasing with volume, a study of GB molecular dynamics model tactoids [4]. We confirm their result, finding that the aspect ratio increases with the volume of the tactoid, see Fig. 7.7. This may suggest that larger droplets with higher number of rods might be required to see agreement with the continuum tactoid model. Because of this discrepancy, we must be cautious attempting to map continuum theory directly to the MD results with GB particles.

7.5.5 Extraction of director field

We extract the director field from MD simulations to gain insight into the perturbation that a colloid induces in the director field. From a time series of trajectory frames, we first exclude any particles that are within the fixed colloid (assuming the particular trajectory has a colloid). Next, we exclude any gas particles by using the following procedure. We compute the adjacency matrix for the system, whose matrix elements are defined as

$$A_{ij} = \exp\left(-\frac{r_{ij}^2}{2\sigma^2}\right), \quad (7.7)$$

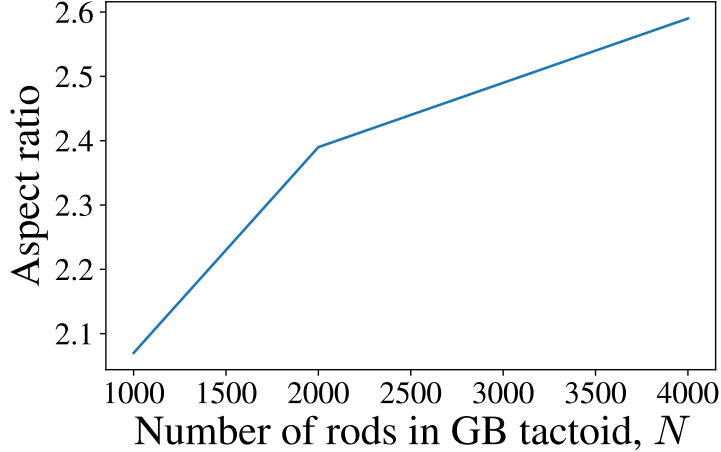


Figure 7.7: Measured aspect ratio for tactoids formed from rods with $\kappa' = 1$ as a function of particle number. This trend of tactoids formed in the GB model, first reported by [4], is opposite of that predicted by theory and observed in experiment.

with $r_{ij} = |\mathbf{r}_j - \mathbf{r}_i|$ and σ a parameter chosen to make sums over columns $d_i = \sum_j A_{ij}$ large when particle i is in the tactoid droplet and small when in the gas phase (we use $\sigma = 0.5$). This is a similar metric to coordination number. We cluster $(d_i + c)^{-1}$ values about two means using the standard k -means clustering algorithm, with c a small constant (here, 0.01). Clustering with $\sim 1/d_i$ was found to give much better results than directly clustering d_i . The particles in the cluster corresponding to small d_i values are in the gas phase, and are excluded. Having removed the gas and (optional) colloid particles, we compute the center of mass of the remaining particles, which make up the tactoid droplet. We set the origin to be the center of mass, compute the inertia tensor, and rotate to the inertia tensor eigenvector basis as the natural basis of the droplet. We divide space into discrete bins, and within these bins compute our order parameter of interest: local density or local director field.

The director field is computed within a bin by first computing the nematic tensor order parameter $\mathbf{Q}(\mathbf{r})$, specifically,

$$Q_{ij}(\mathbf{r}) = \frac{1}{2N_b(\mathbf{r})} \sum_k^{N_b(\mathbf{r})} 3u_i^{(k)}(\mathbf{r})u_j^{(k)}(\mathbf{r}) - \delta_{ij}, \quad (7.8)$$

where the sum runs over all particles within a bin, $N_b(\mathbf{r})$, and $u_i^{(k)}(\mathbf{r})$ is the i -component of particle k 's orientation vector. The director $\mathbf{n}(\mathbf{r})$ is the eigenvector corresponding to the largest eigenvalue of $\mathbf{Q}(\mathbf{r})$, and the largest eigenvalue is the magnitude of the ordering, $S(\mathbf{r})$.

Fig. 7.1(b) shows a cross-section of the director field of a tactoid with $N = 2000$ particles in a simulation box of size $L = 75\sigma_0$. Qualitatively, it is clear that the tactoid is not homogeneous, as the director field tends to mimic the curvature of the nematic-vapor interface. However, the tactoid is also not purely bipolar (compare with the schematic in Fig. 7.5(a)). Fig. 7.1(d) shows a cross-section of the director field of a $N = 2000$ tactoid in a box of size $L = 75\sigma_0$ associated with a colloid at its lower tip. It can be seen that the colloid templates homeotropic order within a local region, and that even beyond that local region, the director field is perturbed relative to the tactoid without an associated colloid.

7.5.6 Measurement of surface tension

The surface tension is extracted using the standard pressure tensor method [166, 167, 168, 169] using a slab geometry. The slab is oriented with its normal in the z -direction, and the important functions, namely density, the normal and tangential terms of the pressure tensor, and the integral of their difference, are plotted in Fig. 7.8. The surface tension is one half the value of the integral (since there are two interfaces); for $\kappa' = 1$, we find the surface tension is $\gamma \sim 0.4\epsilon_0/\sigma_0^2$, which is within expectations from the literature [168].

7.5.7 Large tactoids partially engulf aster-like colloids

We greatly increase the number of fluid rods to study whether a large tactoid engulfs the colloid. We are particularly interested in whether defects will appear within the director field of the engulfing tactoid, as the avoidance of defects may cause the divided tactoid configurations, as we discuss in Section 7.3. If the number of fluid particles is large, nucleation will proceed as normal, but the tactoid will continue to grow in length – the tactoid width

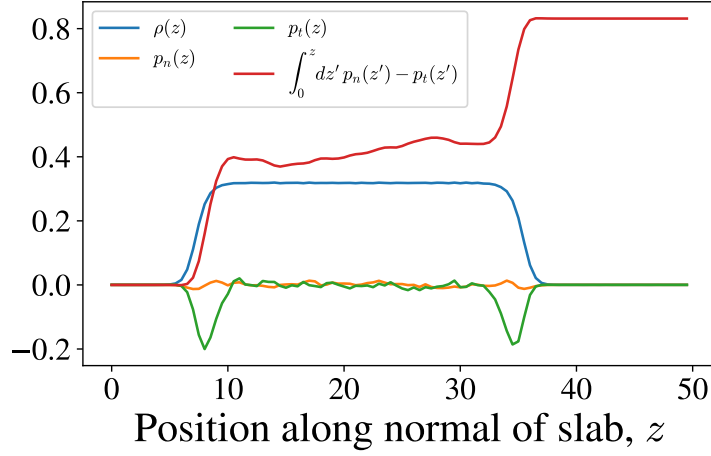


Figure 7.8: Surface tension measurement of $\kappa' = 1$ nematic-vapor slab at $T = 0.55$ via the pressure tensor. The surface tension is one half the value of the integral at the largest value of z , ie. $\gamma \sim 0.4\epsilon_0/\sigma_0^2$ (since there are two interfaces).

appears to be bounded by the size of the colloid. If growth continues, the tip of tactoid eventually decouples from the colloid, and the colloid is partially engulfed by the tactoid, see Fig. 7.9(a) which uses the slow parameter set, $N = 20200$ fluid rods, and box size of $L = 200\sigma_0$.

The change to a partially-engulfing tactoid can be understood by considering the interplay of a few interactions and entropy. The interactions at play can be thought of as the favorable wetting interaction between the fluid particles and the colloid, the colloid surface anchoring, and the perturbation of the tactoid director field induced by the colloid. For small particle number, tactoids associate with a colloid by binding one end to the colloid, leading to a minimal perturbation to the tactoid director field. As the number of fluid particles increases, the end of the tactoid eventually dissociates and it partially engulfs the colloid. In this way, the tactoid can increase in width, reducing the nematic-vapor surface energy, and a larger portion of the colloid can be wet by the tactoid at the cost of a high local colloid surface anchoring energy and an increased deformation of the tactoid director field. The tactoid gains an entropy benefit in this configuration as well, because in addition to translation on

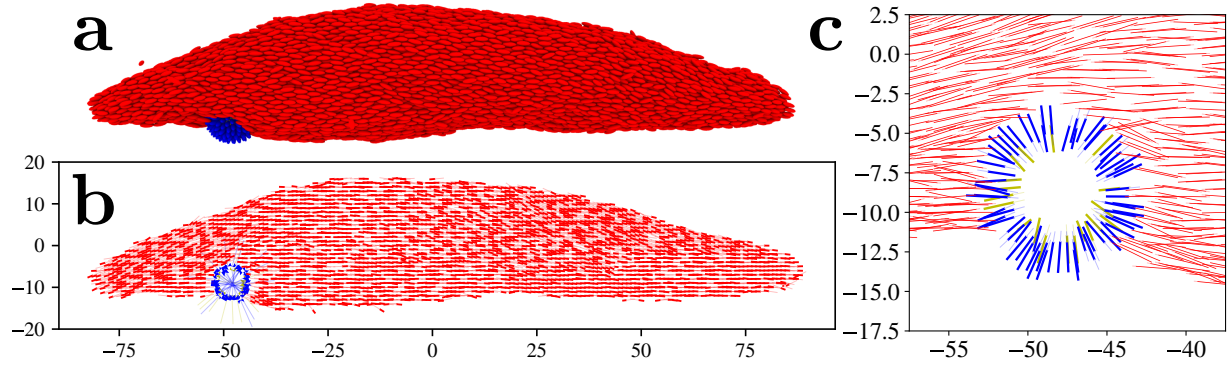


Figure 7.9: Large tactoids partially engulf small colloids because perturbations to the director field are costly and are minimized by expelling the colloid to the tactoid surface. Here, $T = 0.55$, $\kappa' = 0.5$, $N = 20200$, and $L = 200\sigma_0$. **(a)** A snapshot from simulation showing a large “tactoid” partially engulfing a homeotropic colloid. Partial wetting and dissociation of the tactoid end from the colloid is only observed when the resultant tactoid is much larger than the colloid. The “tactoid” has a distinct crescent shape. In this snapshot, the immobilized colloid is colored yellow, the thin, splayed nematic layer adsorbed to the colloid is colored blue, and all other rods are colored red. **(b)** The director field extracted from simulation showing partial colloid wetting. The director field is not apparently deflected beyond the wetting layer of the colloid. Same color scheme as (a). **(c)** Zoom-in near the colloid, showing the director field beyond the splayed nematic layer is only slightly perturbed. Same color scheme as (a). All MD snapshots are visualized using Ovito [2].

the surface of the colloid, the tactoid can now also change the position of association with the colloid.

The director field corresponding to the partial wetting snapshot is shown in Fig. 7.9(b). If the molecularly-thin splayed nematic layer, shown in blue, is considered a part of the fluid, the configuration looks to contain a partial “Saturn-ring” defect after the single-molecule splayed nematic layer [170, 44, 171], see Fig. 7.9(c) for a close-up of the director field near the molecularly-thin layer. Traditionally, defects occur a further distance from the surface of the colloid, for example, in Ref. [44], the defect is predicted to occur at a distance of $\sim 1.17a$, with a the colloid radius, or between 10 and 100 rod lengths from the surface of the water droplet colloid in that work. Here, however, the colloid radius is of the same order as the rod length. It may be the case that only one molecular layer appears since a is so much small.

7.5.8 Details of continuum simulations

The dynamical equations for the density, ψ , and the 2D nematic order parameter, \mathbf{Q} , are evolved in time by explicit Euler stepping on a 120×120 grid with periodic boundary conditions using the pseudospectral method implemented on the numerical package XMDS [148]. The parameters are chosen to be in the nematic-vapor coexistence region of the phase diagram so that tactoids can nucleate, and so that the interface thicknesses are comparable to a few gridpoints. After observing tactoid nucleation and coarsening, a large tactoid is selected and initialized with a colloid at its center. Strong anchoring at the tactoid-colloid interface is enforced with a high value of the parameter B_4 .

7.5.9 Derivation of free energy of a thin splayed nematic layer on the surface of an adhesive colloid

The free energy contributions to the splayed nematic layer of thickness λ adhered to the surface of a colloid of radius a , as pictured in Fig. 7.4, will be from the favorable nematic-

Parameter	Value
v_2	0.5
v_3	0.5
v_4	2.0
B	0.5
C	5.0
D_1	0.01
S_1	2.0
D_2	1.0
B_3	0.7
τ_ψ	1.0
τ_Q	10.0

Parameter	small	large
r_0	4.0	8.0
t_0	1.0	1.0
B_4	5.0	20.0
W	1.0	1.0

Table 7.1: Parameters used in the continuum simulations. The first set of parameters are for generating tactoids. The second set of parameters represent the size of the colloid and the strength of the tactoid-colloid interactions for the two cases shown in Fig. 7.3. There, we show the evolution of tactoid nematic field for two different colloids: a small colloid with weak surface interaction (upper panel) to contrast with a large colloid with strong surface interaction (lower panel). All lengths are in units of grid size, whereas energy and timescales are in arbitrary units.

colloid wetting, the elastic cost due to a splayed nematic, the surface tension cost of the nematic-vapor interface, and the anchoring energy cost due to the deviation of the director field from planar at the nematic-vapor interface. Say that the thin layer covers an area fraction of the colloid f_l which has a value 0 if none of the surface is covered and 1 if the entire surface is covered.

Proceeding term-by-term, the adhesive interaction between the colloid and the thin layer will be

$$\begin{aligned}
 F_l^{(w)} &= -w f_l a^2 \int dS 1 \\
 &= -w f_l 4\pi a^2,
 \end{aligned} \tag{7.9}$$

where the coefficient w is a parameter that controls the strength of the adhesive, or wetting, interaction and where dS is the integral over the solid angle of the surface. The elastic cost of a splayed nematic can be computed

$$\begin{aligned} F_l^{(K)} &= K f_l \int dS \int_a^{a+\lambda} dr r^2 (\nabla \cdot \mathbf{n})^2 \\ &= 4K\lambda f_l 4\pi, \end{aligned} \quad (7.10)$$

where K is the Frank elastic constant in the one-constant approximation, and \mathbf{n} is the director field of the thin nematic layer, here $\mathbf{n} = \hat{\mathbf{r}}$. The surface energy due to the nematic-vapor interface for a sphere of radius $a + \lambda$ is simply

$$\begin{aligned} F_l^{(\gamma)} &= \gamma f_l (a + \lambda)^2 \int dS 1 \\ &= \gamma f_l 4\pi (a + \lambda)^2, \end{aligned} \quad (7.11)$$

with γ the nematic-vapor surface tension. Finally, the nematic-vapor anchoring energy cost is easily computed since we require that $\mathbf{n} = \hat{\mathbf{r}}$ at the interface:

$$\begin{aligned} F_l^{(A_v)} &= \gamma A_v f_l (a + \lambda)^2 \int dS (\mathbf{v} \cdot \mathbf{n})^2 \\ &= \gamma A_v f_l 4\pi (a + \lambda)^2, \end{aligned} \quad (7.12)$$

where $\mathbf{v} = \hat{\mathbf{r}}$ is the surface normal.

We can write the free energy of the thin nematic layer as

$$\begin{aligned} F_l &= F_l^{(w)} + F_l^{(K)} + F_l^{(\gamma)} + F_l^{(A_v)} \\ &= \left[-w + \frac{4K}{a} \frac{\lambda}{a} + \gamma (1 + A_v) \left(1 + \frac{\lambda}{a} \right)^2 \right] f_l 4\pi a^2 \\ &= [-w + \epsilon] f_l 4\pi a^2. \end{aligned} \quad (7.13)$$

If a tactoid associates with the colloid-layer system where the entire colloid is covered by

the thin nematic layer, the free energy benefit of association now comes from the reduction of the area fraction of the energy penalty $\epsilon f_l 4\pi a^2$. This can be seen from a few considerations. First, consider the schematic in Fig. 7.10, which shows that, for a thin splayed nematic layer, relative to the curvature of the associating tactoid, the area fraction, f_t , that the tactoid occupies on the colloid surface and the area fraction the tactoid occupies on the thin splayed nematic layer surface are equivalent. We can think of the tactoid as cutting out a cone shaped region from the nematic layer when it associates with the colloid-layer system. Then, the association of the tactoid will not change the area of the colloid which is wet by a nematic (whether from the tactoid or from the thin splayed nematic layer), so the benefit from the adhesive wetting energy $-wf_l 4\pi a^2 = -w(f_l - f_t) 4\pi a^2 - wf_t 4\pi a^2$ remains constant. On the other hand, the energy penalty due to the wetting layer has its area fraction modified, from its pre-tactoid value of f_l to a post-tactoid value of $f_l - f_t$. Thus, the association of a tactoid leads to an energy benefit of $-\epsilon f_t 4\pi a^2$, making ϵ take the role of an “effective wetting”.

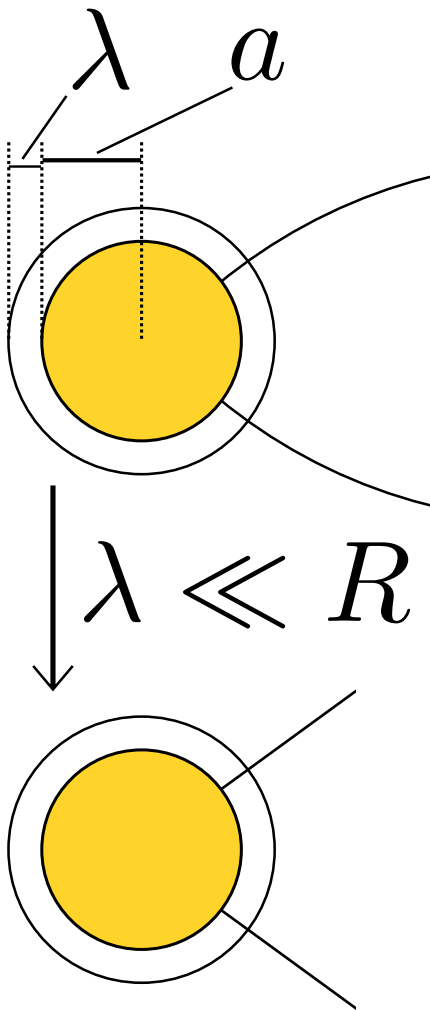


Figure 7.10: When the thickness of the thin splayed nematic layer, λ is small relative to the radius of curvature of the associated tactoid, R , the curvature can be neglected and the intersection between the tactoid and the nematic layer can be treated as a portion of a cone. The requirement that the tactoid director lines be radial at the colloid surface, discussed in Ref. [5], then sets the “cone tactoid” radial at both colloid and splayed nematic layer surfaces and means that the tactoid covers an equal area fraction of both surfaces.

CHAPTER 8

CONCLUSIONS AND OUTLOOK

In this work, we present a set of studies of soft matter systems and their interactions with colloids of various kinds. First, we set the stage in Chapter 2 by introducing some important concepts about ionic fluids, which are the subject of the majority of this work, discussing the foundational Debye-Hückel and DLVO theories, introducing linear response, and detailing some modern approaches which attempt to account for correlations in fluids with high ionic strength. We present work done on the charge-frustrated Ising model in Chapter 3, demonstrating that a simple, coarse-grained model can capture some of the important features of an ionic fluid with low or high ionic strength. Next, we detail two studies of nanocrystal colloids within molten salts and ionic liquids in Chapters 4 and 5, which together establish the stability of these colloids and provide evidence for a stabilizing mechanism: the charge density oscillations induced within the fluid by the colloid surfaces. Chapter 6 is concerned with some generalizations of the charge-frustrated Ising model, and is still work in progress. Finally, switching focus away from ionic fluids, Chapter 7 studies the interactions between nematic liquid crystal fluids formed from rod-like particles and colloids which have a preference for a fixed, radial alignment of rods at their surface.

Specifically, our work has helped to establish some of the minimal requirements for a coarse-grained model of ionic fluids. The frustrated Ising model captures the DH regime as well as the regime change to the post-DH regime where charge correlations become oscillatory. The FI model compares well with other theoretical techniques, but is unable to reproduce recent experimental measurements [21, 22, 23], indicating that there is still work to be done. We extended ideas from the FI model to explain colloidal stability in molten salt and ionic liquid solvent environments, and again, though the model was able to bring some explanatory efficacy to bear, there were results that we were unable to explain, see Chapter 5 in particular. Our tactoid-colloid model advanced the state of knowledge about the minimal

features required to stabilize shape changes such as splitting of nematic droplets. Thus, we provide a possible route to droplet division at equilibrium, as well as some insights into the possible roles of motor activity in the experimental actin-myosin system [5].

Broadly, our work has advanced understanding of soft matter colloidal systems with potential applications to nanoscopic self-assembly and materials design. Mean field theories and linear response have been standard techniques for many years, but we were surprised at how applicable they were in systems where strong interactions between particles occur, such as ionic liquids or molten salts. Mean field theory tends to be most applicable when the range of interactions is long relative to the size or spacing of particles, since that means that on the shorter, particle length scale, small deviations in position do not significantly change the net force that a particle feels, and hence, local regions can be effectively coarse-grained [166]. Though electrostatic interactions are long-ranged, the damped oscillatory configurations that result mean that small deviations in position can indeed lead to large changes in the net force felt by a particle. Despite this apparent contradiction to standard mean field intuition, our work has demonstrated that mean field ideas can indeed account for a significant portion of the phenomenology of these solvent systems. Our work is thus encouraging for studies of other soft matter systems. We also apply similarly minimal modeling tools to study how colloids influence the shape of associated nematic tactoid droplets, and, again, demonstrate how simple tools can provide insights into complicated soft matter systems. The long-range nature of both of these systems yields to astonishingly simple minimal models. Our work paints a hopeful picture that the minimal models required to describe a wide range of complicated soft matter systems might also be fairly simple.

There are always more questions to address. Two major unanswered questions may be related to the applicability of linear response and mean field theory. In Chapter 5, nanocrystal-induced correlations were of longer range than bulk correlations. Perhaps along the same lines, is the mysterious screening length scaling observed experimentally in surface

force apparatus, and other, experiments [21, 22, 1, 23]. One difference between these two sets of unexplained results is that the correlations induced by the colloids [26] are oscillatory, while the interaction between plate-like surfaces appears to be monotonic [21, 22, 1]. Nonetheless, until these results are understood, we cannot claim to fully understand the physics of colloids and surfaces within the dense ionic fluid state. On a different subject, we would also like to pursue the generalizations of the FI model discussed in Chapter 6. An additional interesting possibility that might be worth studying that emerged from our study of cubic NCs is that of kinetic trapping. Kinetically stable gel phase or superlattice structures might be created using cubic or other highly-faceted NCs. In future work, our charge-frustrated Ising code might be used to efficiently study the structures formed by many NCs. If we indications are found that these phases exist, they can then be studied with more sophisticated molecular dynamics techniques without having to canvas a large region of phase space. It would be exciting to provide predictions as to the kinds of NCs and physical parameters which might produce these phases, which could be used to help guide our experimental collaborators along new exciting and productive avenues of investigation.

With regards to our studies of the colloid-tactoid system, this work has only just begun. We have provided a prediction as to how an equilibrium colloid-nematic droplet system might lead to stably divided droplets, but this needs to be confirmed in simulation and in experiment. A number of past studies have documented the assembly of colloids by nematic droplets [153, 137, 139], but now with the shape changes induced within droplets by colloids as an additional tool, it might be interesting to explore what sort of exotic self-assembly configurations could be achieved by combining these two research directions. Of course, the original experimental work we were inspired by included motor activity as an important element [5], and so it will be exciting to see how our predictions of stability relate to microscopic models which include motor activity. Another element which we have not considered in any great detail is the treatment of crosslinkers. In the experiments, actin

rods are transiently bound by filamin crosslinkers, and we model this in an extremely coarse manner with a pairwise attractive well potential. It is likely that the a more realistic picture is significantly more complicated [172]. Finally, it is surprising that our model of rod-like particles, with an aspect ratio at least an order of magnitude smaller than the experimental actin rods, gave even qualitatively similar results to the experimental system. It will be intriguing to see what changes occur with particles of a more reasonable aspect ratio.

In summary, we have applied simple, minimal theory models to complicated soft matter systems involving the self-assembly of colloids. We have used simulation methods, molecular and coarse-grained, to extend beyond the reach of our mean field, linear response models and to incorporate the effects of fluctuations. Though we were able to capture a surprising amount of the phenomenology with our minimal models, there are some aspects of the experiments which we aspired to explain, such as long-range monotonic screening in ionic fluids [21, 22, 23], which our models were unable to account for. Considering that more detailed models cannot explain these aspects either, this is exciting rather than disheartening. Our minimal models capture the same essential physics described by the state of the art in the field – but there are hints of new, as yet unexplained physics. It is our hope that the minimal models developed here can serve as a foundation for the next generation of models that will be able to explain these new physics and advance human understanding.

CHAPTER 9

APPENDIX

9.1 The Euler–Lagrange equation

9.1.1 One-dimensional case

The calculus of variations is a very powerful and wide-ranging formalism. Here, we derive a small set of tools from that formalism which will come in handy. A more detailed derivation can be found in Weinstock’s text [173].

The problem is to extremize the integral of a functional, defined as

$$F = \int dx f [x, y(x), \partial_x y(x)], \quad (9.1)$$

with respect to variations in $y(x)$. Another statement of the problem is to find the optimal $y^*(x)$ that extremizes F . To do so, we consider how variations in $y(x)$ lead to variations in F with the goal of writing down an expression for the functional derivative $\frac{\delta F}{\delta y(x)}$. With the functional derivative in hand, F is easily extremized by setting $\frac{\delta F}{\delta y(x)} = 0$, which will lead us to an expression for $y^*(x)$ that extremizes F . Here, we assume that the extremum is a minimum of F , but this condition can be confirmed by requiring that the second functional derivative $\frac{\delta^2 F}{\delta y(x)^2} > 0$.

The variation of F can be written

$$\begin{aligned} \delta F &= \int dx \delta f [x, y(x), \partial_x y(x)] \\ &= \int dx \frac{\delta f}{\delta y(x)} \delta y(x) + \frac{\delta f}{\delta (\partial_x y(x))} \delta (\partial_x y(x)). \end{aligned} \quad (9.2)$$

A key element of the procedure occurs here in the second line where the function $y(x)$ and its first derivative $\partial_x y(x)$ are allowed to vary independently. To acquire the functional

derivative, we need to perform an integration by parts to move the derivative in the second term. Specifically,

$$\begin{aligned}\delta F &= \int dx \frac{\delta f}{\delta y(x)} \delta y(x) + \frac{\delta f}{\delta (\partial_x y(x))} \delta (\partial_x y(x)) \\ &= \int dx \frac{\delta f}{\delta y(x)} \delta y(x) - \partial_x \left(\frac{\delta f}{\delta (\partial_x y(x))} \right) \delta y(x) \\ &\quad + \left[\frac{\delta f}{\delta (\partial_x y(x))} \delta y(x) \right]_x,\end{aligned}\tag{9.3}$$

where the final term is evaluated over the end points of the integration, and can often be neglected. Neglecting it for now, the expression for the functional derivative is

$$\frac{\delta F}{\delta y(x)} = \frac{\delta f}{\delta y(x)} - \partial_x \left(\frac{\delta f}{\delta (\partial_x y(x))} \right),\tag{9.4}$$

which can be set to 0 to extremize the functional F : this is known as the Euler–Lagrange equation. Solving will provide an expression for $y^*(x)$, which can be substituted into F to find the extremized value.

9.1.2 Three-dimensional case

In three dimensions, the Euler–Lagrange equation is evaluated much the same as in one dimension. If the integrand functional depends only on a radial function and gradients of that function, ie.

$$F = \int d^3r f [r, y(r), \nabla y(r)],\tag{9.5}$$

then the resulting expression for the functional derivative, neglecting the surface term, is simply

$$\frac{\delta F}{\delta y(r)} = \frac{\delta f}{\delta y(r)} - \nabla \cdot \left(\frac{\delta f}{\delta (\nabla y(r))} \right).\tag{9.6}$$

9.2 Fourier transformation conventions

The d -dimensional Fourier transform of a function $f(\mathbf{r})$ is

$$\tilde{f}(\mathbf{k}) \equiv \mathcal{F}\{f(\mathbf{r})\}(\mathbf{k}) = \int_{\mathbb{R}^d} d^d r \exp(-i\mathbf{k} \cdot \mathbf{r}) f(\mathbf{r}), \quad (9.7)$$

with inverse

$$\mathcal{F}^{-1}\{\tilde{f}(\mathbf{k})\}(\mathbf{r}) = \int_{\mathbb{R}^d} \frac{d^d k}{(2\pi)^d} \exp(i\mathbf{k} \cdot \mathbf{r}) \tilde{f}(\mathbf{k}). \quad (9.8)$$

In three-dimensions, when $f(r)$ depends on only r (and not the vector-valued \mathbf{r}), the Fourier transform reduces to

$$\tilde{f}(k) = \mathcal{F}\{f(r)\}(k) = \frac{4\pi}{k} \int_0^\infty dr r \sin(kr) f(r), \quad (9.9)$$

and

$$\mathcal{F}^{-1}\{\tilde{f}(k)\}(r) = \frac{4\pi}{r} \int_0^\infty \frac{dk}{(2\pi)^3} k \sin(kr) \tilde{f}(k). \quad (9.10)$$

9.3 Inverse Fourier transformation of a k^4 order parameter correlation function

In this section we lay out the contour integrals required to inverse Fourier transform the Fourier form of order parameter correlation function, $\tilde{\phi}(k)$ to find the order parameter density $\phi(r)$. Consider an order parameter $\phi(r)$ for which we know the inverse order parameter correlation function has the form

$$\tilde{\phi}(k) = \frac{2\alpha k^2}{k^4 + 2\alpha k^2 + \beta}, \quad (9.11)$$

where α and β are constants with units length $^{-2}$ and length $^{-4}$ respectively. In particular, two cases will be considered since the poles have two regimes of interest. After finding the poles in these two cases, we walk through the integrals which lead to the final results,

$$\begin{aligned} \phi(r) &= 2\alpha \frac{1}{4\pi r} \left[\kappa^2 \exp(-\kappa r) - \frac{(\kappa^*)^4}{\kappa^2} \exp\left(-\frac{(\kappa^*)^2}{\kappa} r\right) \right] \Big/ \left[\kappa^2 - \frac{(\kappa^*)^4}{\kappa^2} \right] \\ &\xrightarrow{r \gg \kappa/(\kappa^*)^2} \frac{2\alpha}{1 - (\kappa^*/\kappa)^4} \frac{1}{4\pi r} \exp(-\kappa r), \end{aligned} \quad (9.12)$$

for $\alpha > \sqrt{\beta}$ (the “high temperature” case), and

$$\phi(r) = -\frac{2\alpha}{\sqrt{1 - \alpha^2/\beta}} \frac{1}{4\pi r} \exp(-\kappa r) \sin(\omega r + \theta), \quad (9.13)$$

for $-\sqrt{\beta} < \alpha < \sqrt{\beta}$ (the “low temperature” case). Constants are defined in the next sections, specifically, κ^* in Eq. 9.18, κ and ω in Eq. 9.19, and the phase factor θ in Eq. 9.33. There is another regime for $\alpha < -\sqrt{\beta}$ which has a truly long-ranged ordering (ie. no exponential decay), but we won’t explore this regime.

For the case of a one-dimensional order parameter, say due to a infinite plate-like bound-

ary condition, the high temperature Eq. 9.12 becomes

$$\phi(z) = \frac{\alpha}{4\kappa(1 - (\kappa^*/\kappa)^4)} \exp(-\kappa z), \quad (9.14)$$

and the low temperature Eq. 9.13 becomes

$$\phi(z) = \frac{\alpha}{4\kappa^*\sqrt{1 - \alpha^2/\beta}} \exp(-\kappa z) \cos(\omega z + \theta/2). \quad (9.15)$$

9.3.1 Poles for k^4 order parameter correlation function

The poles determine the contour integrals. The poles of $\tilde{\phi}(k)$ are found by solving the fourth-order equation

$$0 = k^4 + 2\alpha k^2 + \beta, \quad (9.16)$$

which leads to the four solutions

$$k^{\eta\lambda} = \eta\sqrt{\alpha}\sqrt{-1 + \lambda\sqrt{1 - \beta/\alpha^2}}, \quad (9.17)$$

where $\eta, \lambda \in \{\pm 1\}$.

The poles have different behavior in three different regimes, and we walk through two of those three. The first regime is for $\alpha^2 > \beta$, which we refer to sometimes as the “high temperature” regime (since $\alpha = \alpha(T)$ in the models we consider in this work). In the high temperature regime, the inner root is positive. When the inner square root becomes negative, the behavior of the poles upon variation of the parameters changes qualitatively, and this is the second, “low temperature” regime: $\alpha^2 < \beta$. Before discussing the high temperature regime, let’s define a constant

$$\kappa^* = \beta^{1/4}, \quad (9.18)$$

which, physically, is the inverse of the shortest decay length the system will achieve, and let

$$\begin{aligned}\kappa &= \mathbb{R}(k^{++}) \\ \omega &= \mathbb{I}(k^{++}).\end{aligned}\tag{9.19}$$

Poles in the “high temperature” regime

Letting $\alpha > \sqrt{\beta}$, the expression for the poles, Eq.9.17 can be specialized,

$$k^{\eta\lambda} = i\eta\sqrt{\alpha}\sqrt{1 - \lambda\sqrt{1 - \beta/\alpha^2}},\tag{9.20}$$

with the argument of the root now known to be ≥ 0 . Then the roots are known to be purely imaginary, ie. $\omega = 0$. Further, k^{++} and k^{+-} are in the upper half plane, with

$$\begin{aligned}k^{++} &< k^{+-}, \\ k^{++} &= -k^{-+}, \\ k^{+-} &= -k^{--},\end{aligned}\tag{9.21}$$

which will allow for significant simplifications. Finally,

$$(\kappa^*)^4 = (k^{++})^2 (k^{+-})^2,\tag{9.22}$$

which allows the rewriting of $\mathbb{I}(k^{+-}) = (\kappa^*)^2 / \kappa$. Note also that

$$\kappa \xrightarrow{\alpha \gg \sqrt{\beta}} 0,\tag{9.23}$$

which, with α varying as temperature means that, in the high temperature regime, the length scale $1/\kappa$ increases with temperature. Next, we outline the structure of the poles in the low temperature regime, which have some significant differences to the high temperature case

including an opposite dependence of $1/\kappa$ on temperature.

Poles in the “low temperature” regime

Now, let $0 < \alpha^2 < \beta$. The inner root becomes imaginary-valued, and it becomes convenient to write the argument of the square root in the expression for the poles, Eq. 9.17,

$$-1 + i\lambda\sqrt{\beta/\alpha^2 - 1} = \sqrt{\beta/\alpha^2} \exp \left[i \arctan \left(-\lambda\sqrt{\beta/\alpha^2 - 1} \right) \right], \quad (9.24)$$

which can be simplified, leading to an expression for the poles in this regime:

$$k^{\eta\lambda} = \kappa^* \eta \left[\sqrt{\frac{1}{2} \frac{\sqrt{\beta} - \alpha}{\sqrt{\beta}}} + i \lambda \sqrt{\frac{1}{2} \frac{\sqrt{\beta} + \alpha}{\sqrt{\beta}}} \right]. \quad (9.25)$$

In the low temperature regime, the relationships between poles are different. Specifically,

$$\begin{aligned} \mathbb{R}(k^{++}) &= \mathbb{R}(k^{+-}) \\ &= -\mathbb{R}(k^{-+}) \\ &= -\mathbb{R}(k^{--}), \\ \mathbb{I}(k^{++}) &= \mathbb{I}(k^{--}) \\ &= -\mathbb{I}(k^{+-}) \\ &= -\mathbb{I}(k^{-+}), \end{aligned} \quad (9.26)$$

where $\mathbb{R}(x)$ and $\mathbb{I}(x)$ are the real and imaginary parts of x , respectively. Note also that

$$(\kappa^*)^2 = \kappa^2 + \omega^2. \quad (9.27)$$

For the low temperature case, then, the length scale $1/\kappa = 1/\mathbb{I}(k^{++}) \sim \alpha^{-1/2}$ decreases with the root of temperature. Then the direction of change with temperature is opposite that

of the high temperature regime, for which an increase in temperature increases the length scale $1/\kappa$. These are all the relations we need, so let us proceed to the contour integrals.

9.3.2 Computing the inverse Fourier transform contour integrals

The residue theorem gives us a way to compute integrals over contours in the complex plane,

$$\oint_C dz \frac{f(z)}{(z-a)^{n+1}} = \frac{2\pi i}{n!} f^{(n)}(a), \quad (9.28)$$

where the integral is over a closed contour, C , which contains a pole at a of order $n+1$, and $f^{(n)}(a)$ is the n -the derivative of $f(z)$, which is then evaluated at the pole a . Here, we wish to compute a Fourier integral

$$\begin{aligned} \phi(r) &= \frac{4\pi}{r} \int_0^\infty \frac{dk}{(2\pi)^3} k \sin(kr) \frac{2\alpha k^2}{k^4 + 2\alpha k^2 + \beta} \\ &= \frac{\alpha}{(2\pi)^2 i r} \int_{-\infty}^\infty dk k^3 (e^{ikr} - e^{-ikr}) \left(\prod_j^4 (k - k_j) \right)^{-1}, \end{aligned} \quad (9.29)$$

with the k_j 's each a pole, and where in the second line, use has been made of the evenness of the integrand and the sin has been rewritten in exponential form. This integral can be computed by creating a contour that extends from $[-R, R]$ on the real axis and then follows a semicircular contour of radius R in the upper/lower half plane for the first/second exponential term respectively. Taking the limit $R \rightarrow \infty$ will send the values of the values of the integrals over the semicircle portion to identically 0, leaving the integral over the real line equal to the residues of the poles. Here, the result for the upper and lower half plane are identical, and so we only consider the integral over the upper half plane, accounting for the lower half plane by multiplying the result by 2.

Then,

$$\phi(r) = \frac{4\alpha}{4\pi r} \left[\sum_l^2 (k_l)^3 e^{ik_l r} \left(\prod_{j \neq l}^4 (k_l - k_j) \right)^{-1} \right], \quad (9.30)$$

where l runs over the poles in the upper half plane.

High temperature integral

For the high temperature regime, the two poles in the upper half plane are k^{++} and k^{+-} and so the product in the denominator of Eq. 9.30 can be written, for evaluation about the k^{++} pole, and using the identities Eq. 9.21

$$\begin{aligned} \prod_{j \neq ++}^4 (k^{++} - k_j) &= 2k^{++} \left[(k^{++})^2 - (k^{+-})^2 \right] \\ &= 4k^{++} \sqrt{1 - \beta/\alpha^2}, \end{aligned} \quad (9.31)$$

where in the second line the expressions for the high temperature poles, Eq. 9.20 has been used. Evaluating the corresponding product for the pole k^{+-} yields the same result with a minus sign, since the factor which was originally $k^{++} - k^{+-}$ switches sign. Plugging values into the result from the residue integration, Eq. 9.30, the order parameter correlation density is found to be Eq. 9.20 as promised (also using Eq. 9.22).

Low temperature integral

The poles in upper half plane for the low temperature regime are k^{++} and k^{--} . The k^{++} term denominator product can be found using the low temperature pole relations Eq. 9.26 and is found to be

$$\prod_{j \neq ++}^4 (k^{++} - k_j) = 8i\kappa\omega k^{++}. \quad (9.32)$$

Again, the product for the other pole, k^{--} , is simply -1 times the product Eq. 9.32. After some algebra, the final result, Eq. 9.25, is found, with

$$\theta = -\arctan \left(\sqrt{\beta/\alpha^2 - 1} \right) \quad (9.33)$$

the phase factor.

REFERENCES

- [1] Alpha A. Lee, Carla S. Perez-Martinez, Alexander M. Smith, and Susan Perkin. Scaling analysis of the screening length in concentrated electrolytes. *Phys. Rev. Lett.*, 119:026002, Jul 2017.
- [2] Alexander Stukowski. Visualization and analysis of atomistic simulation data with OVITO—the open visualization tool. *Modelling and Simulation in Materials Science and Engineering*, 18(1):015012, dec 2009.
- [3] A. V. Kaznacheev, M. M. Bogdanov, and S. A. Taraskin. The nature of prolate shape of tactoids in lyotropic inorganic liquid crystals. *Journal of Experimental and Theoretical Physics*, 95(1):57–63, Jul 2002.
- [4] Davide Vanzo, Matteo Ricci, Roberto Berardi, and Claudio Zannoni. Shape, chirality and internal order of freely suspended nematic nanodroplets. *Soft Matter*, 8:11790–11800, 2012.
- [5] Kimberly L. Weirich, Kinjal Dasbiswas, Thomas A. Witten, Suriyanarayanan Vaikuntanathan, and Margaret L. Gardel. Self-organizing motors divide active liquid droplets. *Proceedings of the National Academy of Sciences*, 116(23):11125–11130, 2019.
- [6] Philip W Anderson. More is different. *Science*, 177(4047):393–396, 1972.
- [7] Helmut Föll. Iron, steel and swords. URL: <https://www.tf.uni-kiel.de/matwiss/amat/iss/>. Accessed: 2019-07-01.
- [8] Masaru Kuno. Introductory nanoscience: Physical and chemical concepts. *MRS Bulletin*, 37(2):169–170, 2012.
- [9] Richard P. Feynman. There’s plenty of room at the bottom, 1959. URL: <https://web.archive.org/web/20071012033834/http://www.its.caltech.edu/~feynman/plenty.html>. Accessed: 2019-07-23.
- [10] P. G. de Gennes. Soft matter. *Rev. Mod. Phys.*, 64:645–648, Jul 1992.
- [11] George M Whitesides and Bartosz Grzybowski. Self-assembly at all scales. *Science*, 295(5564):2418–2421, 2002.
- [12] Nikhil R Jana. Shape effect in nanoparticle self-assembly. *Angewandte Chemie International Edition*, 43(12):1536–1540, 2004.
- [13] Yonggang Ke, Luvena L Ong, William M Shih, and Peng Yin. Three-dimensional structures self-assembled from dna bricks. *science*, 338(6111):1177–1183, 2012.
- [14] Stefano Sacanna, David J Pine, and Gi-Ra Yi. Engineering shape: the novel geometries of colloidal self-assembly. *Soft matter*, 9(34):8096–8106, 2013.

- [15] John Toner and Yuhai Tu. Long-range order in a two-dimensional dynamical XY model: How birds fly together. *Phys. Rev. Lett.*, 75:4326–4329, Dec 1995.
- [16] M. C. Marchetti, J. F. Joanny, S. Ramaswamy, T. B. Liverpool, J. Prost, Madan Rao, and R. Aditi Simha. Hydrodynamics of soft active matter. *Rev. Mod. Phys.*, 85:1143–1189, Jul 2013.
- [17] Michael Nguyen and Suriyanarayanan Vaikuntanathan. Design principles for nonequilibrium self-assembly. *Proceedings of the National Academy of Sciences*, 113(50):14231–14236, 2016.
- [18] Glenn H. Fredrickson. Surface ordering phenomena in block copolymer melts. *Macromolecules*, 20:2535–2542, 1987.
- [19] Glenn H. Fredrickson and Kurt Binder. Kinetics of metastable states in block copolymer melts. *The Journal of Chemical Physics*, 91(11):7265–7275, 1989.
- [20] Michael Seul and David Andelman. Domain shapes and patterns: The phenomenology of modulated phases. *Science*, 267(5197):476–483, 1995.
- [21] Matthew A. Gebbie, Markus Valtiner, Xavier Banquy, Eric T. Fox, Wesley A. Henderson, and Jacob N. Israelachvili. Ionic liquids behave as dilute electrolyte solutions. *Proceedings of the National Academy of Sciences*, 110(24):9674–9679, 2013.
- [22] Alexander M. Smith, Alpha A. Lee, and Susan Perkin. The electrostatic screening length in concentrated electrolytes increases with concentration. *The Journal of Physical Chemistry Letters*, 7(12):2157–2163, 2016.
- [23] Prudhvidhar Gaddam and William Ducker. Electrostatic screening length in concentrated salt solutions. *Langmuir*, 35(17):5719–5727, 2019.
- [24] Nicholas B. Ludwig, Kinjal Dasbiswas, Dmitri V. Talapin, and Suriyanarayanan Vaikuntanathan. Describing screening in dense ionic fluids with a charge-frustrated ising model. *The Journal of Chemical Physics*, 149(16):164505, 2018.
- [25] Hao Zhang, Kinjal Dasbiswas, Nicholas B. Ludwig, Gang Han, Byeongdu Lee, Suri Vaikuntanathan, and Dmitri V. Talapin. Stable colloids in molten inorganic salts. *Nature*, 542:328–331, 02 2017.
- [26] Vladislav Kamysbayev, Vishwas Srivastava, Nicholas B. Ludwig, Olaf J. Borkiewicz, Hao Zhang, Jan Ilavsky, Byeongdu Lee, Karena W. Chapman, Suriyanarayanan Vaikuntanathan, and Dmitri V. Talapin. Nanocrystals in molten salts and ionic liquids: Experimental observation of ionic correlations extending beyond the debye length. *ACS Nano*, 13(5):5760–5770, 2019. PMID: 30964280.
- [27] Vishwas Srivastava, Wenyong Liu, Eric M Janke, Vladislav Kamysbayev, Alexander S Filatov, Cheng-Jun Sun, Byeongdu Lee, Tijana Rajh, Richard D Schaller, and Dmitri V

Talapin. Understanding and curing structural defects in colloidal gaas nanocrystals. *Nano letters*, 17(3):2094–2101, 2017.

- [28] Vishwas Srivastava, Vladislav Kamysbayev, Liang Hong, Eleanor Dunietz, Robert F Klie, and Dmitri V Talapin. Colloidal chemistry in molten salts: Synthesis of luminescent $\text{In}_{1-x}\text{Ga}_x\text{P}$ and $\text{In}_{1-x}\text{Ga}_x\text{As}$ quantum dots. *Journal of the American Chemical Society*, 140(38):12144–12151, 2018.
- [29] J. N. Israelachvili. *Intermolecular and Surface Forces*. Academic Press, 2011.
- [30] S Marčelja and N Radić. Repulsion of interfaces due to boundary water. *Chemical Physics Letters*, 42(1):129–130, 1976.
- [31] D.A. McQuarrie. *Statistical Mechanics*. University Science Books, 2000.
- [32] Yan Levin. Electrostatic correlations: from plasma to biology. *Reports on Progress in Physics*, 65(11):1577, 2002.
- [33] Yan Levin. Introduction to statistical mechanics of charged systems. *Brazilian Journal of Physics*, 34:1158 – 1176, 09 2004.
- [34] J. P. Hansen and I. R. McDonald. *Theory of Simple Liquids*. Elsevier, 2013.
- [35] Phil Attard. Asymptotic analysis of primitive model electrolytes and the electrical double layer. *Phys. Rev. E*, 48:3604–3621, Nov 1993.
- [36] Lev Davidovich Landau and Evgenii Mikhailovich Lifshitz. *Statistical Physics Part I*. Pergamon Press, 1980.
- [37] Paul M Chaikin and Tom C Lubensky. *Principles of condensed matter physics*, volume 1. Cambridge university press Cambridge, 2000.
- [38] S. A. Safran. *Statistical Thermodynamics of Surfaces, Interfaces, and Membranes*. Westview Press, 2003.
- [39] Mehran Kardar. *Statistical physics of fields*. Cambridge University Press, 2007.
- [40] S. A. Brazovskii. Phase transition of an isotropic system to a nonuniform state. *Soviet Journal of Experimental and Theoretical Physics*, 41:85, January 1975.
- [41] Glenn H Fredrickson and Eugene Helfand. Fluctuation effects in the theory of microphase separation in block copolymers. *The Journal of chemical physics*, 87(1):697–705, 1987.
- [42] M. Grousson, G. Tarjus, and P. Viot. Phase diagram of an ising model with long-range frustrating interactions: A theoretical analysis. *Phys. Rev. E*, 62:7781–7792, Dec 2000.

- [43] Beate West, Frank LH Brown, and Friederike Schmid. Membrane-protein interactions in a generic coarse-grained model for lipid bilayers. *Biophysical Journal*, 96(1):101–115, 2009.
- [44] Philippe Poulin, Holger Stark, T. C. Lubensky, and D. A. Weitz. Novel colloidal interactions in anisotropic fluids. *Science*, 275(5307):1770–1773, 1997.
- [45] John Gregory. Approximate expression for the interaction of diffuse electrical double layers at constant charge. *Journal of the Chemical Society, Faraday Transactions 2: Molecular and Chemical Physics*, 69:1723–1728, 1973.
- [46] John Gregory. Interaction of unequal double layers at constant charge. *Journal of Colloid and Interface Science*, 51(1):44–51, 1975.
- [47] Matthew A Gebbie, Howard A Dobbs, Markus Valtiner, and Jacob N Israelachvili. Long-range electrostatic screening in ionic liquids. *Proceedings of the National Academy of Sciences*, 112(24):7432–7437, 2015.
- [48] Susan Perkin, Mathieu Salanne, Paul Madden, and Ruth Lynden-Bell. Is a stern and diffuse layer model appropriate to ionic liquids at surfaces? *Proceedings of the National Academy of Sciences*, 110(44):E4121–E4121, 2013.
- [49] Matthew A. Gebbie, Markus Valtiner, Xavier Banquy, Wesley A. Henderson, and Jacob N. Israelachvili. Reply to perkin et al.: Experimental observations demonstrate that ionic liquids form both bound (stern) and diffuse electric double layers. *Proceedings of the National Academy of Sciences*, 110(44):E4122–E4122, 2013.
- [50] Hamed Riazi, Sara Mesgari, Noor A. Ahmed, and Robert A. Taylor. The effect of nanoparticle morphology on the specific heat of nanosalts. *International Journal of Heat and Mass Transfer*, 94:254 – 261, 2016.
- [51] Terrell L. Hill. *Statistical Mechanics: Principles and Selected Applications*. Courier Corporation, 2013.
- [52] Roland Kjellander and D. John Mitchell. Dressedion theory for electrolyte solutions: A debyehckellike reformulation of the exact theory for the primitive model. *The Journal of Chemical Physics*, 101(1):603–626, 1994.
- [53] Jonathan Ennis, Roland Kjellander, and D. John Mitchell. Dressed ion theory for bulk symmetric electrolytes in the restricted primitive model. *The Journal of Chemical Physics*, 102(2):975–991, 1995.
- [54] Roland Kjellander and D. John Mitchell. Dressed ion theory for electric double layer structure and interactions; an exact analysis. *Molecular Physics*, 91(2):173–188, 1997.
- [55] B. P. Lee and M. E. Fisher. Charge oscillations in debye-hckel theory. *EPL (Euro-physics Letters)*, 39(6):611, 1997.

- [56] Derek Frydel. The double-layer structure of overscreened surfaces by smeared-out ions. *The Journal of Chemical Physics*, 145(18):184703, 2016.
- [57] Ram M Adar, Samuel A Safran, Haim Diamant, and David Andelman. Screening length for finite-size ions in concentrated electrolytes. *arXiv preprint arXiv:1812.07217*, 2018.
- [58] John G. Kirkwood. On the theory of strong electrolyte solutions. *The Journal of Chemical Physics*, 2(11):767–781, 1934.
- [59] P. Kebblinski, J. Eggebrecht, D. Wolf, and S. R. Phillpot. Molecular dynamics study of screening in ionic fluids. *The Journal of Chemical Physics*, 113(1):282–291, 2000.
- [60] Jiří Janeček and Roland R. Netz. Effective screening length and quasiuniversality for the restricted primitive model of an electrolyte solution. *The Journal of Chemical Physics*, 130(7):074502, 2009.
- [61] Martin Z. Bazant, Brian D. Storey, and Alexei A. Kornyshev. Double layer in ionic liquids: Overscreening versus crowding. *Phys. Rev. Lett.*, 106:046102, Jan 2011.
- [62] Nir Gavish, Doron Elad, and Arik Yochelis. From solvent-free to dilute electrolytes: Essential components for a continuum theory. *The Journal of Physical Chemistry Letters*, 9(1):36–42, 2018. PMID: 29220577.
- [63] A. Yu. Grosberg, T. T. Nguyen, and B. I. Shklovskii. Colloquium. *Rev. Mod. Phys.*, 74:329–345, Apr 2002.
- [64] David J. Bozym, Betl Uralcan, David T. Limmer, Michael A. Pope, Nicholas J. Szamreta, Pablo G. Debenedetti, and Ilhan A. Aksay. Anomalous capacitance maximum of the glassy carbonionic liquid interface through dilution with organic solvents. *The Journal of Physical Chemistry Letters*, 6(13):2644–2648, 2015.
- [65] David T. Limmer. Interfacial ordering and accompanying divergent capacitance at ionic liquid-metal interfaces. *Phys. Rev. Lett.*, 115:256102, Dec 2015.
- [66] Betul Uralcan, Ilhan A. Aksay, Pablo G. Debenedetti, and David T. Limmer. Concentration fluctuations and capacitive response in dense ionic solutions. *The Journal of Physical Chemistry Letters*, 7(13):2333–2338, 2016.
- [67] W. M. Gelbart, R. F. Bruinsma, P. A. Pincus, and V. A. Parsegian. DNA-inspired electrostatics. *Physics Today*, 53(9):38–44, September 2000.
- [68] Yaohua Li, Martin Girard, Meng Shen, Jaime Andres Millan, and Monica Olvera de la Cruz. Strong attractions and repulsions mediated by monovalent salts. *Proceedings of the National Academy of Sciences*, 114(45):11838–11843, 2017.
- [69] Thomas Welton. Room-temperature ionic liquids. solvents for synthesis and catalysis. *Chemical Reviews*, 99(8):2071–2084, 1999.

- [70] Hamed Riazi, Sara Mesgari, Noor A. Ahmed, and Robert A. Taylor. The effect of nanoparticle morphology on the specific heat of nanosalts. *International Journal of Heat and Mass Transfer*, 94(Supplement C):254 – 261, 2016.
- [71] Konstantinos Gkagkas, Veerapandian Ponnuchamy, Miljan Dai, and Igor Stankovi. Molecular dynamics investigation of a model ionic liquid lubricant for automotive applications. *Tribology International*, 113(Supplement C):83 – 91, 2017. 43rd Leeds - Lyon Symposium on Tribology 2016.
- [72] Dan Ben-Yaakov, David Andelman, Rudi Podgornik, and Daniel Harries. Ion-specific hydration effects: Extending the poisson-boltzmann theory. *Current Opinion in Colloid & Interface Science*, 16(6):542 – 550, 2011.
- [73] P Debye and E Hückel. The theory of electrolytes: I. lowering of freezing point and related phenomena. *Phys. Z*, 24:185–206, 1923.
- [74] Luis M. Varela, Manuel Garcia, and Victor Mosquera. Exact mean-field theory of ionic solutions: non-debye screening. *Physics Reports*, 382(1):1 – 111, 2003.
- [75] David Wu, David Chandler, and Berend Smit. Electrostatic analogy for surfactant assemblies. *The Journal of Physical Chemistry*, 96(10):4077–4083, 1992.
- [76] M. Grousson, G. Tarjus, and P. Viot. Monte carlo study of the three-dimensional coulomb frustrated ising ferromagnet. *Phys. Rev. E*, 64:036109, Aug 2001.
- [77] Frank H. Stillinger Jr. and Ronald Lovett. Ionpair theory of concentrated electrolytes. i. basic concepts. *The Journal of Chemical Physics*, 48(9):3858–3868, 1968.
- [78] Athanassios Z. Panagiotopoulos and Sanat K. Kumar. Large lattice discretization effects on the phase coexistence of ionic fluids. *Phys. Rev. Lett.*, 83:2981–2984, Oct 1999.
- [79] Alexandre Diehl and Athanassios Z. Panagiotopoulos. Phase diagrams in the lattice restricted primitive model: From order-disorder to gas-liquid phase transition. *Phys. Rev. E*, 71:046118, Apr 2005.
- [80] Jos Zwanikken and Ren van Roij. Inflation of the screening length induced by bjerrum pairs. *Journal of Physics: Condensed Matter*, 21(42):424102, 2009.
- [81] Mingnan Ding, Yihao Liang, Bing-Sui Lu, and Xiangjun Xing. Charge renormalization and charge oscillation in asymmetric primitive model of electrolytes. *Journal of Statistical Physics*, 165(5):970–989, Dec 2016.
- [82] R.J.F. Leote de Carvalho and R. Evans. The decay of correlations in ionic fluids. *Molecular Physics*, 83(4):619–654, 1994.
- [83] R. R. Netz and H. Orland. Field theory for charged fluids and colloids. *EPL (Euro-physics Letters)*, 45(6):726, 1999.

- [84] Charles E. Sing, Jos W. Zwanikken, and Monica Olvera de la Cruz. Interfacial behavior in polyelectrolyte blends: Hybrid liquid-state integral equation and self-consistent field theory study. *Phys. Rev. Lett.*, 111:168303, Oct 2013.
- [85] P. P. Ewald. Die berechnung optischer und elektrostatischer gitterpotentiale. *Annalen der Physik*, 369(3):253–287, 1921.
- [86] D. Frenkel and B. Smit. *Understanding Molecular Simulations*. Academic Press, San Diego, 2002.
- [87] Melissa E. O’Neill. Pcg: A family of simple fast space-efficient statistically good algorithms for random number generation. Technical Report HMC-CS-2014-0905, Harvey Mudd College, Claremont, CA, September 2014.
- [88] William Humphrey, Andrew Dalke, and Klaus Schulten. Vmd: Visual molecular dynamics. *Journal of Molecular Graphics*, 14(1):33 – 38, 1996.
- [89] R Pathria and PD Beale. Statistical mechanics 3rd ed., 2011.
- [90] Lars Onsager. Crystal statistics. i. a two-dimensional model with an order-disorder transition. *Physical Review*, 65(3-4):117, 1944.
- [91] AL Talapov and HWJ Blöte. The magnetization of the 3d ising model. *Journal of Physics A: Mathematical and General*, 29(17):5727, 1996.
- [92] Maksym V. Kovalenko, Marcus Scheele, and Dmitri V. Talapin. Colloidal nanocrystals with molecular metal chalcogenide surface ligands. *Science*, 324(5933):1417–1420, 2009.
- [93] Evelyn L. Rosen, Raffaella Buonsanti, Anna Llordes, April M. Sawvel, Delia J. Milliron, and Brett A. Helms. Exceptionally mild reactive stripping of native ligands from nanocrystal surfaces by using meerweins salt. *Angewandte Chemie International Edition*, 51(3):684–689, 2012.
- [94] Zhijun Ning, Xiwen Gong, Riccardo Comin, Grant Walters, Fengjia Fan, Oleksandr Voznyy, Emre Yassitepe, Andrei Buin, Sjoerd Hoogland, and Edward H Sargent. Quantum-dot-in-perovskite solids. *Nature*, 523(7560):324, 2015.
- [95] Michael A Boles, Daishun Ling, Taeghwan Hyeon, and Dmitri V Talapin. The surface science of nanocrystals. *Nature materials*, 15(2):141, 2016.
- [96] Oliver J. Lanning and Paul A. Madden. Screening at a charged surface by a molten salt. *The Journal of Physical Chemistry B*, 108(30):11069–11072, 2004.
- [97] Mirijam Zobel, Reinhard B. Neder, and Simon A. J. Kimber. Universal solvent restructuring induced by colloidal nanoparticles. *Science*, 347(6219):292–294, 2015.

- [98] Markus Mezger, Heiko Schröder, Harald Reichert, Sebastian Schramm, John S. Okasinski, Sebastian Schöder, Veijo Honkimäki, Moshe Deutsch, Benjamin M. Ocko, John Ralston, Michael Rohwerder, Martin Stratmann, and Helmut Dosch. Molecular layering of fluorinated ionic liquids at a charged sapphire (0001) surface. *Science*, 322(5900):424–428, 2008.
- [99] Steven C Erwin, Lijun Zu, Michael I Haftel, Alexander L Efros, Thomas A Kennedy, and David J Norris. Doping semiconductor nanocrystals. *Nature*, 436(7047):91, 2005.
- [100] Hao Zhang, Jaeyoung Jang, Wenyong Liu, and Dmitri V. Talapin. Colloidal nanocrystals with inorganic halide, pseudohalide, and halometallate ligands. *ACS Nano*, 8(7):7359–7369, 2014. PMID: 24988140.
- [101] Jacob Israelachvili and Håkan Wennerström. Role of hydration and water structure in biological and colloidal interactions. *Nature*, 379(6562):219, 1996.
- [102] Emanuel Schneck, Felix Sedlmeier, and Roland R. Netz. Hydration repulsion between biomembranes results from an interplay of dehydration and depolarization. *Proceedings of the National Academy of Sciences*, 109(36):14405–14409, 2012.
- [103] B v Derjaguin and L Landau. Theory of the stability of strongly charged lyophobic sols and of the adhesion of strongly charged particles in solutions of electrolytes. *Progress in Surface Science*, 43(1-4):30–59, 1993.
- [104] Andrea Di Cicco, Mauricio Jose Rosolen, Roberto Marassi, Roberto Tossici, Adriano Filipponi, and Jaroslaw Rybicki. Short-range order in solid and liquid kbr probed by exafs. *Journal of Physics: Condensed Matter*, 8(50):10779, 1996.
- [105] David M Heyes and Julian HR Clarke. Computer simulation of molten-salt interphases. effect of a rigid boundary and an applied electric field. *Journal of the Chemical Society, Faraday Transactions 2: Molecular and Chemical Physics*, 77(7):1089–1100, 1981.
- [106] U Löw, VJ Emery, K Fabricius, and SA Kivelson. Study of an ising model with competing long-and short-range interactions. *Physical Review Letters*, 72(12):1918, 1994.
- [107] Nir Gavish and Arik Yochelis. Theory of phase separation and polarization for pure ionic liquids. *The journal of physical chemistry letters*, 7(7):1121–1126, 2016.
- [108] Yoav Tsori, David Andelman, and Michael Schick. Defects in lamellar diblock copolymers: Chevron- and ω -shaped tilt boundaries. *Physical Review E*, 61(3):2848, 2000.
- [109] Steve Plimpton. Fast parallel algorithms for short-range molecular dynamics. *Journal of computational physics*, 117(1):1–19, 1995.
- [110] Alfonso S Pensado and Agílio AH Pádua. Solvation and stabilization of metallic nanoparticles in ionic liquids. *Angewandte Chemie International Edition*, 50(37):8683–8687, 2011.

- [111] Gareth A Tribello, Massimiliano Bonomi, Davide Branduardi, Carlo Camilloni, and Giovanni Bussi. Plumed 2: New feathers for an old bird. *Computer Physics Communications*, 185(2):604–613, 2014.
- [112] Michael R Shirts and John D Chodera. Statistically optimal analysis of samples from multiple equilibrium states. *The Journal of chemical physics*, 129(12):124105, 2008.
- [113] S Marčelja and N Radić. Repulsion of interfaces due to boundary water. *Chemical Physics Letters*, 42(1):129–130, 1976.
- [114] Andrs Aguado and Paul A. Madden. Molecular dynamics simulations of the liquidvapor interface of a molten salt. iii. size asymmetry effects and binary mixtures. *The Journal of Chemical Physics*, 117(16):7659–7668, 2002.
- [115] Michael Grünwald, Alexey Zayak, Jeffrey B Neaton, Phillip L Geissler, and Eran Rabani. Transferable pair potentials for cds and zns crystals. *The Journal of chemical physics*, 136(23):234111, 2012.
- [116] FG Fumi and MP Tosi. Ionic sizes and born repulsive parameters in the nacl-type alkali halides: the huggins-mayer and pauling forms. *Journal of Physics and Chemistry of Solids*, 25(1):31–43, 1964.
- [117] José N Canongia Lopes, Johnny Deschamps, and Agílio AH Pádua. Modeling ionic liquids using a systematic all-atom force field. *The journal of physical chemistry B*, 108(6):2038–2047, 2004.
- [118] Tae-Gon Kim, Danylo Zhrebetskyy, Yehonadav Bekenstein, Myoung Hwan Oh, Lin-Wang Wang, Eunjoo Jang, and A Paul Alivisatos. Trap passivation in indium-based quantum dots through surface fluorination: mechanism and applications. *ACS nano*, 12(11):11529–11540, 2018.
- [119] Peng Han and Gabriel Bester. Interatomic potentials for the vibrational properties of iii-v semiconductor nanostructures. *Physical Review B*, 83(17):174304, 2011.
- [120] Zongzhi Hu, Jenel Vatamanu, Oleg Borodin, and Dmitry Bedrov. A molecular dynamics simulation study of the electric double layer and capacitance of [bmim][pf 6] and [bmim][bf 4] room temperature ionic liquids near charged surfaces. *Physical Chemistry Chemical Physics*, 15(34):14234–14247, 2013.
- [121] Valentina Migliorati, Alessandra Serva, Giuliana Aquilanti, Sakura Pascarelli, and Paola D’Angelo. Local order and long range correlations in imidazolium halide ionic liquids: a combined molecular dynamics and xas study. *Physical Chemistry Chemical Physics*, 17(25):16443–16453, 2015.
- [122] CJ Pings and J Waser. Analysis of scattering data for mixtures of amorphous solids or liquids. *The Journal of Chemical Physics*, 48(7):3016–3018, 1968.

- [123] Cherry S Santos, Harsha VR Annapureddy, N Sanjeeva Murthy, Hemant K Kashyap, Edward W Castner Jr, and Claudio J Margulis. Temperature-dependent structure of methyltributylammonium bis (trifluoromethylsulfonyl) amide: X ray scattering and simulations. *The Journal of chemical physics*, 134(6):064501, 2011.
- [124] PJ Brown, AG Fox, EN Maslen, MA OKeefe, and BTM Willis. International tables for crystallography, vol. c, 2006.
- [125] David I McCooey. Truncated icosidodecahedron. URL: <http://dmccooey.com/polyhedra/TruncatedIcosidodecahedron.html>. Accessed: 2019-08-01.
- [126] Ivan I. Smalyukh. Liquid crystal colloids. *Annual Review of Condensed Matter Physics*, 9(1):207–226, 2018.
- [127] Thuan Beng Saw, Amin Doostmohammadi, Vincent Nier, Leyla Kocgozlu, Sumesh Thampi, Yusuke Toyama, Philippe Marcq, Chwee Teck Lim, Julia M. Yeomans, and Benoit Ladoux. Topological defects in epithelia govern cell death and extrusion. *Nature*, 544:212, Apr 2017.
- [128] Linda S. Hirst and Guillaume Charras. Liquid crystals in living tissue. *Nature*, 544:164 –, Apr 2017.
- [129] Tim Sanchez, Daniel T. N. Chen, Stephen J. DeCamp, Michael Heymann, and Zvonimir Dogic. Spontaneous motion in hierarchically assembled active matter. *Nature*, 491:431 EP –, Nov 2012.
- [130] Nitin Kumar, Rui Zhang, Juan J. de Pablo, and Margaret L. Gardel. Tunable structure and dynamics of active liquid crystals. *Science Advances*, 4(10), 2018.
- [131] Amin Doostmohammadi, Jordi Ignés-Mullol, Julia M. Yeomans, and Francesc Sagués. Active nematics. *Nature Communications*, 9(1):3246, 2018.
- [132] Kimberly L. Weirich, Shiladitya Banerjee, Kinjal Dasbiswas, Thomas A. Witten, Suriyanarayanan Vaikuntanathan, and Margaret L. Gardel. Liquid behavior of cross-linked actin bundles. *Proceedings of the National Academy of Sciences*, 114(9):2131–2136, 2017.
- [133] Marina Soares e Silva, Martin Depken, Björn Stuhrmann, Marijn Korsten, Fred C. MacKintosh, and Gijsje H. Koenderink. Active multistage coarsening of actin networks driven by myosin motors. *Proceedings of the National Academy of Sciences of the United States of America*, 108(23):9408–9413, Jun 2011.
- [134] Pierre-Gilles De Gennes and Jacques Prost. *The Physics of Liquid Crystals*, volume 83. Oxford University Press, 1995.
- [135] J. G. Gay and B. J. Berne. Modification of the overlap potential to mimic a linear sitesite potential. *The Journal of Chemical Physics*, 74(6):3316–3319, 1981.

- [136] Frdric Mondiot, Xiaoguang Wang, Juan J. de Pablo, and Nicholas L. Abbott. Liquid crystal-based emulsions for synthesis of spherical and non-spherical particles with chemical patches. *Journal of the American Chemical Society*, 135(27):9972–9975, 2013.
- [137] Jonathan K. Whitmer, Xiaoguang Wang, Frederic Mondiot, Daniel S. Miller, Nicholas L. Abbott, and Juan J. de Pablo. Nematic-field-driven positioning of particles in liquid crystal droplets. *Phys. Rev. Lett.*, 111:227801, Nov 2013.
- [138] Xiaoguang Wang, Daniel S. Miller, Juan J. de Pablo, and Nicholas L. Abbott. Reversible switching of liquid crystalline order permits synthesis of homogeneous populations of dipolar patchy microparticles. *Advanced Functional Materials*, 24(39):6219–6226, 2014.
- [139] Mohammad Rahimi, Tyler F. Roberts, Julio C. Armas-Pérez, Xiaoguang Wang, Emre Bukusoglu, Nicholas L. Abbott, and Juan J. de Pablo. Nanoparticle self-assembly at the interface of liquid crystal droplets. *Proceedings of the National Academy of Sciences*, 112(17):5297–5302, 2015.
- [140] Kabir Husain and Madan Rao. Emergent structures in an active polar fluid: Dynamics of shape, scattering, and merger. *Physical review letters*, 118(7):078104, 2017.
- [141] W. Michael Brown, Matt K. Petersen, Steven J. Plimpton, and Gary S. Grest. Liquid crystal nanodroplets in solution. *The Journal of Chemical Physics*, 130(4):044901, 2009.
- [142] E. Martín del Río and E. de Miguel. Computer simulation study of the free surfaces of a liquid crystal model. *Phys. Rev. E*, 55:2916–2924, Mar 1997.
- [143] L. F. Rull, J. M. Romero-Enrique, and A. Fernandez-Nieves. Computer simulations of nematic drops: Coupling between drop shape and nematic order. *The Journal of Chemical Physics*, 137(3):034505, 2012.
- [144] Miha Ravnik and Slobodan umer. Landaude gennes modelling of nematic liquid crystal colloids. *Liquid Crystals*, 36(10-11):1201–1214, 2009.
- [145] Peter Prinsen and Paul van der Schoot. Shape and director-field transformation of tactoids. *Phys. Rev. E*, 68:021701, Aug 2003.
- [146] Hartmut Lwen. A phase-field-crystal model for liquid crystals. *Journal of Physics: Condensed Matter*, 22(36):364105, aug 2010.
- [147] Raphael Wittkowski, Hartmut Löwen, and Helmut R. Brand. Microscopic and macroscopic theories for the dynamics of polar liquid crystals. *Phys. Rev. E*, 84:041708, Oct 2011.
- [148] Graham R. Dennis, Joseph J. Hope, and Mattias T. Johnsson. Xmds2: Fast, scalable simulation of coupled stochastic partial differential equations. *Computer Physics Communications*, 184(1):201 – 208, 2013.

- [149] Rapini, A. and Papoular, M. Distorsion d'une lamelle nématische sous champ magnétique conditions d'ancrage aux parois. *J. Phys. Colloques*, 30(C4):C4–54–C4–56, 1969.
- [150] M. Nobili and G. Durand. Disorientation-induced disordering at a nematic-liquid-crystal-solid interface. *Phys. Rev. A*, 46:R6174–R6177, Nov 1992.
- [151] N M Silvestre, P Patrício, M Tasinkevych, D Andrienko, and M M Telo da Gama. Colloidal discs in nematic liquid crystals. *Journal of Physics: Condensed Matter*, 16(19):S1921–S1930, apr 2004.
- [152] Marco Leoni, Oksana V. Manyuhina, Mark J. Bowick, and M. Cristina Marchetti. Defect driven shapes in nematic droplets: analogies with cell division. *Soft Matter*, 13:1257–1266, 2017.
- [153] JA Moreno-Razo, EJ Sambriski, NL Abbott, JP Hernández-Ortiz, and JJ De Pablo. Liquid-crystal-mediated self-assembly at nanodroplet interfaces. *Nature*, 485(7396):86, 2012.
- [154] Matthew R. Stachowiak, Patrick M. McCall, Todd Thoresen, Hayri E. Balcioglu, Lisa Kasiewicz, Margaret L. Gardel, and Ben O'Shaughnessy. Self-organization of myosin ii in reconstituted actomyosin bundles. *Biophysical Journal*, 103(6):1265 – 1274, 2012.
- [155] Yimin Luo, Daniel A. Beller, Giuseppe Boniello, Francesca Serra, and Kathleen J. Stebe. Tunable colloid trajectories in nematic liquid crystals near wavy walls. *Nature Communications*, 9(1):3841, 2018.
- [156] Iris B. Liu, Nima Sharifi-Mood, and Kathleen J. Stebe. Capillary assembly of colloids: Interactions on planar and curved interfaces. *Annual Review of Condensed Matter Physics*, 9(1):283–305, 2018.
- [157] Anja Humpert, Samuel F. Brown, and Michael P. Allen. Molecular simulations of entangled defect structures around nanoparticles in nematic liquid crystals. *Liquid Crystals*, 45(1):59–69, 2018.
- [158] Yu. Trukhina, S. Jungblut, P. van der Schoot, and T. Schilling. Osmotic compression of droplets of hard rods: A computer simulation study. *The Journal of Chemical Physics*, 130(16):164513, 2009.
- [159] P. V Dolganov, H. T Nguyen, G Joly, V. K Dolganov, and P Cluzeau. Shape of nematic droplets in smectic membranes. *Europhysics Letters (EPL)*, 78(6):66001, may 2007.
- [160] Patrick W. Oakes, Jorge Viamontes, and Jay X. Tang. Growth of tactoidal droplets during the first-order isotropic to nematic phase transition of f-actin. *Phys. Rev. E*, 75:061902, Jun 2007.

- [161] Nicolas Puech, Eric Grelet, Philippe Poulin, Christophe Blanc, and Paul van der Schoot. Nematic droplets in aqueous dispersions of carbon nanotubes. *Phys. Rev. E*, 82:020702, Aug 2010.
- [162] Luana Tortora and Oleg D. Lavrentovich. Chiral symmetry breaking by spatial confinement in tactoidal droplets of lyotropic chromonic liquid crystals. *Proceedings of the National Academy of Sciences*, 2011.
- [163] Peter C. Moshenheim, Joel S. Pendery, Douglas B. Weibel, Saverio E. Spagnolie, and Nicholas L. Abbott. Straining soft colloids in aqueous nematic liquid crystals. *Proceedings of the National Academy of Sciences*, 113(20):5564–5569, 2016.
- [164] Luuk Metselaar, Ivan Dozov, Krassimira Antonova, Emmanuel Belamie, Patrick Davidson, Julia M. Yeomans, and Amin Doostmohammadi. Electric-field-induced shape transition of nematic tactoids. *Phys. Rev. E*, 96:022706, Aug 2017.
- [165] Gustav Nyström and Raffaele Mezzenga. Liquid crystalline filamentous biological colloids: Analogies and differences. *Current Opinion in Colloid & Interface Science*, 38:30 – 44, 2018.
- [166] John Shipley Rowlinson and Benjamin Widom. *Molecular Theory of Capillarity*. Courier Corporation, 2013.
- [167] M. J. P. Nijmeijer, A. F. Bakker, C. Bruin, and J. H. Sikkenk. A molecular dynamics simulation of the lennardjones liquidvapor interface. *The Journal of Chemical Physics*, 89(6):3789–3792, 1988.
- [168] E. Martín del Río and E. de Miguel. Computer simulation study of the free surfaces of a liquid crystal model. *Phys. Rev. E*, 55:2916–2924, Mar 1997.
- [169] Daan Frenkel and Berend Smit. *Understanding Molecular Simulation: From Algorithms to Applications*, volume 1. Elsevier, 2001.
- [170] O. V. Kuksenok, R. W. Ruhwandl, S. V. Shiyanovskii, and E. M. Terentjev. Director structure around a colloid particle suspended in a nematic liquid crystal. *Phys. Rev. E*, 54:5198–5203, Nov 1996.
- [171] T. C. Lubensky, David Pettey, Nathan Currier, and Holger Stark. Topological defects and interactions in nematic emulsions. *Phys. Rev. E*, 57:610–625, Jan 1998.
- [172] James E. Komianos and Garegin A. Papoian. Stochastic ratcheting on a funneled energy landscape is necessary for highly efficient contractility of actomyosin force dipoles. *Phys. Rev. X*, 8:021006, Apr 2018.
- [173] Robert Weinstock. *Calculus of Variations: With Applications to Physics and Engineering*. Courier Corporation, 1974.